RESEARCH IN SEISMOLOGY

Frank Press, et al

Massachusetts Institute of Technology

Prepared for:

Air Force Office of Scientific Research
Advanced Research Projects Agency

15 September 1972

Department of Earth and Planetary Sciences

Massachusetts Institute of Technology

Cambridge, Massachusetts 02139

RESEARCH IN SEISMOLOGY

Annual Report to

Air Force Office of Scientific Research

1 April 1971 - 31 March 1972

ARPA Order No. - 1827-1 / 2134

Program Code No. - 2F10

Name of Contractor - Massachusetts Institute of Technology

Effective Date of Contract - 1 April 1971

Contract Expiration Date - 31 December 1972

Amount of Contract - $347,389.00

Contract No. - F44620-71-C-0049

Principal Investigators - Frank Press, 617/253-3382
M. Nafi Toksöz, 617/253-6382
Keiiti Aki, 617/253-6397
Sean C. Solomon, 617/253-3786

Program Manager - William J. Best, 202/694-5456

Short Title of Work - Research in Seismology

Sponsored by

Advanced Research Projects Agency

ARPA Order No. 1827-1 / 2134

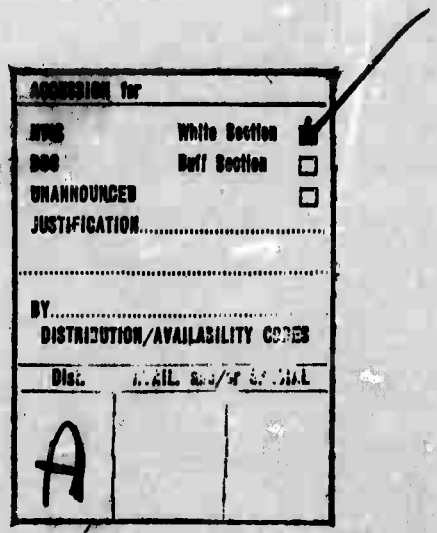

Qualified requestors may obtain additional copies from the Defense Documentation Center. All others should apply to the National Technical Information Service.

Approved for public release, distribution unlimited.

DOCUMENT CONTROL DATA - R & D

(Security classification of title, body of abstract and indexing annotation must be entered when the overall report is classified)

1. ORIGINATING ACTIVITY (Corporate author)
Massachusetts Institute of Technology
Department of Earth & Planetary Sciences
Cambridge, Massachusetts 02139

2a. REPORT SECURITY CLASSIFICATION
UNCLASSIFIED

2b. GROUP

3. REPORT TITLE
RESEARCH IN SEISMOLOGY

4. DESCRIPTIVE NOTES (Type of report and inclusive dates)
Scientific. -------- Interim.

5. AUTHOR(S) (First name, middle initial, last name)
Frank Press Sean C. Solomon
M. Nafi Toksöz
Keiiti Aki

6. REPORT DATE
15 September 1972

7a. TOTAL NO. OF PAGES
~~243~~ 244

7b. NO. OF REFS
214

8a. CONTRACT OR GRANT NO.
F44620-71-C-0049

b. PROJECT NO.
1827-1 / 2134

c. 62701D

d.

9a. ORIGINATOR'S REPORT NUMBER(S)

9b. OTHER REPORT NO(S) (Any other numbers that may be assigned this report)
AFOSR - TR - 73 - 0491

10 DISTRIBUTION STATEMENT
Approved for public release, distribution unlimited.

11. SUPPLEMENTARY NOTES
TECH, OTHER

12. SPONSORING MILITARY ACTIVITY
AFOSR (NPG)
1400 Wilson Blvd.
Arlington, Virginia 22209

13. ABSTRACT

This report gives a summary of the research projects conducted under this contract. These investigations can be grouped into three broad categories: (1) Wave propagation in laterally inhomogeneous media, including studies of body waves, surface waves and free oscillations; (2) Source mechanisms of earthquakes and underground nuclear explosions, including questions of the scaling of earthquake spectra, the tidal triggering of earthquakes, and the release of tectonic strain by explosions; (3) Earth structure, with primary emphasis on developing realistic models for seismic-wave attenuation in the upper mantle and for stress within downgoing slabs of lithosphere. Lists of publications and theses completed during the contract year are also included.

DD FORM 1 NOV 65 1473

14 KEY WORDS	LINK A		LINK B		LINK C	
	ROLE	WT	ROLE	WT	ROLE	WT
Attenuation						
Body waves						
Earth heterogeneities						
Earthquakes						
Earth structure						
Seismic discrimination						
Seismology						
Source mechanism						
Surface waves						
Wave propagation						

Department of Earth and Planetary Sciences

Massachusetts Institute of Technology

Cambridge, Massachusetts 02139

RESEARCH IN SEISMOLOGY

Annual Report to

Air Force Office of Scientific Research

1 April 1971 - 31 March 1972

ARPA Order No. - 1827-1 / 2134

Program Code No. - 2F10

Name of Contractor - Massachusetts Institute of Technology

Effective Date of Contract - 1 April 1971

Contract Expiration Date - 31 December 1972

Amount of Contract - $347,389.00

Contract No. - F44620-71-C-0049

Principal Investigators - Frank Press, 617/253-3382
M. Nafi Toksöz, 617/253-6382
Keiiti Aki, 617/253-6397
Sean C. Solomon, 617/253-3786

Program Manager - William J. Best, 202/694-5456

Short Title of Work - Research in Seismology

Sponsored by

Advanced Research Projects Agency

ARPA Order No. 1827-1 / 2134

ic

TABLE OF CONTENTS

ABSTRACT		i
1.	SUMMARY	1
2.	WAVE PROPAGATION IN LATERALLY HETEROGENEOUS MEDIA	6
3.	SOURCE MECHANISMS OF EARTHQUAKES AND EXPLOSIONS	12
4.	EARTH STRUCTURE	117
5.	LIST OF PUBLICATIONS DURING CONTRACT YEAR	237
6.	LIST OF THESES COMPLETED DURING CONTRACT YEAR	238

1. SUMMARY

In this annual report we summarize briefly the work completed under the contract during the year 1 April 1971 through 31 March 1972. This project, as the title indicates, covers a wide range of topics. A number of specific investigations were undertaken within the broad scope of the problem of discriminating earthquakes from underground nuclear explosions.

The topics studied can be grouped under three general headings:

1. Wave propagation in laterally heterogeneous media,
2. Source mechanisms of earthquakes and explosions,
3. Earth structure.

In the following sections we present abstracts of the published papers falling in each category. Unpublished results are discussed in more detail. Also included are lists of all publications and theses supported under this project during the contract year.

Much has been learned about the interior of the earth by interpreting seismic data in terms of laterally homogeneous earth models. To unravel the fine structure of the crust and upper mantle, and to understand the effects of such fine structure on seismic waves, more realistic, laterally heterogeneous earth models must be studied. Several such investigations are summarized in this report.

In his Ph.D. thesis work, R. Ward developed a theoretical technique to compute the P waveforms from sources located near inhomogeneities. Since many inhomogeneous zones in the earth have characteristic widths similar to the wavelength of long-period body waves, this treatment allows wave amplitudes to be calculated with greater accuracy than does the classical ray-theory approach. Specific problems to which the technique has been applied include the synthesis of P waves from sources near a phase-change boundary in the mantle and near a descending slab of lithosphere as at island arcs.

Also as a Ph.D. thesis, R. Madariaga treated for the first time the theoretical effect of lateral heterogeneities in the earth on free oscillations and long-period surface waves. Using a perturbation theory method, he demonstrated that for realistic earth models with structurally distinct oceanic and continental regions there is significant splitting of earth normal mode spectral peaks for angular order numbers above a critical value, in agreement with observations. Further, standard techniques for "regionalizing" the earth from the dispersion of long-period surface waves were brought into question.

Several approaches to the questions of the forces triggering earthquakes and the physics of the earthquake source are currently being followed. Recent data has required some revision of Aki's scaling law of far-field seismic spectra.

The law is still valid for large magnitudes ($M_s > 6$) and periods ($T > 10$), but one must conclude that large earthquakes and small ones are fundamentally dissimilar. At least two simple modifications of the scaling law can explain the data.

An alternative view of the earthquake source is that of Ida, who models a fault as a rupturing crack. Crack theory may be used to obtain improved relationships for rupture velocity and the stress field near the crack for later comparison of calculations with near-field seismic data.

The question of whether tides play an important role in triggering earthquakes was reexamined by Shlien. An extensive comparison of earthquake occurrences with tidal stresses was conducted, but no significant correlation could be established.

For many underground nuclear explosions, the surface waves indicate a substantial double couple component at the source, most likely due to release of tectonic strain in the rock surrounding the explosion. Toksöz and Kehrer have demonstrated that such strain release depends on the rock type and pre-stress. Tectonic strain energy released as surface waves can occasionally exceed the surface wave energy from the explosion alone. For such explosions, however, the $M_S - m_b$ discriminant is still effective.

Many aspects of earth structure need better definition

if the effects of propagation path and source-region peculiarities are to be successfully removed from seismic signals. Two of these aspects have to date received insufficient attention: seismic-wave attenuation and ambient stress. The former quantity is important because of its effect on the absolute amplitude and spectral shape of seismic waves, the latter because of its relation to natural seismicity and earthquake source parameters.

A detailed investigation by Solomon of seismic attenuation, or Q, beneath North America has demonstrated that Q is frequency dependent, in agreement with predictions of attenuation in a partially melted upper mantle. Together with the known dependence of Q on depth and its variation laterally, this fact complicates the correction of seismic wave spectra for attenuation and thus many discrimination criteria as well. In particular, the $M_S - m_b$ discriminant, the estimation of source depth from surface wave spectra, and the determination of long-period surface wave magnitude and other source parameters can be hampered by imprecise or incorrect knowledge of Q.

As a step toward linking dynamical models of the earth's crust and mantle with global patterns of earthquake occurrence and source mechanisms, Smith and Toksöz have calculated the stress fields within geophysically reasonable models of descending lithosphere slabs. It is within and

adjacent to these slabs that a majority of the world's earthquake occur. The models of stress patterns, including the effects of temperature and phase changes, are in good agreement with the stress distributions inferred from the focal mechanisms of deep earthquakes.

2. WAVE PROPAGATION IN LATERALLY HETEROGENEOUS MEDIA

2.1 Synthesis of Teleseismic P-Waves from Sources Near Transition Zones by Ronald W. Ward (Abstract)

We have developed a useful method to compute both short-period and long-period theoretical seismograms from a P-wave source in or near an inhomogeneous transition zone. The method is applicable to the cases in which the characteristic dimension of the transition zone is comparable to the wavelength and the source is located near (within a few wavelengths) or in the transition zone. Recent evidence indicates that such transition zones may exist in the upper mantle. The transition zone distorts the wave form, gives rise to focusing and complex interference with reflected waves, and also forms frequency dependent shadow zones. The method can take a fuller account of these effects than ray-theoretical methods do, in order that the nature of these transition zones may be determined more precisely.

In our method we avoid the complexity of scattering in the nearfield of a point source by considering the reciprocal problem, which is simply related to the forward problem. We solve the reciprocal problem by using a plane wave approximation in the far field. An exact wave-solution for plane waves incident on a one-dimensional acoustic or elastic linear transition layer is used. An algorithm is developed to evaluate the wave-solutions for a general class of linear

transition zones. The frequency domain far field response to a source near a transition zone is synthesized to obtain theoretical seismograms for comparison with observations.

We apply this method to the problem of the 20° discontinuity, by synthesizing short-period and long-period seismograms for several models of the transition zone. We find that the total velocity increase across the transition zone may be accurately determined from several independent observable features of the seismograms. Even if the focal depth is not accurately known, one can determine the thickness of the transition zone from the reflections, provided there is a low noise (including corrupting arrivals) level (S/N 40 db). If the total velocity increase and the focal depth are precisely known, one can infer the velocity gradient in the transition zone from the observations of a source within the transition zone.

We use our method to treat a simplified model of the sinking lithospheric slab with a 10% maximum velocity contrast. For this model, we find that the ray-theoretical solution predicts the amplitude of the short-period seismogram quite well. The amplitude of the long-period seismogram, however, does not follow the ray-theoretical prediction well. For example, the amplitude in the ray-theoretical shadow zone may be typically 50% of the direct P-wave amplitude. The lithospheric slab broadens the waveform of the long-period

P-wave in certain radiation azimuths. Source mechanism investigators working in the time domain attribute the cause of similar broadening of the waveform to the finiteness of the earthquake source. We show that for sources occurring in and near the lithospheric slab the broadening of the waveform by the slab must be taken into account in source dynamic studies.

We find that the major cause of the difference in the observed radiation pattern between Longshot and Milrow is more likely due to source effects than due to the effect of a nearby lithospheric slab on the different dominant frequencies. For example, the cause of this amplitude difference may be due to greater strain energy release for Milrow than Longshot, introducing a double couple component into the radiation pattern.

2.2 Free Oscillations of the Laterally Heterogeneous Earth by Raul I. Madariaga (Abstract)

The splitting of the eigenfrequencies of the earth due to lateral heterogeneities was studied by the use of classical theory of perturbations of the degenerate eigenfrequencies of the spherically symmetric average earth. The eigenfunctions ${}_n\vec{U}_\ell^m(\vec{r})$ associated with a degenerate frequency lead assymptotically (for large ℓ) to surface waves propagating along great circle paths determined by ℓ and m. The lateral heterogeneities couple these eigenfunctions and

produce a complicated interference pattern on the surface of the earth. The perturbation expansion leads, to first order, to a matrix eigenvalue problem for a Hermitian matrix which selects the constructive interference patterns. The elements of the matrix express the coupling between different eigenvectors of the degenerate problem.

We expand the lateral heterogeneities in a series of spherical harmonics ($\delta\rho_s^t(r)y_s^t(\theta,\psi)$, $\delta\mu_s^t(r)y_s^t(\theta,\psi)$, $\delta\lambda_s^t(r)y_s^t(\theta,\psi)$). Every term in this expansion couples the eigenfunctions selectively. These selection rules can all be deduced from a simple vector diagram. If there is no strong coupling with overtones or spheroidal - toroidal coupling, the odd terms in the spherical harmonics expansion of the heterogeneities do not affect the eigenfrequencies. For instance, there would be no splitting if the earth had a continental hemisphere and an oceanic hemisphere. Also, terms such that $s > 2\ell$ do not affect the eigenfrequencies of modes of order ℓ.

Observations indicate that splitting due to lateral heterogeneity is significant for angular orders $\ell > 20$ or $T < 350$ sec and is of the order of 1.% - 1.5% for toroidal oscillations at $\ell = 40$ and about 1% for spheroidals. Numerical computations for proposed models of continental and oceanic structures show that the splitting predicted theoretically is of the order of the observed. A model in which lateral heterogeneity

is caused solely by anomalous structure of the tectonically active regions was also studied. Computations based on realistic structures beneath these regions show that the effect is too small to account for the observed amount of splitting.

The great circle ray theory commonly used to study the dispersion of long period surface waves is shown to be valid only if the heterogeneities can be expanded with spherical harmonics of very low s($s << \ell$). This puts a severe constraint on the applicability of this theory, in particular it cannot be applied on tectonic regions. Scattering and interference of surface waves in the laterally heterogeneous earth produce time varying amplitude and phase, which cannot be interpreted as due to the effect of local structure along the wave path.

2.3 Spectral Splitting of Toroidal-Free Oscillations Due to Lateral Heterogeneity of the Earth's Structure by Raul Madariaga and Keiiti Aki (Abstract)

Contradicting results have been obtained by H. Kanamori (1970) and A.M. Dziewonski (1970) on the 'pure-path' dispersions of mantle Rayleigh waves. This discrepancy may be due to the inadequacy of their methods of ray-theory interpretation, in that the total phase delay is assumed to be the algebraic sum of delays over the lengths of pure paths measured along the great-circle path. In order to take into

account the effect of interference by the waves propagating in other directions, we apply a perturbation method to several laterally heterogeneous earth models and calculate the splitting of eigenfrequency of toroidal oscillations. For the order number $\ell = 40$, observation shows the variation of the spectral peak to be as much as 1.7% of the degenerate frequency. The continent-ocean heterogeneity with 8099 or 5.08M as the oceanic model and CANSD as the continent model produces the multiplet width of about 1%. The continent-ocean heterogeneity with O1 and S1 as the constituent models gives less than 0.4% multiplet width. The tectonic heterogeneity, in which the tectonically active region is assumed to be different from the rest of the world, also produced too small a multiplet width for any choice of models of these regions. The ray-theory method of interpreting the great-circle phase velocities has been examined by the criterion obtained by R. Madariaga (1972). With the modes having order numbers $\ell < 40$, the ray theory is not applicable to any of the laterally heterogeneous earth models discussed here.

3. SOURCE MECHANISMS OF EARTHQUAKES AND EXPLOSIONS

3.1 Earthquake Mechanism by Keiiti Aki (Abstract)

Important progress has been made in the study of the earthquake mechanism during the Upper Mantle Project, through the establishment of an appropriate mathematical framework which relates the observed seismogram with the slip motion across a fault plane. Since an arbitrary fault slip is described by a function of time and two space coordinates, a complete inversion of the observed seismogram is practically impossible. The only practical inversion method is to describe the kinematics of rupture growth along a fault plane using a small number of source parameters, and then to determine those parameters from the seismograms. A number of kinematic models have been proposed to cover a class of earthquakes. Preliminary attempts have also been made to find dynamic models by solving the problem of spontaneous rupture propagation for given initial conditions.

There are a few source parameters, which represent some averaged quantities over the source time and source space and are therefore independent of the details of rupture kinematics. They are: (1) the seismic moment, which is proportional to the total displacement averaged over the fault surface; and (2) the apparent stress, which is proportional to the ratio of total seismic energy to seismic moment. In addition to these, the average stress drop can be approximately

calculated from the seismic moment and the fault area, without detailed knowledge of the kinematics. The accuracies of determining these average quantities are discussed for the Parkfield, California earthquake of 1966, one of the best studied earthquakes during the U.M.P. period. Recent results from several well-studied earthquakes are then summarized as: (1) the relation between magnitude and seismic moment; and (2) the relation between stress-drop and magnitude. It was found that the stress drop in shallow earthquakes is 10-100 bar, apparently independent of magnitude for $M > 6$. Finally, recent evidences for the fault origin of deep-focus earthquakes are presented.

3.2 Recent Results on the Mechanism of Earthquakes with Implications on the Prediction and Control Program

by Keiiti Aki (Abstract)

The current earthquake prediction and control research programs are based on the working hypothesis that an earthquake is a release of tectonic strain energy stored up in a volume of the earth's crust. Accumulating seismological evidence indicates that this energy release is done by a propagating rupture which creates a shear dislocation over a finite fault plane.

The velocity of the rupture propagation is the single, most important factor in the dynamics of energy release in this process. If the velocity is very slow and the dislocation takes place quasi-statically, all the strain energy will be

spent against friction on the fault and there will be no seismic energy radiation and no earthquake hazard.

If the velocity of rupture propagation is infinite and the stress release takes place instantaneously over the entire fault plane, then the particle velocity on the fault is simply the stress divided by the impedance, that is, the product of density and shear velocity. As discussed by Brune, the particle velocity of about 1 meter/sec is predicted for the stress release of about 100 bars.

For a finite rupture velocity, however, the impedance depends on rupture velocity. For example, for longitudinal-shear cracks, the impedance becomes zero when the rupture propagates with the shear velocity. In this case, the particle motion becomes infinite when there is a finite stress release along the fault. For a given tectonic stress, therefore, one should expect seismic motion with an amplitude from zero to infinity critically dependent on the rupture velocity. If we find the way to control the rupture velocity, we can control an earthquake.

Early seismological determination of rupture velocities indicated the velocity at 3 to 4 km/sec, a little below the medium shear velocity. Later studies extended the range from about 1.5 to about 4.5 km/sec.

We have not yet established any systematic dependence of rupture velocity on the earthquake parameters such as

focal depth, fault-plane geometry, and other tectonic features of an epicenter. For example, a typical strike-slip earthquake on the San Andreas fault and a deep South American earthquake share the same rupture velocity of 2.2 km/sec. There are some indications that the rupture propagation is faster for large earthquakes than for small ones, but we do not have enough data to draw definite conclusions.

3.3 Cohesive Force across the Tip of a Longitudinal-Shear Crack and Griffith's Specific Surface Energy by Yoshiaki Ida (Abstract)

The cohesive force across the fault plane is considered in order to understand the physical mechanism of rupture at the tip of a longitudinal-shear crack. The elastic field around the tip of a crack and the condition of rupture growth are systematically derived from the assumption that the cohesive force is given as a function of the displacement discontinuity. This assumption is more physically meaningful than those originally used by G.I. Barenblatt in 1959 and 1962. The stress field around the tip is calculated for several models of cohesive force, and is shown to be nonsingular even at the tip. The condition of rupture growth that is used to determine the rupture velocity turns out to be equivalent to the Griffith criterion and the relation employed by B.V. Kostrov in 1966, but the specific surface energy is defined more clearly in this paper.

3.4 Earthquake-Tide Correlation by Seymour Shlien (Abstract)

The detection of moonquakes that occur when the moon is at perigee has prompted a search for tidal effects on earthquake occurrences. An attempt was made to correlate earthquakes listed in the CGS-NOAA epicenter determinations with the tidal phase of semidiurnal tides. This study was confined to several seismic regions representative of tectonic and non-tectonic regions. An extended form of Schuster's test was used to decide whether significant correlations existed. Though some tidal influences could be accepted at a 5% significance level, the effect was not consistent or stable with time. Earthquakes, if they are affected by tides, show a slight tendency to occur at times when the tidal stress is changing most rapidly. Insufficient data was available to compare tectonic to non-tectonic areas.

An analysis of the Japanese aftershock sequence which began 11 August 1969 was found to have no significant tidal correlation.

3.5 Scaling Law of Earthquake Source Time-Function by Keiiti Aki

Summary

Further evidences support the scaling law of far-field seismic spectrum based upon the ω-square model (Aki, 1967) for earthquakes with $M_s > 6$ and for periods $T > 10$ seconds. Recent observations, however, unequivocally require the modification of the above law for periods $T < 10$ seconds. Unfortunately, the presently available data are not sufficient for a unique revision of the scaling law. We propose two alternatives and discuss their implications and consequences. In either case, we have to conclude that a large earthquake and a small one are substantially different. One interesting feature of the ω-square model appears to be unaffected by the required revision; that is, the spectral density of the dislocation time-function for periods $T < 5$ seconds takes the same absolute value, independent of magnitude, for earthquakes greater than $M_s = 6.5$. This result has important consequences in earthquake engineering because the seismic motion in the vicinity of an earthquake fault will scale as the dislocation function.

1. INTRODUCTION

As a first step to relate the seismic spectrum with earthquake magnitude, a model of earthquake ensemble was proposed by Aki (1967) on the basis of a dislocation theory of earthquake faulting. In this model, the source factor of far-field spectrum diminishes inversely proportional to the square of frequency ω beyond a corner frequency. For this frequency dependence, it was called the "ω-square model." Below the corner frequency, the spectrum is flat with the height proportional to the seismic moment (Aki 1966). A family of such spectral curves was constructed on the assumption that large and small earthquakes are similar phenomena in a medium with given elastic constants and density. The assumption implies the same geometry, a constant stress-drop, constant rupture velocity and slip velocity, independent of magnitude, and it follows that the corner frequency is inversely proportional to the fault length, and the seismic moment to the cube of fault length. Thus, the corner frequency lies on a straight line with slope 3 in Fig. 1 which shows the logarithm of spectrum against the logarithm of period. The spacings between the curves are made equal at the period of 20 seconds to be compatible with the definition of M_s by Gutenberg and

Richter. The scaling law shown in Fig. 1 explained very well Berckhemer's (1962) observations on spectral ratios, Gutenberg-Richter's (1956) M_S-M_b relation for $M_S > 6$, and Tocher's (1960) data on the earthquake fault length and magnitude.

The assumption of similarity comes from the idea advocated by Tsuboi (1940, 1956, 1958, 1965) who held the view that the strain energy density prior to the earthquake occurrence is the property of rock material independent of earthquake magnitude, and that the energy of an earthquake is determined by the volume within which it has been stored. This idea radically contradicts the assumption underlying Benioff's (1951) strain release curve, which was calculated as the square root of energy release implying a constant earthquake volume independent of magnitude. The latter view may be natural to the California seismologists, becuase the majority of California earthquakes, large or small, appear to be associated with the same fault plane; the San Andreas. It was, however, unacceptable to the Japanese seismologists who were familiar with the distinct difference in spectral structure between large and small, especially microearthquakes (Asada 1957). The controversy appeared to have been settled when Båth and Duda (1964) summarized observational data in favor of Tsuboi's idea and proposed an improvement of Benioff's method for

calculating the strain release curve. Thus, the assumption of similarity was the most reasonable one at the time when the ω-square model was proposed.

Since then, a large amount of observational data have become available for more critical testing of the proposed model. In general, the new evidences support the ω-square model for earthquakes larger than $M_S = 6$, and for periods longer than 10 seconds. For smaller earthquakes or for shorter periods, new evidences require revision of the ω-square model. The purpose of the present paper is to propose such a revision, and to discuss its implications and consequences. Since, unfortunately, the presently available data are not sufficient for a unique revision, discussion will be made for two alternative revision.

An interesting feature of the ω-square model is that the spectral density of dislocation time-function for periods shorter than 5 seconds is identical, in the absolute scale, for all the earthquakes greater than $M_S = 6.5$. This feature of the ω-square model, which is particularly important for earthquake engineering, is unaffected by the revision required in the present paper.

2. COMPARISON WITH OBSERVATIONS

The validity of the scaling law shown in Fig. 1 can be tested against various kinds of observations. In general, the right-half ($T > 10$ sec) of Fig. 1 shows excellent agreements with the observed data, but the left-half ($T < 10$ sec) does not. Let us start with observations at the infinite period, that is, static fault parameters.

(1) Fault length. Fig. 2 shows the data on magnitude and fault length reproduced from Chinnery (1969). In view of the difficulties in extracting reliable observations of fault parameters from field data the observed points in Fig. 2 were thoughtfully limited to those of near-vertical faults on which the movement was predominantly strike-slip. The surface wave magnitude M_S is used for events with magnitude over 6, and local Richter magnitude M_L for events less than 6. The empirical formulas by Iida (1959, 1965) and Tocher (1958) show a good fit to the data for large earthquakes. Otsuka's (1965) formula is proposed to take into account the hidden part of a fault unnoticed by field observation. Both Otsuka's and Press' (1967) formula predicts much steeper slope than observed for $M > 7$. This discrepancy was attributed to the non-similar fault shape between large and small earthquakes

due to the effect of crustal structure.

The ω-square model, on the other hand, gives exactly the same slopes as those of the Iida and Tocher formulas, and explains the observed slope for large events excellently without invoking the non-similarity. The bending of the curve at about $M = 7$ is due to the inefficiency of M_s as a measure of the size of large earthquakes.

The curve for the ω-square model in Fig. 2 was drawn, first, by finding the relation between M_s and the corner period from Fig. 1, and then multiplying the corner period by a constant to obtain the fault length. Under the assumption of similarity, the corner period and fault length should be proportional to each other. The proportionality constant giving the best fit to observation is 0.65 km/sec (see Fig. 11 of Aki 1967). It is interesting to compare this value with the theoretical coefficient used by Brune (1970, 1971), in which the radius r of earthquake source is related to the corner frequency f_o of shear wave spectra by $r = \frac{2.34\beta}{2\pi f_o}$, where β is the shear velocity. If we take $2r$ as the fault length, the coefficient is 2.6 km/sec for $\beta = 3.5$ km/sec. This is about 4 times larger than the value obtained from the observational data for large earthquakes. It appears that Brune's theory does not apply to large earthquakes. The discrepancy may be attributed to his assumption of infinite

rupture velocity, which is not realistic for a spontaneous rupture (Ida & Aki 1972).

Within the scheme of Aki's (1967) statistical fault model, the corner period T is related to the mean free path k_L^{-1} of fault propagation by the relation

$$k_L^{-1} = \frac{v}{2\pi} T$$

where v is the velocity of rupture propagation. For $v = 3$ km, we find that the mean free path is proportional to the corner period with coefficient about 0.5, which is close to the observed coefficient 0.65 for the fault length. For large earthquakes and for long periods, therefore, the rupture propagation appears to be smooth and encounters no obstacle during the growth to its final length.

The curve based on the ω-square model does not explain the data for small earthquakes shown in Fig. 2, which includes the Imperial earthquake of March 4, 1966 described by Brune and Allen (1967) who demonstrated beyond doubt that an earthquake with magnitude 3.6 could have a 10 km fault length. However, some of the data are questionable. For example, one after-shock ($M = 4.9$) of the Parkfield earthquake of 1966 was given a fault length of 33 km from creep observations (Wyss & Brune 1968). The wide-band spectra of Love waves (Filson & McEvilly

1967) from this earthquake, however, did not show the evidence for such a long fault. Since the field measurement of fault length becomes increasingly difficult with decreasing magnitude, we must resort to indirect methods. For example, Lieberman and Pomeroy(1970) used the data on an aftershock area in a general support of the Wyss-Brune curve of Fig. 2. However, an accurate determination of aftershock area for a small main-shock is a difficult problem and also the aftershock area may give an overestimate of the main-shock fault area (Aki 1968).

(2) Stress drop. Further evidences from field data support the validity of the ω-square model for large earthquakes. Fig. 3 shows the relation between M_s and log LD^2 reproduced from King and Knopoff (1968), where L is the fault length and D is the fault offset. King and Knopoff found that the slope of best-fitting lines is significantly different from the slope of any published magnitude-seismic energy relations. From this result, assuming a dislocation model with a constant efficiency independent of magnitude, they concluded low fractional stress-drop for small earthquakes. Their conclusion has been extended to small earthquakes by Wyss (1970), and was considered as an evidence against the similarity assumption (constant stress-drop) underlying the ω-square model.

The parameter LD^2 is proportional to L^3, and therefore to the seismic moment in the ω-square model. One can draw a theoretical relation between M_s and LD^2 by finding the seismic moment for a given M_s in Fig. 1 and multiplying a constant. For a rectangular fault with width W, this constant is equal to $\frac{D}{\mu W}$, which is a measure of strain-release or stress drop. The constant was chosen as 3×10^{-17} $dyne^{-1}$ cm^2 in Fig. 3. Assuming that $\mu = 3 \times 10^{11}$ dyne cm^{-2} in the earth's crust, we find that $\frac{D}{W} = 10^{-5}$ and $\mu\frac{D}{W} = 30$ bars. This value is a reasonable rough estimate of stress drop in large shallow earthquakes (Chinnery 1964; Brune & Allen 1967). A recent summary of earthquake mechanism studies by Aki (1972) demonstrates that the stress drop in shallow earthquakes with $M > 6$ is 10 to 100 bars independent of magnitude. Here, again, we see that the ω-square model can explain observed field data without invoking non-similarity.

(3) Seismic moment. Fig. 4 is reproduced from Aki (1972), who summarized the data on M_s and seismic moment obtained from long-period surface waves and free oscillations. Body wave results were not included because of the controversial window effect discussed by Linde & Sacks (1971), who concluded that theories which predict constant displacement spectrum for body waves at long periods (the ω-square model

is one of them) must be in error. Their results are in favor of the Archambeau (1968) theory which predicts a sharp drop of spectrum toward zero frequency. We disagree with their conclusion because the surface wave and free oscillation spectra which do not suffer from the window effect invariably show consistency with the assumption of step function dislocation at the low-frequency end of observable spectrum. The best example is the free oscillation amplitude excited by the Kurile earthquake of October 13, 1963 (M = 8 1/4). Abe (1970) demonstrated that the assumption of step function was valid for the order numbers 10 to 30 for both spheroidal and torsional oscillations. Other convincing cases may be found in Ben-Menahem and Toksöz (1963), Aki (1966), Kanamori (1970a,b), Tsai and Aki (1969, 1970a,b, 1971).

The smooth curve designated as "ω^2-model" in Fig. 4 was drawn by plotting the height of the flat portion of spectrum for a given M_S shown in Fig. 1. The absolute value was fixed in such a way that the curve passes through the observed point for the Niigata earthquake, for which the first accurate determination of seismic moment was made by Aki (1967).

The dashed lines in Fig. 4 represent the calibration curve used by Brune (1968) and Davies and Brune (1971) to find the rate of slip along major fault zones of the earth from the earthquake magnitude data. The curve was developed through a

series of papers by Brune and his colleagues (Brune & King 1967; Brune & Engen 1969; Wyss & Brune 1968), and consisting of the following line segments:

(A) $\log M_o = M_s + 19.9$ for $M_s > 7.5$ and strike slip. (0.3 is added for dip slip)

(B) $\log M_o = M_s + 19.2$ for $7 > M_s > 6$

(C) $\log M_o = 1.4M_L + 17.0$ for $6 > M_L > 3$

The segments (A) and (B) were originally proposed by Brune and King as a relation between M_s and the Rayleigh wave amplitude at about 100 second periods. They assumed ω^{-1} dependence instead of ω^{-2}, and using Tocher and Iida's data on fault length, assumed that the corner period is longer than 100 seconds for $M_s > 7.5$, and is shorter than 20 seconds for $M_s < 7$. Thus, the constants in (A) and (B) differ by the logarithm of the ratio of two periods, as can be figured out from a schematic illustration of scaling law for the "ω-model" shown in Fig. 5. It is obvious from Fig. 5 that the coefficient in the moment-magnitude relation for $M > 7$ should be 1.5 and cannot be unity as given in (A). In order to be consistent with the model described by Brune and King (1967), we must replace the formula (A) by the following:

(A') $\log M_o = 1.5\, M_s + 16.0$, for $M > 7$

This will connect to the line (B) properly as expected for the ω-model sketched in Fig. 5.

Since the formula (C) was obtained empirically as the relation for local magnitude M_L, it is not applicable to the data shown in Fig. 4. The formula (B) should apply to all M_s less than 6 as can be seen from Fig. 5. If we compare the data in Fig. 4 with the formulas (A') and (B) shown by chained lines, we find a systematic discrepancy; all the data for $M_s < 6.5$ fall below the line (B), and all the data for $M_s > 7.5$ lie above the line (A'), except for the Sanriku earthquake, which is an unusual "lithospheric normal faulting" according to Kanamori (1971). On the other hand, the ω^2-model explains the observation except for the Sanriku earthquake without significant systematic error.

It is true, however, that Brune-King's ω-model explains the mantle wave data of Brune and King (1967) and Brune and Engen (1969) somewhat better than the ω-square model. Most of their data on large earthquakes are, however, from old instruments, and Brune and Engen express some concern about uncertain instrument calibration. Furthermore, the correction for attenuation and geometrical spreading may be biased because most of the data for small earthquakes are from the Pasadena

station and larger ones are from other stations. Such problems may be avoided by the use of spectral ratio between earthquakes with different size but with common path and recording station.

(4) Spectral ratio. The observed seismic spectrum is a function of source, path and receiver. The simplest way of isolating the source spectrum is to compare seismograms obtained by the same seismograph at the same station from two earthquakes of the same epicenter but of different size. Berckhemer (1962) was able to collect 6 such earthquake pairs from the Stuttgart records for the period 1931 to 1951. Their magnitudes range from 4.5 to 8.0, and the epicentral distances 400 to 9000 km. The separation between epicenters of each pair was less than 1°. Their locations are shown in a world map in Fig. 6. The ω-square model explains very well the observed spectral ratio for all the pairs, except the one in the Alps for which the comparison was fair (Aki 1967). A good agreement was obtained also for two aftershocks of the Kern County, California earthquake of 1952.

A similar collection of spectra for earthquake pairs has been made recently by Tsujiura (1972), using his multichannel band-pass seismographs (Tsujiura 1966, 1967, 1969). The location of earthquake pairs is shown in Fig. 6. The

ω-square model explained the spectral ratio for the pairs in China (M7.5/M6.1) and Halmahera (M7.2/M6.3) excellently. However, a striking discrepancy was found for two pairs of earthquakes in the Aleutians (M7.1/M6.3, M7.0/M5.7). Judging from their epicenters, they all belong to the underthrusting rather than the extensional group (Stauder 1968). Tsujiura's observation indisputably shows that the M7 and M6 Aleutian earthquake share nearly identical spectral shape in the period range 10 to 100 seconds. This result definitely contradicts the prediction of the ω-square model, because, as shown in Fig. 1, the corner period is about 10 seconds for M=6, and about 40 seconds for M=7.

So far, the failure of the ω-square model in explaining the scale effect on seismic spectrum may be considered as an exception. Such exceptional cases are the seismic moment of the Sanriku earthquake and the spectral ratios of the two earthquake pairs in the Aleutians. So far, we have considered the period range longer than 10 seconds. Once we enter the period range shorter than 10 seconds, however, the failure of the ω-square model becomes a rule rather than an exception.

(5) $M_s - M_b$ relation. Gutenberg and Richter (1956) discovered a discrepancy between the magnitude scale based upon short-period body waves (M_b) and that based upon long-period surface waves (M_s).

This discrepancy was attributed to the scale effect by Aki (1967), and it was shown that the ω-square model explains the M_s - M_b relation observed by them.

Recently, the M_s - M_b relation attracted the attention of several seismologists because of its power as a discriminant between earthquakes and underground explosions (Lieberman et al. 1966; Lieberman & Pomeroy 1967, 1969; Capon et al. 1967; Basham 1969; Molnar et al. 1969; Evernden et al. 1971; Lieberman & Basham 1971).

Fig. 7 summarizes the range of observed data on M_s versus M_b for various regions. The curve designated as "ω-square model" is drawn assuming that M_s is proportional to the spectral density at the period 20 seconds, and M_b is proportional to that at 1 second. The former assumption is valid because of the definition of M_s, and the latter is valid because the repsonse of seismographs used for teleseismic P waves from small events are usually sharply peaked at about 1 second. This assumption was used by Lieberman & Pomeroy (1969) in their discussion of the M_s-M_b relation. Aki (1967) took into account the small effect of signal duration as shown in Fig. 8 for larger events, but such correction may be unnecessary for smaller events, for which the duration is probably determined by the instrument response and path effect. The curve for the ω-square model is further restricted to pass through the point

($M_s = M_b = 6\ 3/4$) according to the original definition by Gutenberg & Richter (1956).

Fig. 7 clearly demonstrates that the observed M_s-M_b relation deviates systematically from the predicted for the ω-square model. The data follows the straight linear extrapolation of the Gutenberg-Richter formula ($M_s = 1.59\ M_b - 3.97$) rather than following the bended curve of the ω^2-model as shown in Fig. 8. It is extremely interesting to note that this departure from the ω-square model makes the discrimination between explosion and earthquake possible for small events. The data for explosions are represented by a line $M_s = M_b - 1.8$, which was established by Thirlaway & Carpenter (1966).

The fact that the M_s-M_b relation for earthquakes does not bend according to the ω-square model but follows the straight line along the extrapolated Gutenberg-Richter formula has an additional support from a work on spectral densities done in the U.S.S.R. Chalturin (1970) made observations at Garm, using a multi-channel band-pass seismograph similar to Tsujiura's (1966, 1967, 1969), and found that the observed relation between the amplitudes at 1 second and 20 seconds follows a straight line with the coeeficient the same as in the Gutenberg-Richter formula, and does not agree with the prediction of the ω-square model. This evidence is particularly strong because no assumptions are made on the relation between magnitudes and spectral densities.

Everrden et al. (1971) emphasize the parallelism of the

M_s versus M_b curves for explosions and earthquakes, and suggest that the $M_s - M_b$ relation for earthquakes with $M_b < 5\ 1/4$ has a slope of approximately 1. Such a suggestion is not inconsistent with the observation, but the data show too much scatter to allow a firm conclusion (see Figs. 7 and 8).

3. REVISED MODELS

Since the ω-square model explains, in general, the observations for the period range longer than 10 seconds, the right half of Fig. 1 should be left unchanged. In order to revise the left half, we shall consider the following two extreme cases. In one revision, we shall keep the ω^{-2}-dependence, but discard the similarity assumption and change the relation between M_s and the corner frequency. This shall be called the revised model A. In the other, we shall give up the ω^{-2}-dependence and adopt the ω^{-1}-dependence in the period range between 10 to .01 seconds. In this case, the relation between M_s and the corner period is unchanged from the ω-square model. We shall refer to this as the revised model B.

(1) Model A

Fig. 9 shows the family of spectral curves for the revised model A, in which the spacing between the curves of Fig. 1 at 1 second was widened to satisfy observed $M_s - M_b$ relation without changing the ω^{-2}-dependence. This resulted in

a shift of corner period to the right for $M_s < 6$. For $M_s < 4\ 1/2$, the corner period stays constant, because we follow the suggestion of Evernden et al. (1971) that the slope of the $M_s - M_b$ relation is unity for $M_b < 5\ 1/4$.

The relation between M_s and the corner frequency is shown in Fig. 10 for various cases. The one corresponding to the suggestion of Evernden et al. indicates the corner period of about 6 seconds for $M_s < 4\ 1/2$. The physical picture behind this is very simple. The fault length, rupture propagation time, and rise time are common to all the earthquakes smaller than $M_s < 4\ 1/2$. The only difference between them is the offset, or strain release or stress drop. This is a revival of Benioff's (1951) idea mentioned in the introduction, and was suggested by Brune & Wyss at the Woods Hole Conference on Seismic Discrimination, July, 1970, sponsored by the Advanced Research Projects Agency. This idea is quite compatible with the concept of "pre-existing fault" which naturally violates the assumption of similarity.

One cannot, however, extend the 6 second corner period to microearthquakes ($M \simeq 0$). The frequency ranges of usual microearthquakes are between 10 to 100 cps [Nevada may be an exceptional area according to Douglas & Ryall (1972), and Takano (personal communication)]. For example, typical records of micrearthquakes may be found in Furuya (1969), and an extensive collection of data in Terashima (1968).

Although M_s cannot be used for microearthquakes, the seismic moment has been estimated for the magnitude zero earthquake by Wyss & Brune (1968), Aki (1969), Takano (1971) and Douglas & Ryall (1972) as $10^{16} \sim 10^{17}$ dyne cm. Therefore, the actual corner period should reach the lower-left corner in Fig. 10. The curve for the ω-square model does, but others have to be sharply bent to reach that corner. Such a sharp bend in the corner period curve produces a strange scaling law of spectrum for $M_s < 3$ as shown in Fig. 9. All the earthquakes with $-1 < M_s < 3$ share the same spectral density for frequencies higher than 20 cps.

Both the bend in the magnitude-corner period relation and the above mentioned peculiar scaling law of microearthquake spectrum are demonstrated in the data reported by Terashima (1968) (see his Figs. 5.5 and 6.5). Unfortunately, the definitions of magnitude and corner period are different between large and small earthquakes, and it is impossible to decide whether the apparent bend in the M_s-corner period curve reported by Terashima is due to the scale effect or some other effects such as a gap in recording instrument response for large and small earthquakes, or different attenuation and wave scattering effects between short and long periods.

It is, nevertheless, intriguing to consider the earthquake of revised model A as consisting of three distinct groups:

one with $M_s > 6$, one with $6 > M_s > 3$, and the other with $M_s < 3$. The largest earthquake group has roughly constant stress drop (10 to 100 bars) independent of earthquake magnitude. The medium-sized group shares pre-existing faults (a few kilometers long), and the smaller shock of this group shows less stress drop. In the smallest group, on the other hand, the stress drop increases with the decreasing magnitude, in agreement with Mogi's (1962) observation on the size effect on fracture strength and with the high stress drop observed in laboratories for small rock samples (the fracture strength is proportional to $L^{-0.1}$ where L is the linear dimension of the sample, according to Mogi). If the earth's crust contains weak zones, faults or cracks of a size predominantly a few kilometers, it is conceivable to have such distinct groups of earthquakes.

(2) Model B

Let us consider the other extreme way of modifying the ω-square model. Keeping the M_s versus corner-frequency curve unchanged, and simply changing the frequency dependence from ω^{-2} to ω^{-1} for periods less than about 5 seconds, we can approximately satisfy the observed $M_s - M_b$ relation. Since the ω^{-1} dependence up to the infinite frequency results in an infinite seismic energy, we assume that the spectral

density drops sharply at about 100 cps. The resultant family of spectral curves is shown in Fig. 11.

This set of curves can explain all the main observations discussed earlier: (1) fault length, (2) stress drop, (3) seismic moment, (4) spectral ratio for T >10 seconds, and (5) $M_s - M_b$ relation. In this modification, we assumed that the suggested bend of M_s versus corner frequency may not be due to the source effect but due to instrumental or propagational path effects. Thus, the M_s - corner frequency relation is the same straight line as in the ω-square model.

One additional support of this model comes from the work of Asada & Takano (1963) and Takano (1970, 1971) on the attenuation measurement using the spectral shape in the period range 0.1 to 1 seconds. They assumed the ω^{-1} dependence at the source and obtained reasonable Q values. They used this shape of source spectrum following Kanai & Yoshizawa's (1958) classic work on the seismic spectrum of nearby earthquakes measured in a deep mine in Japan.

Instead of three groups of earthquakes for revised model A, we find two distinct groups for model B. Earthquakes with $M_s < 6$ are all the same kind; the ω-model of Brune & King (1967) discussed earlier. On the other hand, earthquakes with $M_s > 6$ have peculiar spectral shapes. For example, the spectrum for M8 first decreases as ω^{-2} beyond the corner frequency (about

0.003 cps) but then the decrease slows down to ω^{-1} beyond 0.1 cps.

Within the scheme of a simple dislocation model of an earthquake described by a unidirectional rupture propagation and a step-like offset with a finite rise time (Haskell 1964), the above ω-model implies a very short rise time, outside the range of seismological observation. In view of an incoherent rupture propagation such as described by Haskell (1966) and Aki (1967), the ω-model may correspond to a process in which the fault offset takes place as a succession of irregular rapid motion with a very short time constant. In other words, the fault moves like a car running at a full speed on a very bumpy road. Finally, in the framework of Brune's (1970) model, the ω-model implies very small fractional stress drop, or very large difference between dynamic and static friction. These three interpretations appear to describe the same phenomena: rapid slips and sudden stops.

The peculiar spectral shape for large earthquakes may be explained, if the large one behaves as an ω-model up to a certain size, then transforms into an ω-square model. It seems reasonable to consider that rough and bumpy fault planes of the ω-model become smooth for larger displacements and produce faulting in accordance with the ω-square model which explains the geologic observations on earthquake faults.

As mentioned before, the ω-square model failed to explain Tsujiura's observation on two Aleutian earthquake pairs with magnitudes M_s 5.7 to 7.0. The model predicted a spectral ratio change of almost 10 times from 10 seconds to 100 seconds, while the observed showed a very small change, with a nearly constant value over the same period range. In terms of the revised model A, this result means that all these earthquakes probably had fault planes of the same size. This observation may be approximately explained by the revised model B, if the transition from a rough faulting to a smooth one takes place at larger displacements or for a larger fault size in the Aleutians than in other parts of the world.

Working models such as A and B, which predict the scaling effect on seismic spectrum over the complete frequency range and dynamic range of earthquake seismology, will relate observations on large earthquakes with those on small ones, and the observations at low frequencies with those at high frequencies.

4. SCALING LAW OF DISLOCATION TIME-FUNCTION

The source factor $A(\omega)$ of the far-field seismic spectrum can be written in terms of the dislocation $D(\vec{\xi},t)$, or the displacement discontinuity, specified as a function of time t and the point $\vec{\xi}$ on the fault plane $\sum$ as follows (Haskell 1964):

$$A(\omega) = \iint_{\Sigma} \dot{D}(\vec{\xi},\omega)\ e^{-i\frac{\omega r}{\alpha}}\ d\Sigma_{\xi} \qquad (1)$$

where $\dot{D}(\vec{\xi},\omega)$ is the Fourier transform of the dislocation velocity $\dot{D}(\vec{\xi},t)$, r is the distance to the observer from the surface element $d\Sigma_{\xi}$, and α is the velocity of waves.

At low frequencies, where the change of $\frac{\omega r}{\alpha}$ within Σ is negligible, the far-field spectrum is simply proportional to the spectrum of dislocation velocity integrated over the fault plane. Therefore, the average value of dislocation velocity spectrum may be obtained by dividing $A(\omega)$ by the fault area.

For the inversion at higher frequencies, we shall assume a simple model of one-dimensional rupture propagation, such as considered by Ben-Menahem (1961), Haskell (1964) and Aki (1967). In that case, equation (1) is replaced by

$$A(\omega) = W \int_{0}^{L} \dot{D}(\xi,\omega)\ e^{-i\frac{\omega r}{\alpha}}\ d\xi \qquad (2)$$

where ξ is the coordinate along the path of rupture propagation, L is the final fault length, W is the width, and dislocation $D(\xi,\omega)$ is considered as the average value over the width.

For a uniform dislocation with constant propagation

velocity used by Ben-Menahem (1961),

$$\dot{D}(\xi,t) = \dot{D}(t - \frac{\xi}{v})$$

and therefore,

$$A(\omega) = W \int_0^L \dot{D}(\omega)\, e^{-\frac{i\omega\xi}{v} - i\frac{\omega r}{\alpha}}\, d\xi \qquad (3)$$

$$|A(\omega)| \doteq |\dot{D}(\omega)| \cdot WL \cdot \frac{\sin x}{x}$$

where $x = \frac{L\omega}{2}\left(\frac{1}{v} - \frac{\cos\theta}{\alpha}\right)$, and θ is the angle between the ξ-axis and the direction to the observer. For high frequencies, therefore, the far-field spectrum is proportional to the fault area, the dislocation velocity spectrum and ω^{-1}. The same result is obtained for the incoherent propagation models used by Haskell and Aki, for frequencies beyond the corner frequency. Thus, on the assumption of one-dimensional rupture propagation, one can obtain the spectrum of dislocation velocity at frequencies higher than the corner frequency by dividing the far-field spectrum by the fault area and multiplying it by frequency ω.

The validity of the above procedure should be subject to future critical investigations. If the rupture propagation is two-dimensional as considered by Berckhemer (1962),

Hirasawa & Stauder (1965) and Savage (1965), one should expect ω^{-2} effect beyond the corner frequencies. In that case, the correction should be multiplying ω^2, instead of ω. Of course, the two-dimensional propagation is more realistic because a fault is not a line but a plane. I feel strongly, however, that one of the corner frequencies must be much higher than the frequencies associated with the total time of rupture propagation and the rise time of fault slip, because otherwise, we expect that the -cube model explains the observation on the M_s - M_b relation, but it doesn't (Aki 1967). The second corner frequency of rupture propagation may be associated with a very short transient time of starting and stopping a primarily one-dimensional rupture propagation.

Now let us apply our tentative procedure of inversion to the far-field spectrum and find the scaling law of dislocation time-function. The spectral densities at low frequencies shown in Figs. 1, 9 and 11 are divided by the fault area (the square of the corner period). For frequencies higher than the corner frequency, an additional multiplication by a factor proportional to ω is applied. The resultant family of spectral curves for the dislocation velocity spectrum are shown in Figs. 12, 13 and 14, respectively for the ω-square model, revised model A and B.

It is remarkable that the absolute value of spectral

density of dislocation velocity at periods shorter than 5 seconds is independent of magnitude for earthquakes with $M_s > 6.5$ for all three models.

According to Haskell's (1969) calculation on the elastic near-field of fault motion, not only the maximum displacements but also the maximum velocity and acceleration takes place in the immediate vicinity of the fault plane. According to Aki's (1968) similar calculation, the seismic motion near a fault depends neither on fault length nor on fault width once they exceed certain limits, but is determined mostly by the dislocation time-function and velocity of rupture propagation. Since the rupture velocity is apparently independent of earthquake magnitude, we must conclude that the maximum seismic motion associated with an earthquake scales as the dislocation time-function.

Then, our results on the scaling law of dislocation time-function will have an important effect on earthquake engineering, because they imply that the maximum seismic motion of an earthquake in the period range less than 5 seconds is a constant independent of magnitude for $M_s > 6.5$.

It must be emphasized here that the above conclusion is supported only indirectly by observations. No mention has been made of any group of observations applying to the upper-left quarter of Figs. 1, 9 and 11. The waves in this quarter

are short waves coming from large earthquakes. They suffer not only from the complexity of a large source, but also from the complex path effect on short waves, and this makes the interpretation of the seismogram extremely difficult. Because of this difficulty, they have not attracted due attention. Housner (1955) considered a swarm of pulses random in time resulting from release of shear dislocations distributed randomly over a fault plane. Haskell (1964) introduced incoherent rupture propagation in order to account for observations on short waves from a large earthquake. The concept of a "multiple shock" is an old idea introduced to explain this most complex portion of a seismogram (Stoneley (1937), Usami (1956), Wyss & Brune (1967), Trifunac & Brune (1970), among others). Miyamura et al. (1965) summarize observations and discuss physical mechanisms.

The idea of a "multiple shock" implies that a large earthquake consists of a sequence of several small earthquakes occurring within the epicentral region. One must realize, however, the extremely large value of seismic moment for the largest earthquakes. For example, the Alaska earthquake of 1964 ($M = 8.5$, $M_o = 7.5 \times 10^{29}$ dyne cm) can be a multiple of several Rat Island earthquakes of 1965 ($M = 7.9$, $M_o = 1.2 \times 10^{29}$), but requires about 10,000 San Fernando earthquakes of 1971 ($M = 6.6$, $M_o = 7.5 \times 10^{25}$). The "multiple shock" model of a large earthquake will also have a scale effect on the spectrum; the spectrum at periods longer than the total duration of faulting

will increase proportionally with the number N of component events, but the high frequency spectrum will be proportional to $\sqrt{N}$ because of random interference. Thus, the spectral ratio between large and small earthquakes at low frequency will be the square of the ratio at high frequencies. This scale effect is the same as that of the ω-model of Brune & King (see Fig. 5). As discussed earlier, observations for large earthquakes are in favor of the ω-square model, which predicts that the spectral ratio at low frequency is the cube of the ratio at high frequency. The idea of "multiple shock" for large earthquakes is not compatible with our revised model B, in which small earthquakes are described by the ω-model, but large ones by a composite model of ω and ω-square.

Acknowledgments

The author is grateful to Dr. M. Tsujiura of the Earthquake Research Institute, University of Tokyo, for his generosity in letting the author use his latest result before publication. Dr. Kei Takano of the Geophysical Institute, University of Tokyo, kindly supplied the author with information on the recent developments in microearthquake spectral studies in Japan.

This work was supported in part by the National Science Foundation under Grant GA 24268, and in part by the Advanced

Research Projects Agency monitored by the Air Force Office of Scientific Research through contract F 44620-71-C-0049.

FIGURE CAPTIONS

FIGURE 1 Source factor of far-field seismic spectral density from earthquakes with various M_s for the ω-square model reproduced from Aki (1967).

FIGURE 2 Fault length L as a function of magnitude reproduced from Chinnery (1969) with the additional curve for the ω-square model. See text for the curves designated by the names of investigators.

FIGURE 3 The product of fault length L and the square of offset D as a function of magnitude reproduced from King & Knopoff (1968), with the additional curve for the ω-square model.

FIGURE 4 Seismic moment as a function of magnitude reproduced from Aki (1972) with additional lines (A') and (B) for the ω-model of Brune & King (1967) as described in text.

FIGURE 5 Schematic representation of the scaling law of seismic spectrum based on the ω-model of Brune & King (1967).

FIGURE 6 Locations of earthquake pairs with spectral ratios consistent with the ω-square model (designated by solid circles) and those inconsistent (designated by crosses).

FIGURE 7 Comparison of observed $M_s - M_b$ relation with the one predicted for the ω-square model.

FIGURE 8 Theoretical $M_s - M_b$ relation for the ω-square model as compared with empirical formulas of Gutenberg-Richter (1956) and Evernden et al. (1971) for earthquakes and that of Thirlaway-Carpenter (1966) for explosions.

FIGURE 9 Source factor of far-field seismic spectral density from earthquakes with various M_s for the revised model A.

FIGURE 10 Theoretical M_s versus corner-frequency relation for the ω-square model as compared with those implied by the $M_s - M_b$ relations of Gutenberg-Richter (1956) and Evernden et al. (1971).

FIGURE 11 Source factor of far-field seismic spectral density from earthquakes with various M_s for the revised model B.

FIGURE 12 Spectral densities of dislocation velocity for different M_s based on the ω-square model.

FIGURE 13 Spectral densities of dislocation velocity for different M_s based on the revised model A.

FIGURE 14 Spectral densities of dislocation velocity for different M_s based on the revised model B.

REFERENCES

Abe, K., 1970. Determination of seismic moment and energy from the earth's free oscillation, Phys. Earth Planet. Interiors, 4, 49-61.

Aki, K., 1966. Generation and propagation of G waves from the Niigata earthquake of June 16, 1964, Bull. Earthq. Res. Inst., Univ. Tokyo, 44, 23-88.

Aki, K., 1967. Scaling law of seismic spectrum, J. Geophys. Res., 72, 1217-1231.

Aki, K., 1968. Seismic displacements near a fault, J. Geophys. Res., 73, 5359-5376.

Aki, K., 1969. Analysis of the seismic coda of local earthquakes as scattered waves, J. Geophys. Res., 74, 615-631.

Aki, K., 1972. Earthquake Mechanism, Proceeding of the Final UMP Symposium, Moscow 1971, ed. by R. Ritsema.

Archambeau, C., 1968. General theory of elastodynamic source fields, Rev. Geophys., 6, 241-288.

Asada, T., 1957. Observations of nearby microearthquakes with ultra-sensitive seismometers, J. Phys. Earth, 5, 83-113.

Asada, T. & Takano, K., 1963. Attenuation of short-period P waves in the mantle, J. Phys. Earth, 11, 25-34.

Basham, P.W., 1969. Canadian magnitudes of earthquakes and nuclear explosions in south-western North America, Geophys. J., 17, 1-13.

Båth, M., & Duda, S.J., 1964. Earthquake volume, fault plane area, seismic energy, strain, deformation and related quantities, Ann. Geofis. Rome, 17, 353-368.

Benioff, H., 1951. Earthquakes and rock creep, Part I: creep characteristics of rocks and the origin of aftershocks, Bull. Seismol. Soc. Am., 41, 31-62.

Ben-Menahem, A., 1961. Radiation of seismic surface waves from finite moving sources, Bull. Seismol. Soc. Am., 51, 401-435.

Ben-Menahem, A., & Toksöz, M.N., 1963. Source mechanism from spectrum of long-period surface waves: 2. Kamachatka earthquake of November 5, 1952, J. Geophys. Res., 68, 5207-5222.

Berckhemer, H., 1962. Die Ausdehnung der Bruchfläche im Erdbebenherd und ihr Einfluss auf das seismiche Wellenspektrum, Gerlands Beitr. Geophys., 71, 5-26.

Brune, J.N., 1968. Seismic moment, seismicity, and rate of slip along major fault zones, J. Geophys. Res., 73, 777-784.

Brune, J.N., 1970. Tectonic stress and the spectra of seismic shear waves from earthquakes, J. Geophys. Res., 75, 4997-5009.

Brune, J.N., 1971. Seismic sources, fault plane studies and tectonics, Trans. Am. Geophys. Union, 52, 178-187.

Brune, J.N., Correction to "Tectonic stress and the spectra of seismic shear waves from earthquakes," J. Geophys. Res., 76, 5002.

Brune, J.N., & Allen, C.R., 1967. A low-stress-drop, low-magnitude earthquake with surface faulting: The Imperial, California, earthquake of March 4, 1966, Bull. Seismol. Soc. Am., 57, 501-514.

Brune, J.N., & Engen, G., 1969. Excitation of mantle Love waves and definition of mantle wave magnitude, Bull. Seismol. Soc. Am., 59, 923-933.

Brune, J.N., & King, D.Y., 1967. Excitation of mantle Rayleigh waves of period 100 seconds as a function of magnitude, Bull. Seismol. Soc. Am., 57, 1355-1365.

Capon, J., Greenfield, R.J. & Lacoss, R.T., 1967. Surface-versus body-wave magnitude results, in Semiannual Technical Summary, Lincoln Laboratories, M.I.T., pp. 3-5, Lexington, Mass., June 30.

Chalturin, V.I., Sept. 1970. Proceeding of Eurpopean Eng. Seismological Commission, Sofia, Bulgaria.

Chinnery, M., 1964. The strength of the earth's crust under horizontal shear stress, J. Geophys. Res., 69, 2085-2089.

Douglas, B.M., & Ryall, A., 1972. Spectral characteristics and stress drop for microearthquakes near Fairview Peak, Nevada, J. Geophys. Res., 77, 351-359.

Evernden, J.F., Best, W.J., Pomeroy, P.W., McEvilly, T.V., Savino, J.M., & Sykes, L.R., 1971. Discrimination between small-magnitude earthquakes and explosions, J. Geophys. Res., 76, 8042-8055.

Filson, J., & McEvilly, T.V., 1967. Love wave spectra and the mechanism of the 1966 Parkfield sequence, Bull. Seismol. Soc. Am., 57, 1245-1257.

Furuya, I.,1969. Predominant period and magnitude, J. Phys. Earth, 17, 119-126.

Gutenberg, B., & Richter, C.F., 1956. Earthquake magnitude, intensity, energy, and acceleration, 2, Bull. Seismol. Soc. Am., 46, 105-145.

Haskell, N., 1964. Total energy and energy spectral density of elastic wave radiation from propagating faults, Bull. Seismol. Soc. Am., 56, 1811-1842.

Haskell, N., 1966, Total energy and energy spectral density of elastic wave radiation from propagating faults, 2, A statistical source model, Bull. Seismol. Soc. Am., 56, 125-140.

Haskell, N., 1969. Elastic displacements in the near-field of a propagating fault, Bull. Seismol. Soc. Am., 59, 865-908.

Hirasawa, T., & Stauder, W., 1965. On the seismic body waves from a finite moving source, Bull. Seismol. Soc. Am., 55, 237-262.

Housner, G.W., 1955. Properties of strong ground motion earthquakes, Bull. Seismol. Soc. Am., 45, 197-218.

Ida, Y., & Aki, K., 1972. Seismic source time function of propagating longitudinal-shear cracks, J. Geophys. Res., 76 (in press).

Iida, K., 1959. Earthquake energy and earthquake fault, J. Earth Sci., Nagoya Univ., 7, 98-107.

Iida, K., 1965. Earthquake magnitude, earthquake fault, and source dimensions, J. Earth Sci., Nagoya Univ., 13, 115-132.

Kanai, K., & Yoshizawa, S., 1958. The amplitude and the period of earthquake motions, Bull. Earthq. Res. Inst., 36, 275-293.

Kanamori, H., 1970a. Synthesis of long-period surface waves and its application to earthquake source studies - Kurile Islands earthquake of October 13, 1963. J. Geophys. Res., 75, 5011-5027.

Kanamori, H., 1970b. The Alaska earthquake of 1964: Radiation of long-period surface waves and source mechanism, J. Geophys. Res., 75, 5029-5040.

Kanamori, H., 1971. Seismological evidence for a lithospheric normal faulting - the Sanriku earthquake of 1933, Phys. Earth Planet. Interiors, 4, 289-300.

King, C.Y., & Knopoff, L., 1968. Stress drop in earthquakes, Bull. Seismol. Soc. Am., 58, 249-257.

Lieberman, R.C., & Basham, P.W., 1971. Excitation of surface waves by the Aleutian underground explosion Milrow (October 2, 1969), J. Geophys. Res., 76, 4030-4034.

Lieberman, R.C., King, C.Y., Brune, J.N., & Pomeroy, P.W., 1966. Excitation of surface waves by the underground nuclear explosion Long Shot, J. Geophys. Res., 71, 4333-4339.

Lieberman, R.C., & Pomeroy, P.W., 1967. Excitation of surface waves by events in southern Algeria, Science, 156, 1098-1100.

Lieberman, R.C., & Pomeroy, P.W., 1969. Relative excitation of surface waves by earthquakes and underground explosions, J. Geophys. Res., 74, 1575-1590.

Lieberman, R.C., & Pomeroy, P.W., 1970. Source dimensions of

small earthquakes as determined from the size of after-shock zone, Bull. Seismol. Soc. Am., 60, 879-896.

Linde, A.T., & Sacks, I.S., 1971. Errors in the spectral analysis of long-period seismic body waves, J. Geophys. Res., 76, 3226-3336.

Miyamura, S., Omote, S., Teisseyre, R., & Vesanen, E., 1965. Multiple shocks and earthquake series pattern, Bull. Intern. Inst. Seis. Earthq. Eng., 2, 71-92.

Mogi, K., 1962. The influence of the dimensions of specimens on the fracture strength of rocks - comparison between the strength of rock specimens and that of the earth's crust, Bull. Earthq. Res. Inst., Univ. Tokyo, 40, 175-185.

Molnar, P., Savino, J., Sykes, L.R., Lieberman, R.C., Hade, G., & Pomeroy, P.W., 19 . Small earthquakes and explosions in western North America recorded by new high-gain, long-period seismographs, Nature, 224, 1268-1273.

Otsuka, M., 1965. Earthquake magnitude and surface fault formation, J. Seis. Soc. Japan, Ser. 2, 18, 1-8.

Press, F., 1967. Dimensions of the source region for small shallow earthquakes, Proceedings of the VESIAC Conference on the Current Status and Future Progress for Understanding the Source Mechanism of Shallow Seismic Events in the 3 to 5 Magnitude Range.

Savage, J.C., 1966. Radiation from a realistic model of faulting, Bull. Seismol. Soc. Am., 56, 577-592.

Stauder, W., 1968. Tensional character of earthquake foci beneath the Aleutian trench with relation to sea-floor spreading, J. Geophys. Res., 73, 7693-7701.

Stoneley, R., 1937. The Mongolian earthquake of 1931, August 10. Brit. Ass. Seis. Comm. 42nd Rep., 5-6.

Takano, K., 1970. Attenuation of short period seismic waves in the upper mantle and its regional difference, J. Phys. Earth, 18, 171-180.

Takano, K., 1971. A note on the attenuation of short period P and S waves in the mantle, J. Phys. Earth, 19, 155-164.

Takano, K., 1971. Analysis of seismic coda waves of ultra microearthquakes in the Matsushiro area - a comparison with Parkfield, California, J. Phys. Earth, 19, 209-215.

Terashima, T., 1968. Magnitude of microearthquake and the spectra of microearthquake waves, Bull. Intern. Inst. Seism. Earthq. Eng., 5, 31-108.

Thirlaway, H.I.S., & Carpenter, E.W., 1966. Seismic signal anomalies, travel times, amplitudes, and pulse shapes, Proceedings of the VESIAC Special Study Conference on Seismic Signal Anomalies, Travel Times, Amplitudes, and Pulse Shapes, Beaugency, France, October.

Tocher, D., 1958. Earthquake energy and ground breakage, Bull. Seismol. Soc. Am., 48, 147-152.

Tocher, D., 1960. Movement on faults, Proc. 2nd World Conf. Earthquake Engineering, 1, 551-564.

Trifunac, M., & Brune, J.N., 1970. Complexity of energy release during the Imperial Valley, California, earthquake of 1940, Bull. Seismol. Soc. Am., 60, 137-160.

Tsai, Y.B., & Aki, K., 1969. Simultaneous determination of the seismic moment and attenuation of seismic surface waves, Bull. Seismol. Soc. Am., 59, 275-287.

Tsai, Y.B., & Aki, K., 1970a. Source mechanism of the Truckee, California earthquake of September 12, 1966, Bull. Seismol. Soc. Am., 60, 1199-1208.

Tsai, Y.B., & Aki, K., 1970b. Precise focal depth determination from amplitude spectra of surface waves, J. Geophys. Res., 75, 5729-5743.

Tsai, Y.B., & Aki, K., 1971. Amplitude spectra of surface waves from small earthquakes and underground nuclear explosions, J. Geophys. Res., 76, 39 0-3952.

Tsuboi, C., 1940. Isostasy and maximum earthquake energy, Proc. Imp. Acad., 16, 449.

Tsuboi, C., 1956. Earthquake energy, earthquake volume, aftershock area and strength of the earth's crust, J. Phys. Earth, 4, 63.

Tsuboi, C., 1958. On seismic activities in and near Japan, "Contributions in Geophysics: in honor of Beno Gutenberg," Pergamon Press.

Tsuboi, C., 1965. A theoretical derivation of the magnitude-energy equation of earthquakes, log E = aM + b, Proc. Japan Acad., 41, 588.

Tsujiura, M., 1966. Frequency analysis of seismic waves (1), Bull. Earthq. Res. Inst., Tokyo Univ., 44, 873-891.

Tsujiura, M., 1967. Frequency analysis of seismic waves (2), Bull. Earthq. Res. Inst., Tokyo Univ., 45, 973-995.

Tsujiura, M., 1969. Regional variation of P wave spectra (1), Bull. Earthq. Res. Inst., Tokyo Univ., 47, 613-633.

Tsujiura, M., 1972. Spectrum of seismic waves and its dependence on magnitude (1), Bull. Earthq. Res. Inst., Tokyo Univ. (in press).

Usami, T., 1956. Seismometrical study of Boso-oki earthquake of November 26, 1953, Quart. J. Seismology (Kenshin-Jiho) Japan Meteor. Agency, 21, 3.

Wyss, M., 1970. Observation and interpretation of tectonic strain release mechanisms, Ph.D. thesis, Calif. Inst. of Technology.

Wyss, M., & Brune, J.N., 1967. The Alaska earthquake of 28 March 1964: A complex multiple rupture, Bull. Seismol. Soc. Am., 57, 1017-1023.

Wyss, M., & Brune, J.N., 1968. Seismic moment, stress, and source dimensions for earthquakes in the California-Nevada region, J. Geophys. Res., 73, 4681-4694.

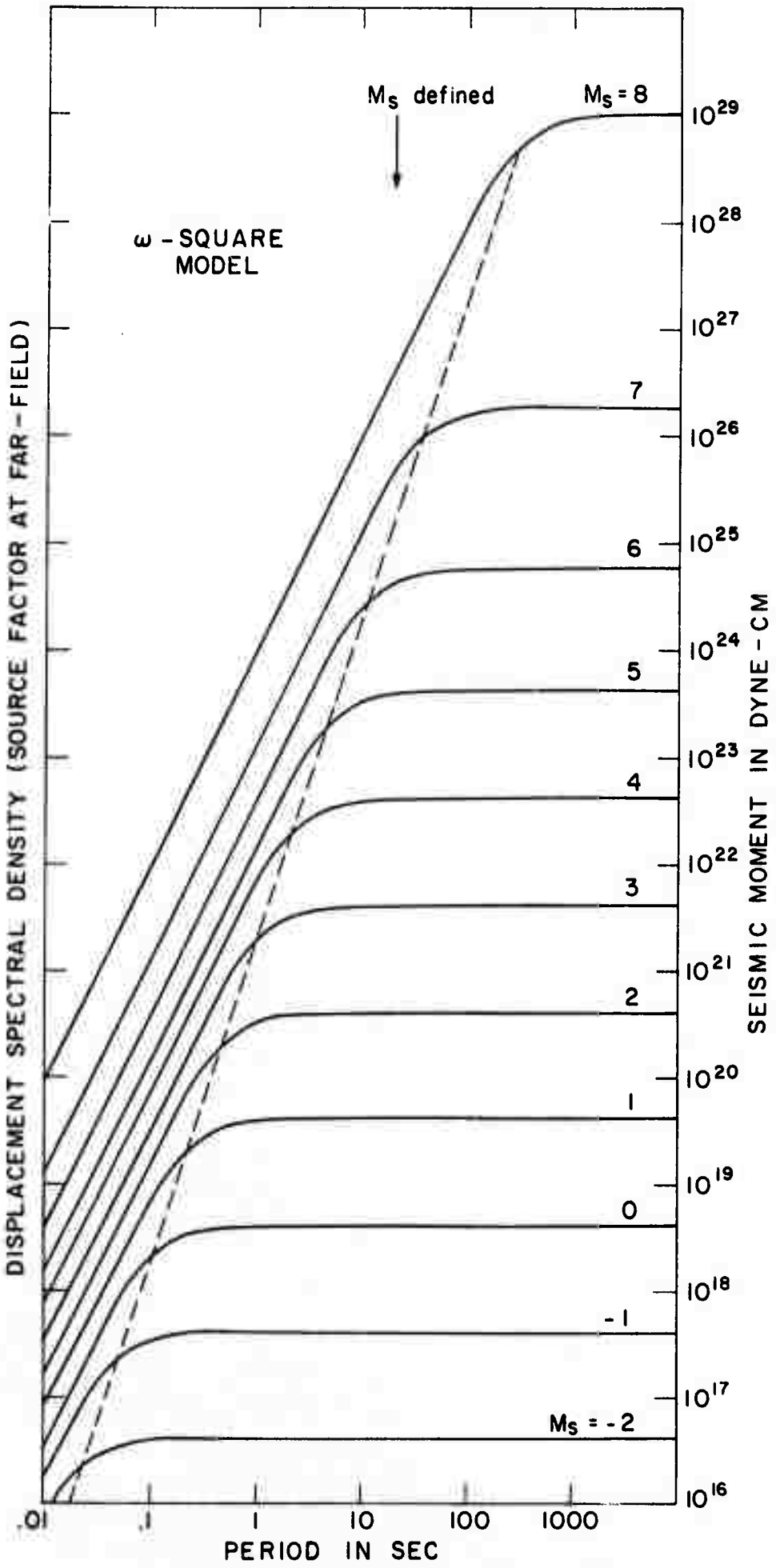
M_S defined
$M_S = 8$
ω - SQUARE MODEL
7
6
5
4
3
2
1
0
-1
$M_S = -2$
DISPLACEMENT SPECTRAL DENSITY (SOURCE FACTOR AT FAR-FIELD)
SEISMIC MOMENT IN DYNE-CM
10^{29}
10^{28}
10^{27}
10^{26}
10^{25}
10^{24}
10^{23}
10^{22}
10^{21}
10^{20}
10^{19}
10^{18}
10^{17}
10^{16}
.01
.1
1
10
100
1000
PERIOD IN SEC

Fig. 1

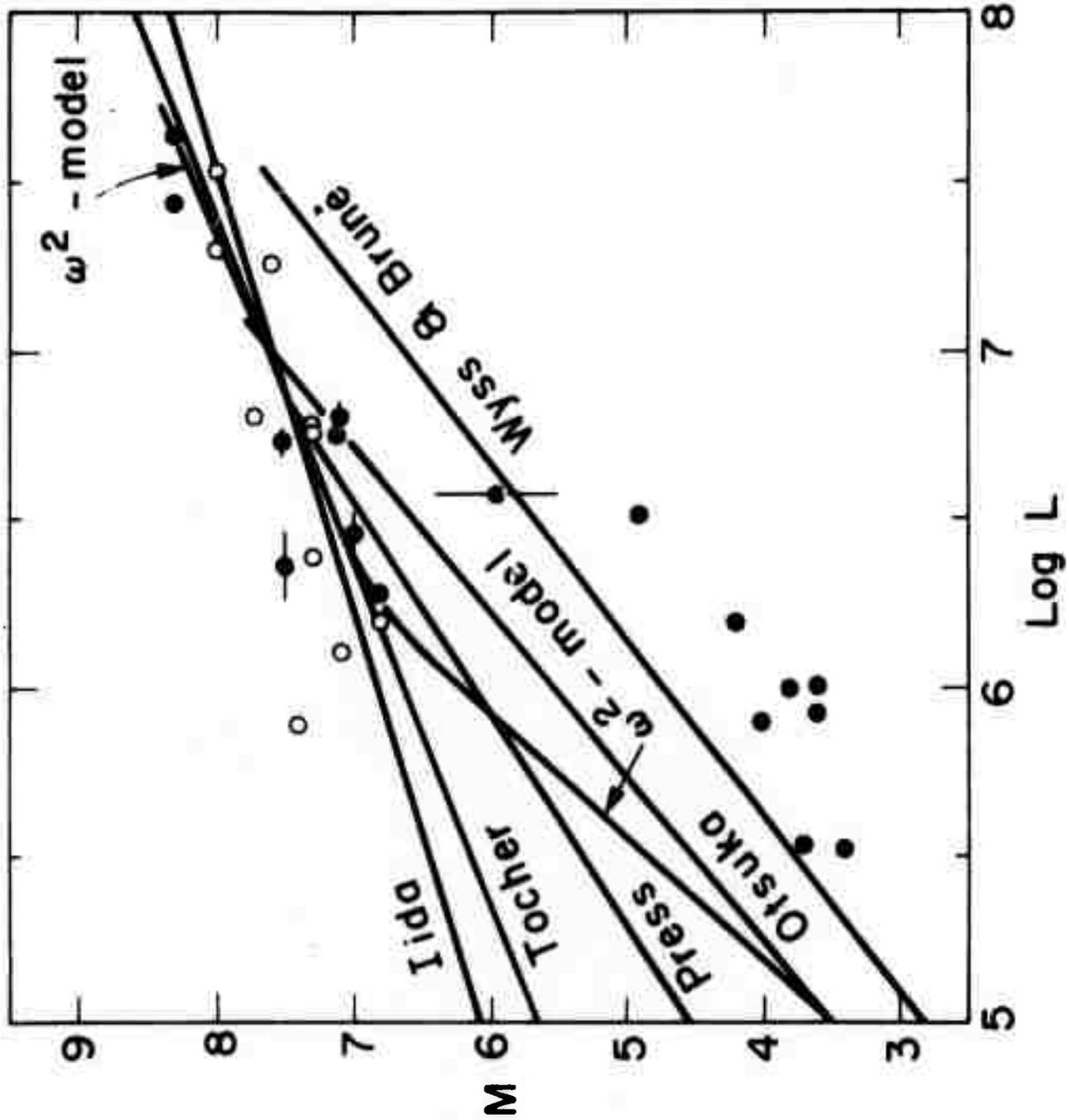
ω² - model
Wyss & Brune
ω² - model
Otsuka
Press
Tocher
Iida
M
Log L
9
8
7
6
5
4
3
5
6
7
8

Fig. 2

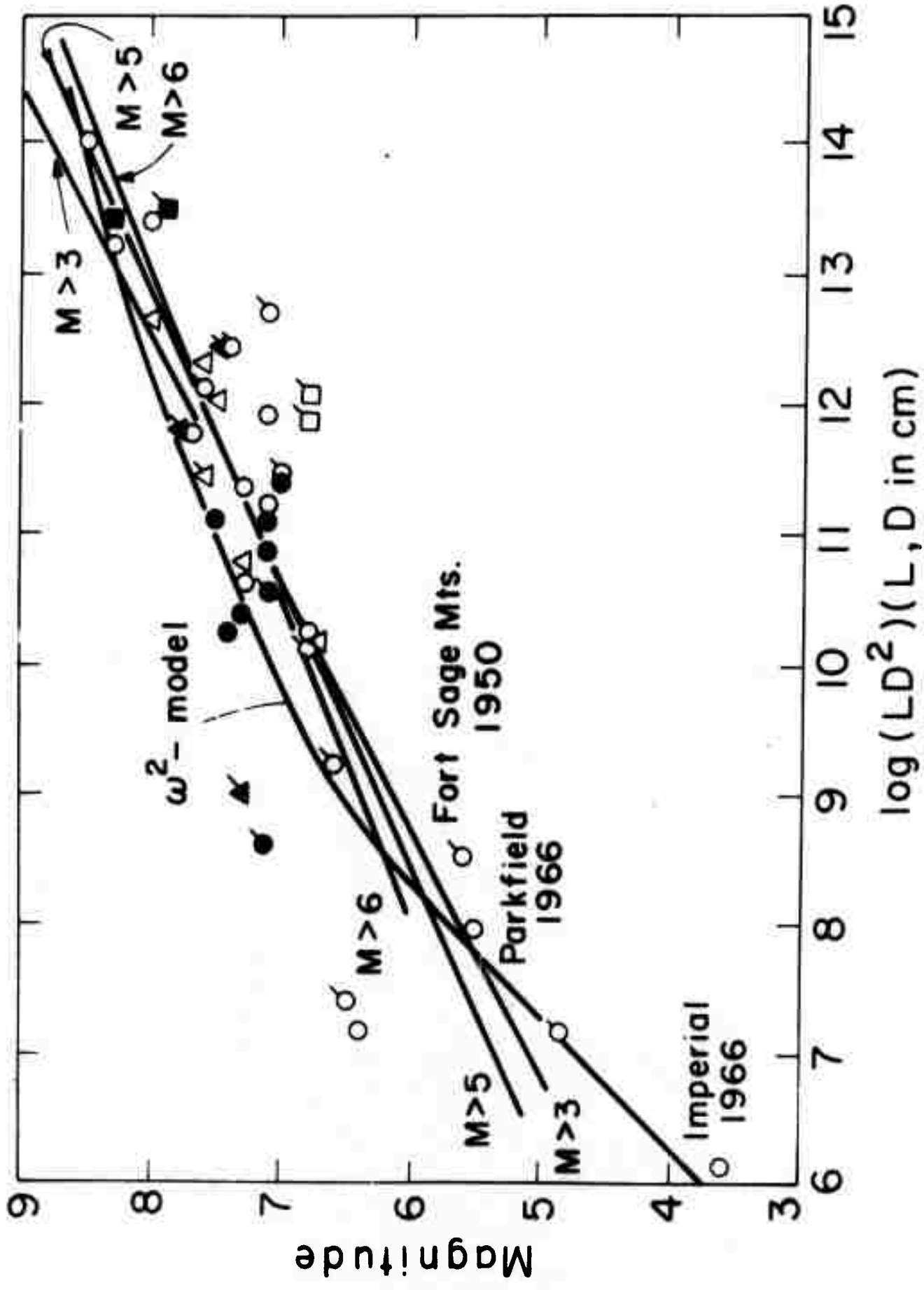
Magnitude
log (LD²)(L, D in cm)
M>3
M>5
M>6
ω²- model
Fort Sage Mts.
1950
Parkfield
1966
Imperial
1966

Fig. 3

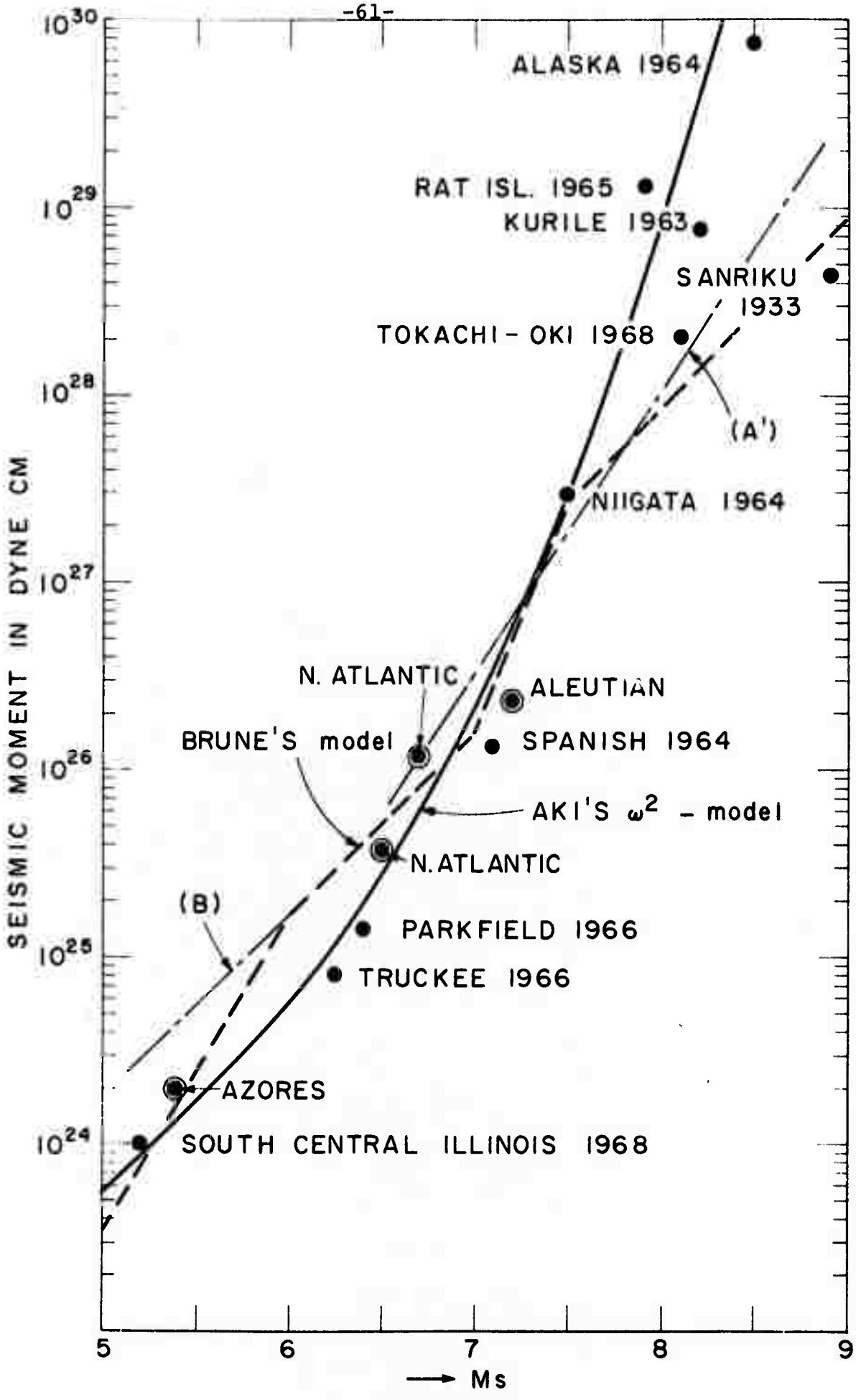
ALASKA 1964
RAT ISL. 1965
KURILE 1963
SANRIKU 1933
TOKACHI-OKI 1968
(A')
NIIGATA 1964
N. ATLANTIC
ALEUTIAN
BRUNE'S model
SPANISH 1964
AKI'S ω² - model
N. ATLANTIC
(B)
PARKFIELD 1966
TRUCKEE 1966
AZORES
SOUTH CENTRAL ILLINOIS 1968
SEISMIC MOMENT IN DYNE CM
10³⁰
10²⁹
10²⁸
10²⁷
10²⁶
10²⁵
10²⁴
5
6
7
8
9
Ms

Fig. 4

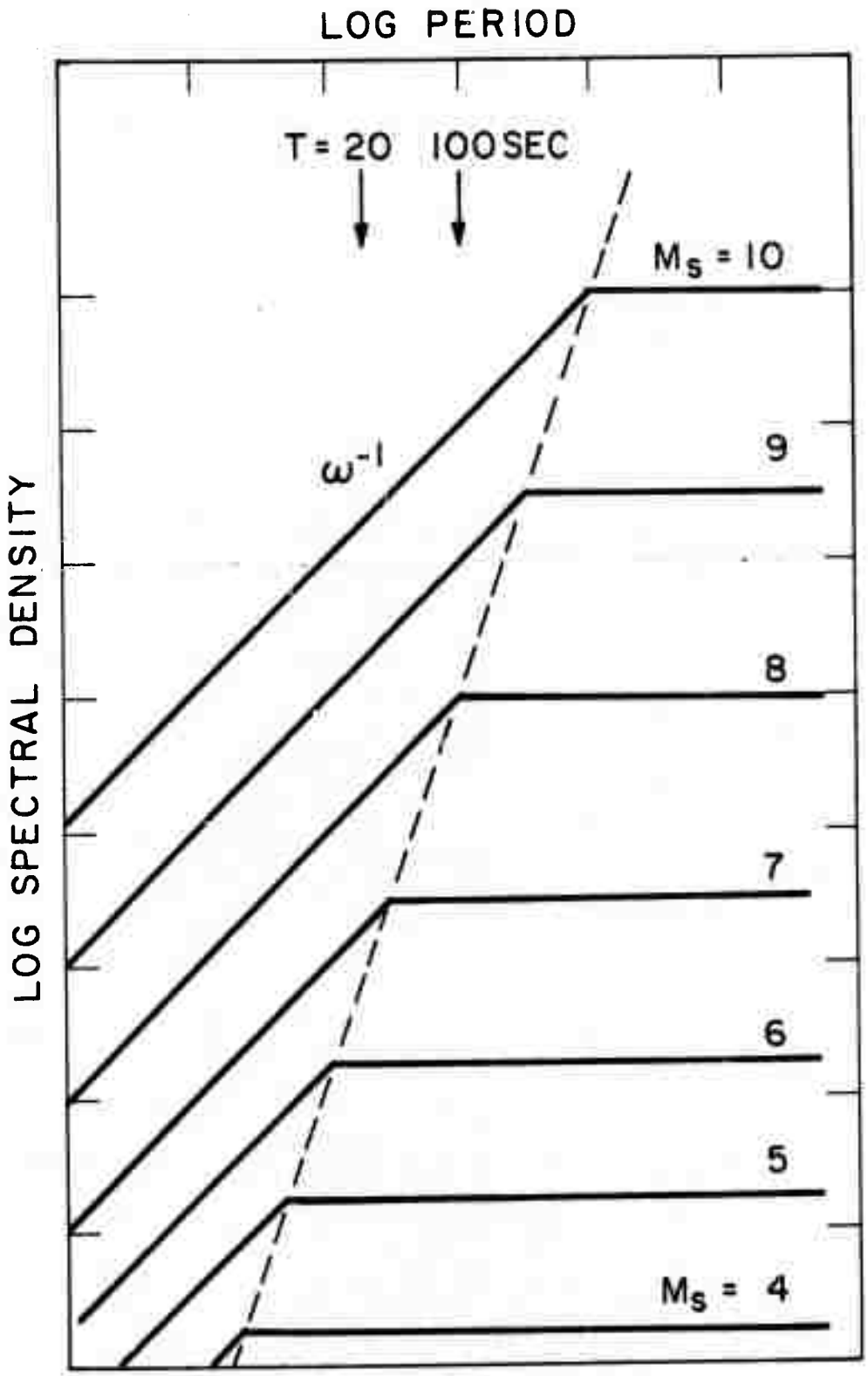
LOG PERIOD
T = 20
100 SEC
M_S = 10
9
8
7
6
5
M_S = 4
ω^{-1}
LOG SPECTRAL DENSITY

Fig. 5

Fig. 6

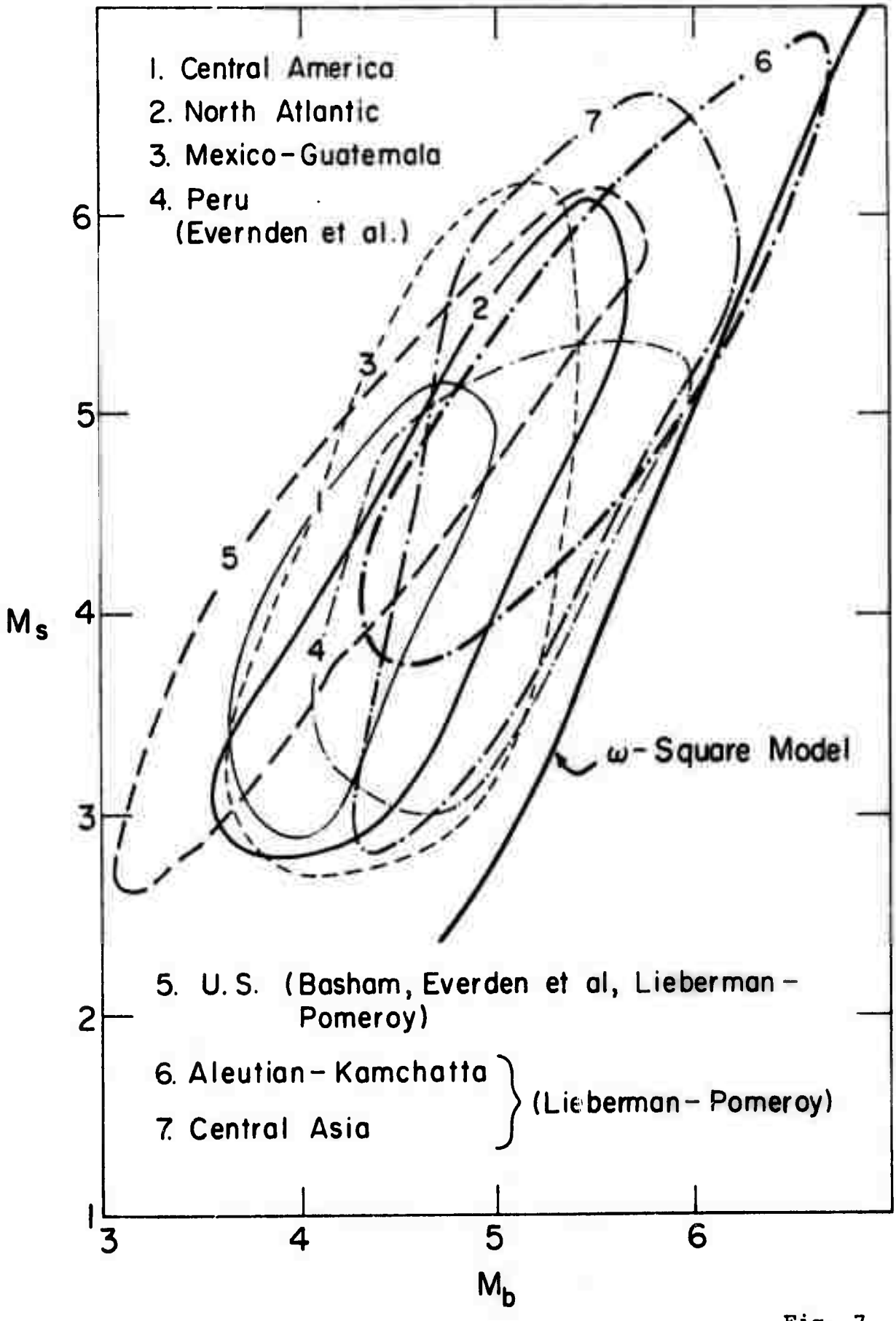
1. Central America
2. North Atlantic
3. Mexico-Guatemala
4. Peru
(Evernden et al.)
5. U.S. (Basham, Everden et al, Lieberman-Pomeroy)
6. Aleutian-Kamchatta
7. Central Asia
(Lieberman-Pomeroy)
ω-Square Model
M_s
M_b
1
2
3
4
5
6

Fig. 7

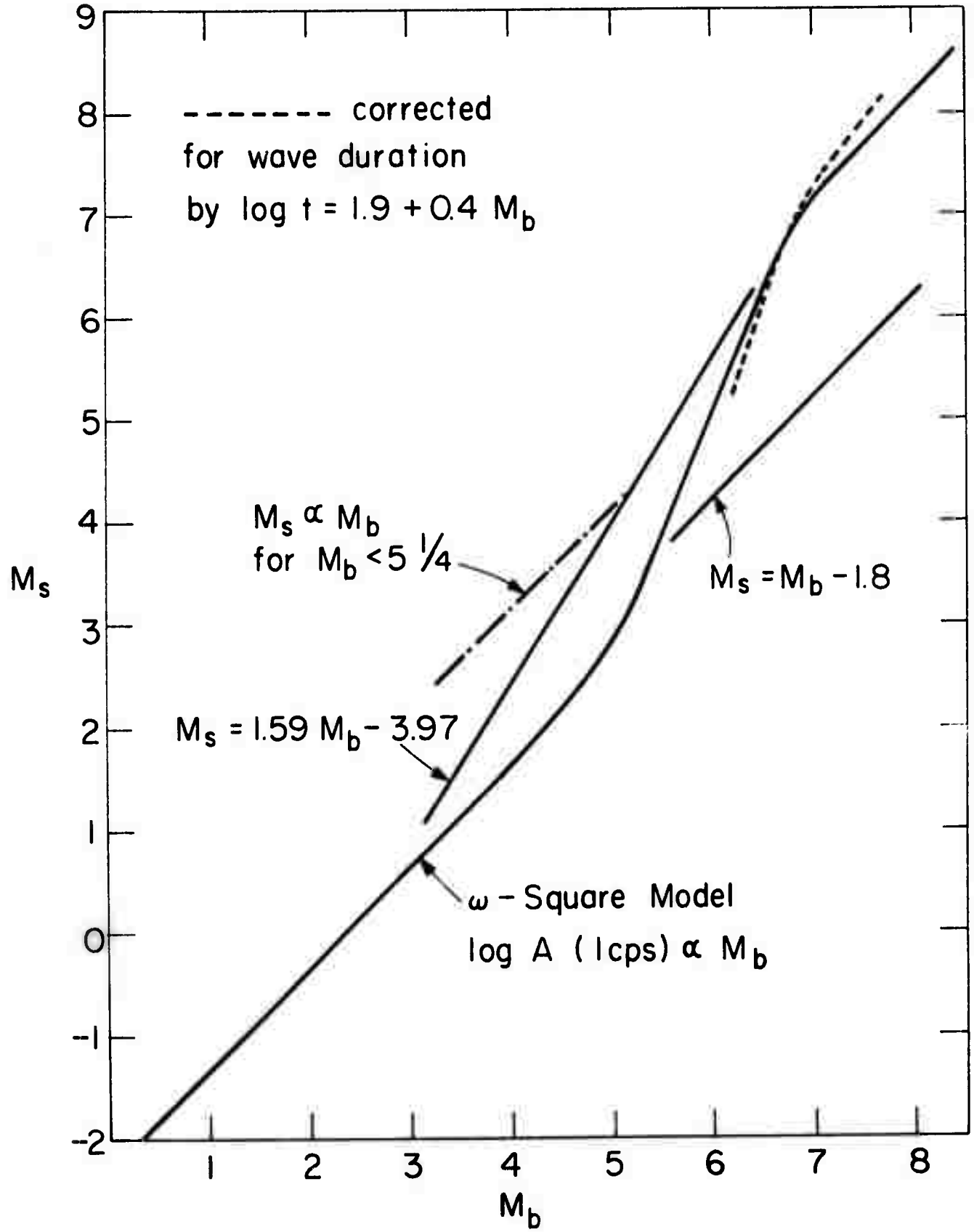
corrected
for wave duration
by log t = 1.9 + 0.4 M_b
$M_s \propto M_b$
for $M_b < 5\frac{1}{4}$
$M_s = M_b - 1.8$
$M_s = 1.59\, M_b - 3.97$
ω - Square Model
log A (1cps) $\propto M_b$
M_s
M_b
9
8
7
6
5
4
3
2
1
0
-1
-2
1
2
3
4
5
6
7
8

Fig. 8

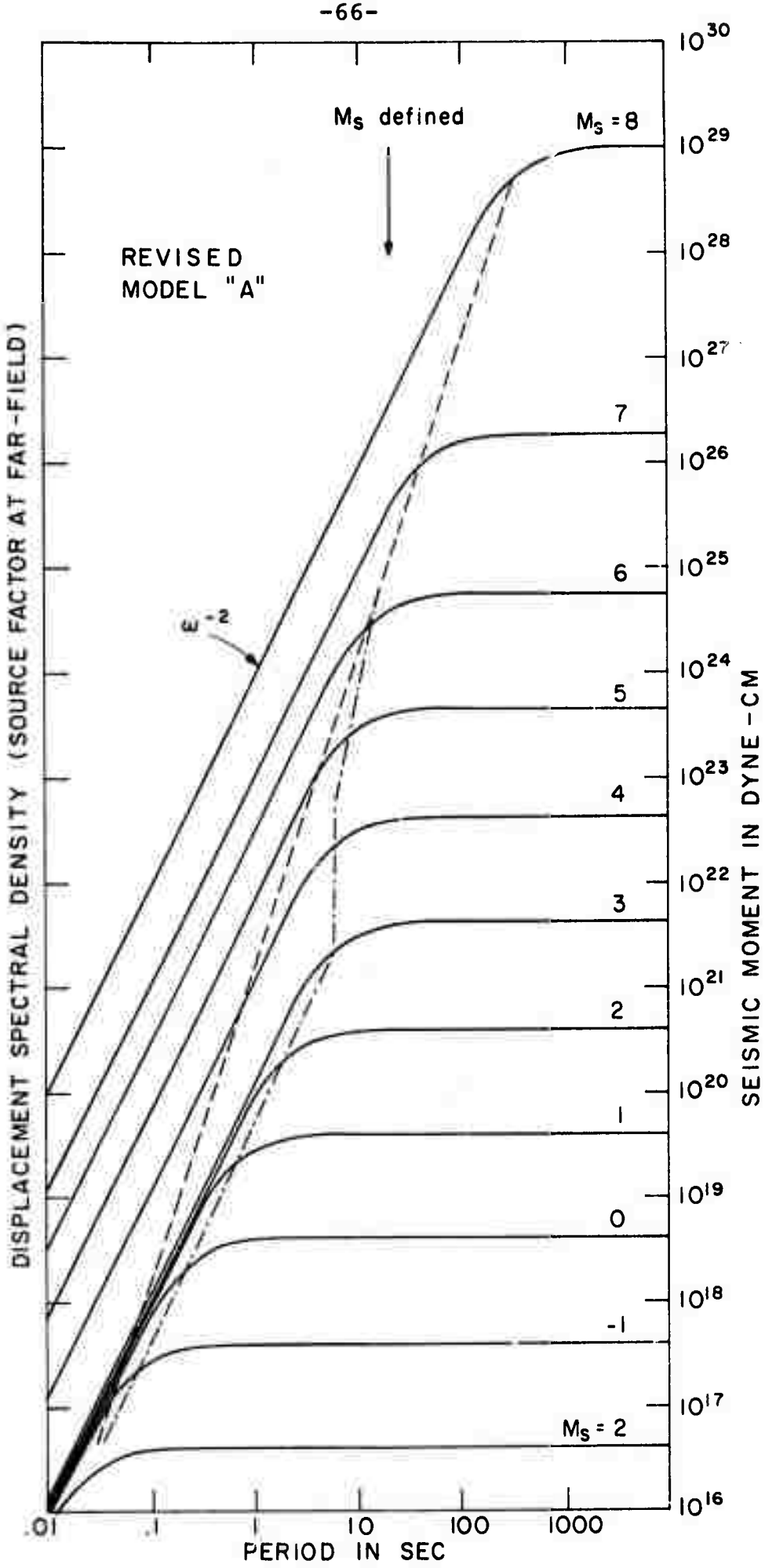
REVISED
MODEL "A"
M_S defined
$M_S = 8$
7
6
5
4
3
2
1
0
-1
$M_S = 2$
ω^{-2}
DISPLACEMENT SPECTRAL DENSITY (SOURCE FACTOR AT FAR-FIELD)
SEISMIC MOMENT IN DYNE-CM
10^{30}
10^{29}
10^{28}
10^{27}
10^{26}
10^{25}
10^{24}
10^{23}
10^{22}
10^{21}
10^{20}
10^{19}
10^{18}
10^{17}
10^{16}
.01
.1
1
10
100
1000
PERIOD IN SEC

Fig. 9

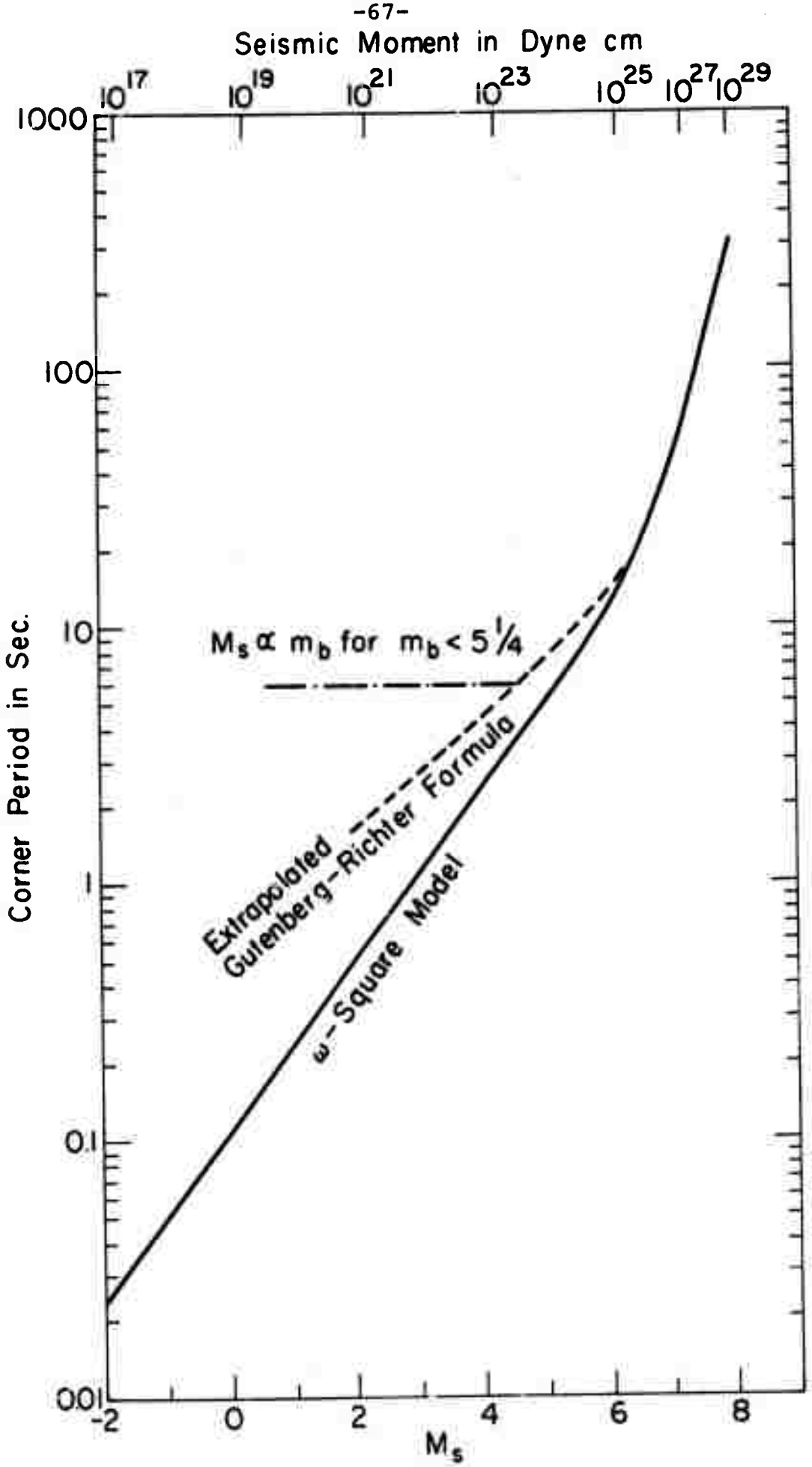
Seismic Moment in Dyne cm
10^{17}
10^{19}
10^{21}
10^{23}
10^{25}
10^{27}
10^{29}
1000
100
10
1
0.1
0.01
Corner Period in Sec.
$M_s \propto m_b$ for $m_b < 5\frac{1}{4}$
Extrapolated Gutenberg-Richter Formula
ω-Square Model
-2
0
2
4
6
8
M_s

Fig. 10

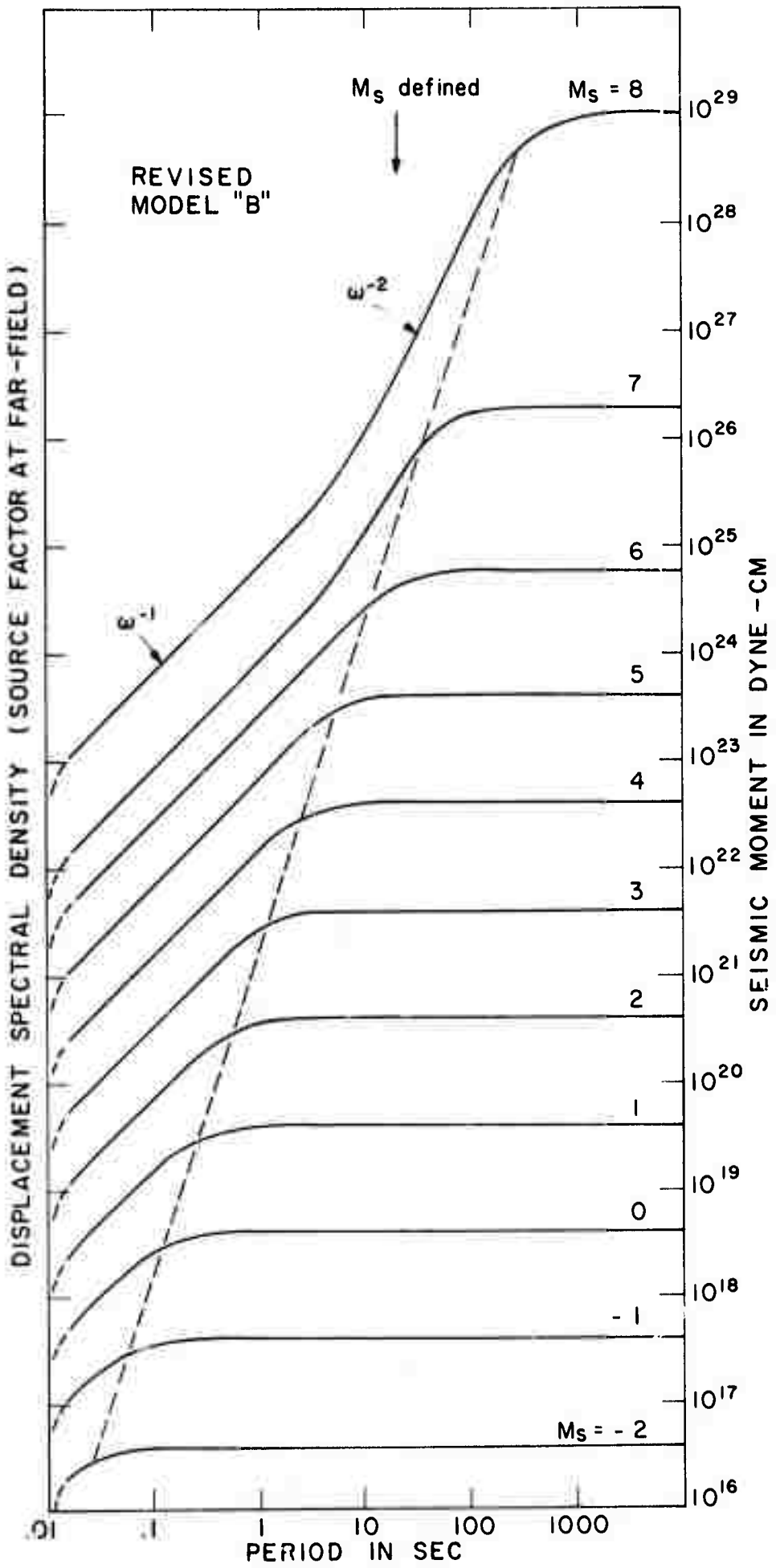
REVISED
MODEL "B"
M_S defined
M_S = 8
ω^{-2}
ω^{-1}
7
6
5
4
3
2
1
0
-1
M_S = - 2
10^{29}
10^{28}
10^{27}
10^{26}
10^{25}
10^{24}
10^{23}
10^{22}
10^{21}
10^{20}
10^{19}
10^{18}
10^{17}
10^{16}
DISPLACEMENT SPECTRAL DENSITY (SOURCE FACTOR AT FAR-FIELD)
SEISMIC MOMENT IN DYNE-CM
.01
.1
1
10
100
1000
PERIOD IN SEC

Fig. 11

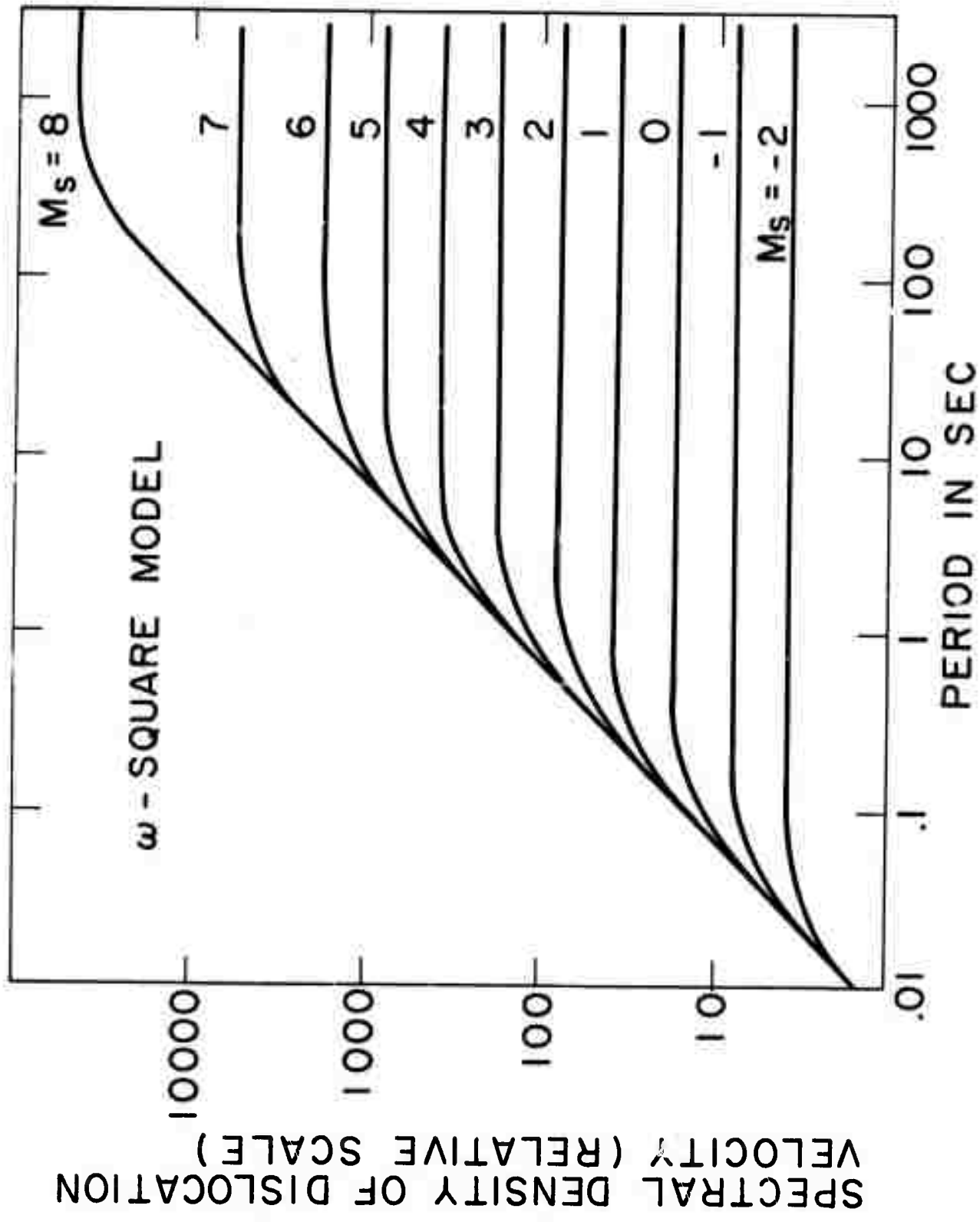
SPECTRAL DENSITY OF DISLOCATION
VELOCITY (RELATIVE SCALE)
10000
1000
100
10
.01
.1
1
10
100
1000
PERIOD IN SEC
ω - SQUARE MODEL
Ms = 8
7
6
5
4
3
2
1
0
-1
Ms = -2

Fig. 12

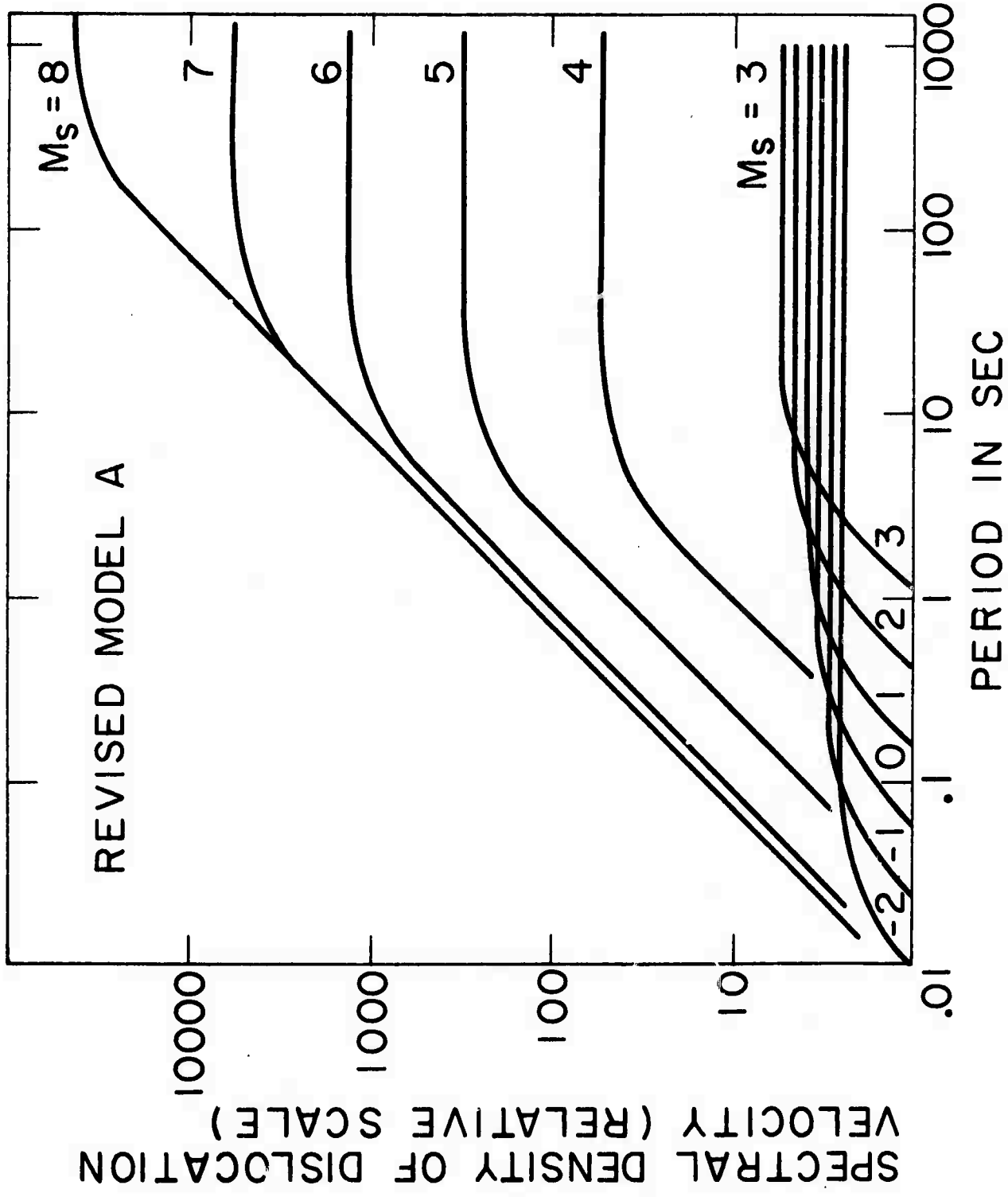
SPECTRAL DENSITY OF DISLOCATION VELOCITY (RELATIVE SCALE)
10000
1000
100
10
.01
REVISED MODEL A
M_S=8
7
6
5
4
M_S = 3
-2
-1
0
1
2
3
.1
1
10
100
1000
PERIOD IN SEC

Fig. 13

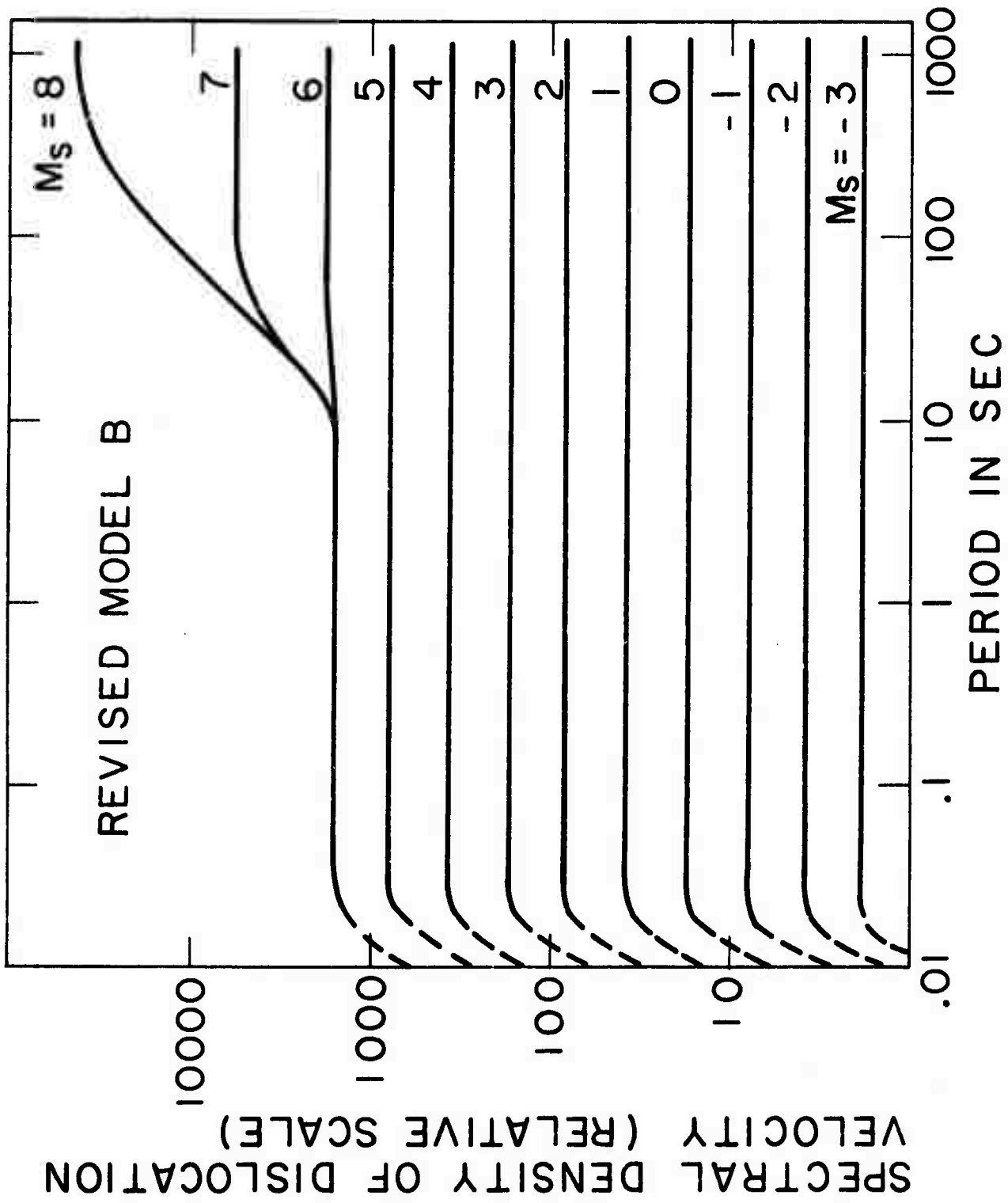
REVISED MODEL B
$M_S = 8$
7
6
5
4
3
2
1
0
-1
-2
$M_S = -3$
.01
.1
1
10
100
1000
PERIOD IN SEC
10000
1000
100
10
1
SPECTRAL DENSITY OF DISLOCATION
VELOCITY (RELATIVE SCALE)

Fig. 14

3.6 Tectonic Strain Release by Underground Nuclear Explosions and its Effect on Seismic Discrimination by M. Nafi Toksöz and Harold H. Kehrer

Summary

The analysis of surface waves from a large number of underground nuclear explosions reinforces the hypothesis of tectonic strain release. Such strain release is dependent on rock type and ambient stress levels. In harder media, such as granite, strain release is considerably greater than in soft media such as loose alluvium and salt. In the case of three events for which the tectonic component exceeded that of the explosion itself, the effect on the $M_S - m_b$ discriminant due to the added surface wave energy was not noticeable. This was probably due to the averaging of magnitude over all azimuths. A decaying pulse-type source-time function is consistent with surface wave amplitude spectra and can explain the long-period/short-period spectral ratio.

INTRODUCTION

The source mechanisms of underground nuclear explosions have been of great seismological interest since it was first observed that a pure explosive source alone could not adequately account for the radiation patterns of seismic waves recorded at distant stations. Most notable among these observations are the presence of SH and Love waves and azimuthal asymmetry of the Rayleigh wave radiation patterns. There have been a number of studies dealing with the radiation patterns and the generation of SH-type seismic waves by underground nuclear explosions (Press & Archambeau 1962; Brune & Pomeroy 1963; Aki 1964; Toksöz et al. 1964, 1965; Toksöz 1967; Archambeau 1968; Kehrer 1969; Molnar et al 1969; Archambeau & Sammis 1970; Toksöz & Kehrer 1971; Toksöz et al 1971). It is generally accepted that the Love waves are generated at or very near the source and that they may be associated with the release of tectonic strain energy by the explosion. As recent calculations by Leavy (1971) show, near-source inhomogeneities and scattering cannot account for the observed amplitudes of Love waves. Geological studies (McKeown et al 1966; Barosch 1968; Bucknam 1969; McKeown & Dickey 1969; Dickey 1968, 1969, 1971) clearly indicate fault movements and surface displacements associated with the majority of explosions. Aftershocks that follow the explosions (Hamilton & Healy

1969; Ryall & Savage 1969; Stauder 1971) generally resemble the sequence that follows earthquakes and they indicate the disturbance of the regional tectonic stress patterns by the explosion.

When observed outside the source region, seismic waves which are due to a tectonic strain release component will have spectral properties and radiation patterns similar to those of an earthquake. These will be superimposed on waves radiated isotropically by the pure explosive source. The questions that arise are: 1) what is the extent of tectonic strain energy release and 2) how significantly does this complication affect some of the seismic discriminants such as $M_s - m_b$ relationships? In this paper we address ourselves to these points.

The paper is divided into three parts. In Part I, we present the strain release characteristics of about 20 underground explosions. For this, we use Rayleigh wave radiation patterns as well as Love-to-Rayleigh wave amplitude ratios. We show the importance of medium properties and tectonic framework in controlling the energy release. In Part II, we evaluate the effect of the released strain energy on the surface wave magnitudes. Part III is devoted to a somewhat separate subject -- the source function of the explosion. A decaying pulse-type pressure function fits the observed surface spectra and explains the success of some of the spectral ratio discriminants.

I. TECTONIC STRAIN RELEASE CHARACTERISTICS OF EXPLOSIONS

Examples of Rayleigh and Love waves generated by three explosions are shown in Fig. 1. These illustrate the differences in the relative generation of Love waves by NTS (Nevada Test Site) explosions recorded at Weston, Massachusetts. Love waves appear on the tangential components (T), about two minutes earlier than the Rayleigh waves on the vertical components (2). The large amplitude of Love waves relative to Rayleigh waves for Pile Driver and Greeley indicates the greater amount of tectonic strain release by these explosions.

To determine the contribution of strain release on the radiated wave, we formulate a composite source consisting of a pure explosion plus a double-couple component representing the strain release. For such a source, the theoretical formulations for the azimuthal dependence of Rayleigh wave amplitudes and Love/Rayleigh amplitude ratios can be written as (Toksöz et al 1965, 1971; Kehrer 1969):

$$U_{Rz} = W_e \left[1 + F \left[\frac{1}{2}\sin\lambda \sin 2\delta \left[\frac{1+\sigma_o}{1-\sigma_o} - \cos 2\theta\right] + \cos\lambda \sin\delta \sin 2\theta\right]\right]$$

(1)

$$\frac{|U_{L\theta}|}{|U_{Rz}|} = \frac{Fk_L^{1/2}A_L\left[\frac{1}{2}\sin\lambda \sin 2\delta \sin 2\theta + \cos\lambda \sin\delta \cos 2\theta\right]}{\left[1 + F\left[\frac{1}{2}\sin\lambda \sin 2\delta \left[\frac{1+\sigma_o}{1-\sigma_o} - \cos 2\theta\right] + \cos\lambda \operatorname{sinc}\delta \sin 2\theta\right]\right] k_R^{1/2}A_R\left[\frac{\dot{u}_o^*}{\dot{w}_o}\right]} \exp\left[-r(\gamma_L - \gamma_R)\right]$$

where A_R and A_L are the Rayleigh and Love amplitude factors (Harkrider 1964); k_R and k_L are the Rayleigh and Love wave numbers; $\dot{u}_o$ and $\dot{w}_o$ are components of particle velocity at the surface; σ_o is Poisson's ratio at the surface; γ_R and γ_L are the Rayleigh and Love wave attenuation coefficients; δ and λ are the dip and slip directions of the fault plane; θ is its azimuth; and F is the strength of the double-couple relative to the explosion. In Eq. (1), the difference in explosion and earthquake source time functions and source dimensions are considered negligible.

For a horizontal double-couple, $\delta = 90°$ and $\lambda = 0°$ and we obtain

$$|U_{Rz}| = W_e \left(1 + F \sin 2\theta\right) \tag{2}$$

$$\frac{|U_{L\theta}|}{|U_{Rz}|} = \frac{F k_L^{1/2} A_L \cos 2\theta}{\left(1 + F \sin 2\theta\right) k_R^{1/2} A_R \left(\frac{u_o^*}{w_o}\right)} \exp\left[-r(\gamma_L - \gamma_R)\right]$$

In this study we use Eq. (2) to determine the strength of the double-couple (F value) and the orientation of the double-couple (θ) from Rayleigh wave amplitudes and Love/Rayleigh

amplitude ratios. Other quantities are computed theoretically for specified layered earth models (Harkrider, 1964)

Long-period seismograms were obtained from stations throughout North America for the study of the U. S. explosions. These included stations of the World Wide Standard Seismograph Network (WWSSN), the Long Range Seismic Measurements Network (LRSM), the Canadian Standard Seismograph Network (CSSN), and two additional stations at Berkeley and Pasadena which provided long-period data. Figure 2 shows the distribution of recording stations in North America. However, not all stations provided useful data for each event. For the presumed Soviet events, data was obtained from the WWSSN stations in Europe and Asia.

The film records of those events, for which the surface wave data were of sufficient quality, were digitized, band-pass filtered (8-60 sec) to reduce noise, and the two horizontal components were rotated to radial and tangential directions with respect to the epicenter. In this way essentially pure Love waves were obtained on the tangential component. Figure 3 is an example of this analysis for the explosion Boxcar recorded at Mould Bay, Canada. The three lower traces are plotted from digital data and show the unfiltered north-south, east-west, and vertical components. The three upper traces show the filtered data, where the horizontal components have been rotated to radial and tangential directions.

The tangential and the vertical components were then Fourier-analyzed to yield the amplitude spectra. The proper time windows for this analysis were determined by examining the filtered trace at each station individually and noting the onset and duration of the wave trains.

Love wave to Rayleigh wave amplitude ratios were determined by computing the spectral ratio of the tangential component to the vertical component over the period range 8 to 60 seconds. In general, the spectral ratios were somewhat oscillatory and thus the ratio at any one particular period could not be expected to be reliable at all stations. The period range was, therefore, divided into three bands, from 9 to 15 sec, from 15 to 22 sec, and from 22 to 30 sec. The average value of the ratio in each band was then taken to represent the ratio over that band.

An automatic error scheme (Kehrer 1969) was used to determine the best fit of Eq. (2) to the observed data. In applying Eq. (2), the term $k_L^{1/2}A_L/k_R^{1/2}A_R(\frac{u_o^*}{w_o})$ was taken to be a constant at all stations. An error term E was then formed between the observed and the theoretical ratios for combinations of F and θ.

$$E_j = \left[\sum_{i=1}^{n} \left(\frac{L_i}{R_i} - \left| \frac{S \cdot F_j \cos 2\theta_{ij}}{1 + F_j \sin 2\theta_{ij}} \right| \right)^2 / N \right]^{1/2} \qquad (3)$$

The jth combination of F and θ which fits the data best will be that which minimizes E. L_i/R_i is the experimentally measured Love wave to Rayleigh wave amplitude ratio at a particular station i, S is a constant, and N is the number of stations. The values of E were contoured on a Stromberg-Carlson 4020 grid for the three period-bands of each event. Figure 4 shows these results for the explosion Faultless. The minima indicate the orientation of the best fitting right-lateral, vertical, strike-slip fault as measured clockwise from the north at the source. A comparison of the error plots over the three bands in Fig. 4 reveals the frequency dependence of F. The orientation θ of the double-couple remains essentially unchanged over the three bands while F is greatest at long periods and smallest at short periods. This relationship was observed for nearly all events and indicates that the source of Love waves is less efficient at short periods than the Rayleigh wave source. A similar phenomenon was noted by Aki et al (1969) for body waves from the Benham event. Figure 5 shows the relationship between F and period for several events.

Observed and calculated Love/Rayleigh amplitude ratios as a function of azimuth for three explosions are shown in Fig. 6. A summary of the best fitting F and θ in the 15 to 22 sec period range for each event is given in Table 1. For some explosions (Buff and the presumed Soviet events of 3-20-66, 3-26-67, and 10-21-67) for which the surface wave data was not

of sufficient quality to permit the calculation of spectral ratios, the parameters F and θ were determined from measurements of the maximum amplitudes of Love and Rayleigh waves. Included in Table 1 is the ratio of the surface wave energy of the double-couple to the energy of the explosion. This ratio (Toksöz et al 1965) is closely approximated by

$$E_{tect}/E_{exp} = 4/3\ F^2. \qquad (4)$$

Several conclusions can be drawn from Table 1. The close agreement in fault orientation of most of the events at the Nevada Test Site indicates that a regional stress field is probably controlling the strain release. The large variation within the two Soviet testing areas may be due to a lack of sufficien data in the case of three of the events. The dependence of F and hence the amount of stress release, on lithology was previously noted by Toksöz (1967) and by Toksöz & Kehrer (1971). Table 1 provides additional evidence that the multipolar source component is larger in more competent rock. Thus strain release from a particular explosion is dependent on the rock medium and the regional state of strain. It is also apparent that there are variations for a given rock type, as in the case of the three events in granite. This can be explained by the differences in ambient stress levels and available strain energy (Toksöz et al 1971). When the F value exceeds unity the

Rayleigh wave radiation pattern will show a lobate structure and reversed polarity in alternating quadrants. This has been discussed in an earlier paper (Toksöz & Kehrer 1971) and is here demonstrated in Fig. 7 for the Pile Driver and Greeley explosions.

The north-northwest orientation of the fault planes of most of the Nevada Test Site explosions is in good agreement with lineaments and dominant fault patterns in the area. Figure 8 shows the Yucca Flat portion of the Nevada Test Site with the source mechanisms of the explosions studied there. Included are the major natural faults and some of the fractures produced by the events. The chief feature of Yucca Flat is the Yucca Fault which trends northward through alluvium and is of recent age. Although most observed displacements across the Yucca Fault are vertical following nearby explosions, numerous en echelon fractures along the fault were produced in the alluvium by Corduroy (Barosch 1968). Such an en echelon pattern is generally related to strike-slip movement in the underlying basement. The trend of the pattern in this case suggests right-lateral slippage.

Figure 9 shows the Pahute Mesa portion of the Nevada Test Site with the natural faults, explosion-produced fractures, and the events studied. The main structural feature of Pahute Mesa is the Silent Canyon Caldera, which encloses the five events.

Many normal faults, striking north-northwest, cut the thick sequence of Tertiary volcanic rock. Recent natural movement along some of these faults has been inferred (McKeown et al 1966). For Benham and Boxcar, studies of aftershock distribution (Hamilton & Healy 1969; Ryall & Savage 1969) as well as studies of faulting and fracturing caused by the explosions (Buckman 1969; McKeown & Dickey 1969) have been published. Figure 10 shows the relationships of these two sets of data with the source mechanisms determined for the two events. In the case of Benham, the correlation between the orientation of the double-couple and the trend of the aftershock pattern as well as the orientation of faults and fractures is quite good. Both vertical and right-lateral movements on the nearby Boxcar fault were initiated by Benham.

The aftershocks of Benham were concentrated in two patterns (Hamilton & Healy 1969). Those to the northwest of ground zero follow a northeasterly trend while those to the west and southwest trend north-south. Fault plane solutions from P waves of events in the first group indicate dip-slip fault movement. Solutions for the second group indicate right-lateral strike-slip motion in a northerly direction. These two patterns were further confirmed in a study of smaller Benham aftershocks (Stauder 1971). The solutions for the second group of aftershocks are similar to the orientation of the double-couple component for Benham (and other events) as determined by this study.

The Benham and Boxcar aftershocks when considered together (see Fig. 10) indicate the continuity of the distribution pattern. Northeast-trending Benham aftershocks overlap with those of Boxcar.

II. EFFECT OF TECTONIC STRAIN RELEASE ON MAGNITUDES AND DISCRIMINANTS

With explosions such as Pile Driver, Hardhat and Greeley where the surface wave energy due to strain release is greater than that of the explosion, one might expect the M_S values to increase. The expected theoretical increase ΔM_S determined from the Gutenberg-Richter energy-magnitude relationship for different F values is listed in Table 2. These were computed using

$$\Delta M_S = \frac{1}{1.5} \log \left(1 + E_{tect}/E_{exp}\right) \qquad (5)$$

For explosions such as Pile Driver and Greeley (with F values of 3.2 and 1.6, respectively) one would expect surface wave magnitudes to be greater than those of corresponding explosions with small F values. One way of investigating this point is to look at M_S vs m_b values for a series of explosions with different F values. In Fig. 11, $M_S - m_b$ explosion data

from three different authors are plotted. Neither Pile Driver nor Greeley is distinguishable from the general explosion populations. The reason for this seems to be that Rayleigh waves due to the explosion component and double-couple component of the source reinforce and cancel out in alternate azimuthal quadrants. Thus when azimuthally averaged, the net effect on magnitudes is small.

To illustrate this point let us compare the Pile Driver radiation pattern and azimuthal range of the Canadian network stations used by Basham (1969) in his magnitude determinations in Fig. 12. With our source model, Canadian stations can be expected to record, on the average, normal Rayleigh wave amplitudes and thus yield a normal M_S vs m_b value, as is indeed observed.

Thus to insure a representative magnitude, it is important to use data from several azimuths. Furthermore, while establishing station corrections for magnitude determinations, it is important to use data from explosions with low F values or from those at different sites.

III. SOURCE-TIME FUNCTION

All observations that have been made on the spectra of surface waves from explosions and earthquakes of comparable

magnitudes indicate that earthquake spectra are richer in long-period components compared to explosions. This could be due to a) source depth, b) source volume and c) source-time function.

Tsai & Aki (1971) favor the source-depth effect to explain the differences in spectra while assuming the source function for explosions and earthquakes to be the same (step function). The spectra of deeper earthquakes would be shifted toward lower frequencies. This effect cannot be neglected but it does not explain two sets of data: 1) Some aftershocks of the Benham and Jorum events were accurately located. While focal depths were less than 5 km (some as shallow as 3.5 km) their spectral characteristics were similar to those of earthquakes rather than explosions (Molnar et al 1969; Savino et al 1971). Also, spectra of collapse events are shifted toward lower frequencies relative to explosions. 2) Spectra of Love waves generated by the explosions are similar to those generated by earthquakes (Savino et al 1971; Toksöz et al 1971). In fact the Love wave source-time function determined from amplitude equalization is close to a step function.

For an explosion, a decaying source-pressure function, with or without a residual d-c pressure, could explain the observed spectra. In our earlier studies (Toksöz et al 1969) we adopted a pressure function given by

$$p(t) = p_o t e^{-\eta t} \qquad (6)$$

where p_o is a constant and η is a time constant dependent on yield in a given medium. For Bilby, $\eta = 1.5$ sec^{-1} fits the observed spectra at three stations as is shown in Fig. 13. Discrepancies at periods longer than $T = 30$ sec are attributed to the effects of lateral heterogeneities and low signal-to-noise ratio.

In a given medium, the source pulse becomes broader with increasing yield. This could be explained by the larger non-linear zone and hence greater attenuation of higher frequencies in this zone (Andrews & Shlien 1972). Observed ground displacement spectra of Rayleigh waves from several NTS explosions as recorded at LASA is shown in Fig. 14 along with three theoretical spectra for two source types. Curve 1 is based on a step function pressure variation. Curves 2 and 3 are based on the decaying pressure pulse with $\eta = 1$ and $\eta = 0.6$ sec^{-1}, respectively. It is clear that for the five lower explosions with intermediate yields, the decaying source function with $\eta = 1.0$ fits the spectra, while for the three larger events, $\eta < 1$ is necessary. The specra of the step function and the decaying pulse [Eq. (6)] type source functions are given by:

$$|S(\omega)| = \frac{1}{\omega} T/2\pi \qquad \text{step}$$

$$|S(\omega)| = \frac{1}{\eta^2 + \omega^2} = \frac{1}{\eta^2 + \frac{4\pi^2}{T^2}} \qquad \text{decaying pulse} \tag{7}$$

where ω is the angular frequency and T is the period. At very low frequencies, the spectrum of the decaying pulse approaches a constant, while that of the step increases with increasing period. At higher frequencies the pulse spectrum falls off proportionally to ω^{-2}, while the step falls off as $1/\omega$.

The success of the spectral ratio discriminant (ratio of amplitude at $T = 20$ sec to $T = 40$-60 sec) can also be explained by the difference in source-time functions of the explosions and earthquakes as given in Eq. (7).

CONCLUSIONS

Nuclear explosions detonated in media with tectonic stresses interact with the ambient stress field and release some of the strain energy. This phenomenon complicates the Rayleigh wave radiation patterns and generates Love waves. It could also affect the $M_S - m_b$ discriminants. Some conclusions that can be derived from this study are:

1. The strain energy release from a particular explosion is dependent on the rock type and the state of stress in the medium. Generally, explosions in harder rocks release greater amounts of strain energy. This probably is related to the energy-storing capability of these rocks. No significant Love waves have been observed from explosions in loose alluvium or salt domes.

2. In a given rock type tectonic strain energy release varies. As was shown by laboratory experiments (Toksöz el al 1971), this is related to the ambient stress level.

3. The strength of the tectonic component of surface waves relative to the explosion itself increases with period.

4. Tectonic strain energy released as surface waves is generally less than the surface wave energy due to the explosion alone. In three cases (Pile Driver, Hardhat, and Greeley) the tectonic component of the surface waves exceeded those due to the explosion and, therefore, dominated the radiation pattern.

5. The tectonic strain release characteristics of explosions did not have significant effect on the $M_S - m_b$ discriminant. This may be due to two factors: a) The mean Rayleigh wave amplitude when averaged over all azimuths, does not change as a result of the tectonic strain release component. Explosion and tectonic components of the source interfere constructively and destructively in alternating quadrants. b) Generally, for an explosion of given yield, the body wave amplitudes are larger when the source is in harder media. Azimuthal averaging is most important for M_S in $M_S - m_b$ discrimination.

6. A decaying pulse-type source-time function can explain surface wave amplitude spectra and long-period/short-period spectral ratio. The shape of the pulse depends on medium properties and size of the explosion.

ACKNOWLEDGMENTS

We thank Dr. J. Filson for the LASA data and spectra. This research was supported by the Air Force Cambridge Research Laboratory under Contract No. F19628-72-C-0094 and by the Air Force Office of Scientific Research under Contract No. F44620-71-C-0049.

REFERENCES

1. Aki, K., 1964. A note on surface waves from the Hardhat nuclear explosion, J. geophys. Res., 69, 1131-1134.

2. Aki, K., Reasenberg, P., DeFazio, T., & Tsai, Y., 1969. Near-field and far-field seismic evidence for triggering of an earthquake by the Benham explosion, Bull, Seis. Soc. Am., 59, 2197-2209.

3. Andrews, D.J. & Shlien, S., 1972. Propagation of underground explosion waves in the nearly-elastic range, EOS Transaction, Am. Geophys. Union, 53, abstract p. 451.

4. Archambeau, C.B., 1968. General theory of elastrodynamic source fields, Rev. geophys., 6, 241-288.

5. Archambeau, C.B. & Sammis, C., 1970. Seismic radiation from explosions in prestressed media and the measurement of tectonic stress in the earth, Rev. geophysics., 8, 473-499.

6. Barosch, P.J., 1968. Relationship of explosion-produced fracture patterns to geologic structure in Yucca Flats Nevada Test Site, in Nevada Test Site, ed. E.B. Eckel, Geol. Soc. Am. Memoir, 110, 199-217.

7. Basham, P.W., 1969. Canadian magnitude of earthquakes and nuclear explosions in south-western North America, geophysical J.R. astr. Soc., 17, 1-13.

8. Brune, J.N. & Pomeroy, P.W., 1963. Surface wave radiation patterns for underground nuclear explosions and small-magnitude earthquakes, J. geophys. Res., 68, 5005-5028.

9. Bucknam, R.C., 1969. Geologic effects of the Benham underground nuclear explosion, Nevada Test Site, Bull. Seism. Soc. Am., 59, 2209-2220.

10. Dickey, D.D., 1968. Fault displacement as a result of underground nuclear explosions, in Nevada Test Site, ed. E.B. Eckel, Geol. Soc. Am. Memoir. 110, 219-232.

11. Dickey, D.D., 1969. Strain associated with the Benham underground nuclear explosion, Bull. Seism. Soc. Am., 59, 2221-2230.

12. Dickey, D.D., 1971. Strain accompanying the Jorum underground nuclear explosion and its relation to geology, Bull. Seism. Soc. Am., 61, 1571-1581.

13. Fernald, A.T., Corchary, C.S., & Williams, W.P., 1968. Surficial geologic map of Yucca Flat, Nye and Lincoln Counties, Nevada, U.S. Geol. Survey Misc. Geol. Inv. Map I-550.

14. Hamilton, R.M., & Healy, J.H., 1969. Aftershocks of the Benham nuclear explosion, Bull. Seism. Soc. Am., 59, 2271-2281.

15. Harkrider, D.G., 1964. Surface waves in multilayered elastic media, 1. Rayleigh and Love waves from buried sources in a multilayered elastic half-space, Bull. Seism. Soc. Am., 54, 627-680.

16. Kehrer, H.H., 1969. Radiation patterns of seismic surface waves from nuclear explosions, M.S. Thesis, Massachusetts Institute of Technology, Cambridge, Massachusetts.

17. Lande, L. & Filson, J., 1971. Scaled Rayleigh wave spectra from explosions, Semiannual Tech. Summary-Seismic Discrimination, M.I.T. Lincoln Laboratory, 1-3, 8-11.

18. Leavy, D., 1971. Scattering of elastic waves around a compressional source, M.S. Thesis, Massachusetts Institute of Technology, Cambridge, Massachusetts.

19. Liebermann, R.C. & Pomeroy, P.W., 1969. Relative excitation of surface waves by earthquakes and underground explosions, J. geophys. Res., 74, 1575-1590.

20. McKeown, F.A. & Dickey, D.D., 1969. Fault displacements and motion related to nuclear explosions, Bull. Seism. Soc. Am., 59, 2253-2269.

21. McKeown, F.A., Orkild, P.P., Dickey, D.D. & Snyder, R.P., 1966. Some geologic data pertinent to the seismic characteristics of Pahute Mesa, USGS Tech.-letter: Sp. Std. I-45.

22. Molnar, P., Jacob, K., & Sykes, L.R., 1969. Microearthquake activity in eastern Nevada and Death Valley, California before and after the nuclear explosion Benham, Bull. Seism. Soc. Am., 59, 2177-2184.

23. Orkild, P.P., Sargent, K.A., & Snyder, R.P., 1969. Geologic map of Pahute Mesa, Nevada Test Site, Nye County, Nevada, U.S. Geol. Survey Misc. Geol. Inv. Map I-567.

24. Press, F., & Archambeau, C.B., 1962. Release of tectonic strain by underground nuclear explosions, J. geophys. Res., 67, 337-343.

25. Ryall, A. & Savage, W.U., 1969. A comparison of seismological effects for the Nevada underground test Boxcar with natural earthquakes in the Nevada region, J. geophys. Res., 74, 4281-4289.

26. Savino, J., Sykes, L. R., Leibermann, R.C., & Molnar, P., 1971. Excitation of seismic surface waves with periods of 15 to 70 seconds for earthquakes and underground explosions. J. geophys. Res., 76, 8003-8020.

27. Stauder, W., 1971. Smaller aftershocks of the Benham nuclear explosion, Bull, Seism. Soc. Am., 61, 417-428.

28. Toksöz, M.N., 1967. Radiation of seismic surface waves from underground explosions, Proceedings of the Vesiac Conference on the current status and future prognosis of shallow seismic events, VESIAC Rept., Willow Run Laboratories, The University of Michigan, 65-84.

29. Toksöz, M.N., Ben-Menahem, A., & Harkrider, D.G., 1964. Determination of source parameters by amplitude equalization of seismic surface waves, 1. Underground nuclear explosions, J. geophys. Res., 69, 4355-4366.

30. Toksöz, M.N., Harkrider, D. G., & Ben-Menahem, A., 1965. Determination of source parameters by amplitude euqalization of seismic surface waves. 2. Release of tectonic strain by underground nuclear explosions and mechanisms of earthquakes, J. geophys. Res., 70, 907-922.

31. Toksöz, M.N. & Kehrer, H.H., 1971. Underground nuclear explosions: tectonic utility and dangers, Science, 173, 230-233.

32. Toksöz, M.N., Thomson, K.C., & Ahrens, T.J., 1971. Generation of seismic waves by explosions in prestressed media, Bull. Seism. Soc. Am., 61, 1589-1623.

33. Tsai, Y. & Aki, K., 1971. Amplitude spectra of surface waves from small earthquakes and underground nuclear explosions, J. geophys. Res., 76, 3940-3952.

34. Wagner, D.E., 1970. Nuclear yields from Rayleigh waves, Earthquake Notes, 41, 9-20.

TABLE 1.

TECTONIC STRAIN RELEASE CHARACTERISTICS OF UNDERGROUND NUCLEAR EXPLOSIONS

U. S. Explosions

EVENT		REGION	MEDIUM	D.C. STRENGTH (F)	FAULT AZI.	ENERGY RATIO E_{tect}/E_{exp}
Pile Driver	6-2-66	Yucca Flat (n. end)	Granite	3.20	340°	13.65
Hardhat	2-15-62	Yucca Flat (n. end)	Granite	3.00	330°	12.00
Shoal	10-26-63	Fallon, Nevada	Granite	.90	346°	1.05
Greeley	12-20-66	Pahute Mesa	Zeolite Tuff	1.60	355°	3.41
Benham	12-19-68	Pahute Mesa	Zeolite Tuff	.85	345°	.96
Chartreuse	5-6-66	Pahute Mesa	Rhyolite	.90	353°	1.05
Duryea	4-14-66	Pahute Mesa	Rhyolite	.75	355°	.75
Half Beak	6-30-66	Pahute Mesa	Rhyolite	.67	345°	.60
Boxcar	4-26-68	Pahute Mesa	Rhyolite	.59	346°	.46
Corduroy	12-3-65	Yucca Flat	Quartzite	.72	347°	.69
Rulison	9-10-69	Grand Valley, Colorado	Ss. and Shale	.60	335°	.48
Faultless	1-19-68	Central Nevada	Sat. Tuff	.50	344°	.33
Cup	3-26-65	Yucca Flat	Tuff	.55	200°	.40
Bilby	9-13-63	Yucca Flat	Tuff	.47	340°	.29
Tan	6-3-66	Yucca Flat	Tuff	.39	347°	.20
Bronze	7-23-65	Yucca Flat	Tuff	.33	185°	.15
Buff	12-16-65	Yucca Flat	Tuff	.31	208°	.13
Haymaker	6-27-62	Yucca Flat	Alluvium	.33	340°	.14
Sedan	7-6-62	Yucca Flat	Alluvium	0	-	0
Salmon	10-22-64	Hattiesburg, Mississippi	Salt	0	-	0
Gnome	12-10-61	Carlsbad, New Mexico	Salt	0	-	0
Milrow	10-2-69	Amchitka	Andesite	<.6	-	<.48
Cannikin	11-5-71	Amchitka	Andesite	.36	-	.17

TABLE 1. Continued

Presumed Soviet Explosions

EVENT	DATE (m-d-y)	REGION	MEDIUM	D.C. STRENGTH (F)	FAULT AZI.	ENERGY RATIO E_{tect}/E_{exp}
U.S.S.R.	10-27-66	Novaya Zemlya	--	0.90	5°	1.05
U.S.S.R.	10-21-67	Novaya Zemlya	--	0.71	43°	0.67
U.S.S.R.	2-26-67	E. Kazakh	--	0.85	6°	0.96
U.S.S.R.	3-20-67	E. Kazakh	--	0.81	155°	0.87
U.S.S.R.	2-13-66	E. Kazakh	--	0.67	101°	0.60

TABLE 2

EFFECT OF TECTONIC STRAIN RELEASE ON MAGNITUDES

F Double-Couple Part	E_{tect}/E_{exp}	ΔM_S Maximum increase in magnitude due to tectonic component
0.3	0.12	0.07
0.5	0.33	0.08
0.7	0.65	0.14
1.0	1.33	0.24
1.5	3.00	0.40
2.0	5.33	0.53
3.0	12.00	1.08
4.0	21.33	1.23

Figure Captions

Figure 1. Long-period filtered seismograms from the Pile Driver, Tan, and Greeley explosions recorded at Weston, Massachusetts.

Figure 2. Stations recording surface waves from explosions in the continental United states.

Figure 3. Filtered (upper three traces) and unfiltered (lower three traces) long-period components from the Boxcar explosion at Mould Bay, Canada (MBC) plotted from digital data at the same gain. The two filtered horizontal components have been rotated to radial and tangential directions to separate Love and Rayleigh waves.

Figure 4. Contour plots of the deviations of combinations of part double-couple and fault plane azimuth from experimental Love to Rayleigh wave ratios for three period ranges: a) 9 to 15 sec., b) 15 to 22 sec., and c) 22 to 30 sec., for the Faultless event.

Figure 5. The period dependence of F, the part double-couple, for five nuclear explosions.

Figure 6. Observed and theoretical Love/Rayleigh wave amplitude radiation patterns for three explosions with different proportions of strain release (F).

Figure 7. Rayleigh wave radiation patterns for explosive component (circles), strain release component (broken curves), and composite sources representing the theoretical models (solid curves, where for Pile Driver: F = 3.2 and Θ = 340°; and for Greeley: F = 1.6 and Θ = 355°). The polarity (phase) of Rayleigh waves in different quadrants of the radiation pattern is indicated by (+) and (-). For Pile Driver some sample seismograms from four stations are compared to those of Tan. Amplitude factors are arbitrary. Pile Driver traces are below those of Tan. Dashed line traces have their polarities reversed. Note the perfect match of wave shapes, with polarities reversed at JP-AT and BOZ as predicted by the model. For Greeley sample seismograms are compared to those of Half Beak (COL and OXF) and Boxcar (LASA). The lower traces are from Greeley. Polarity reversal is very clear at LASA. MN-NV, Mina, Nev.;JP-AT, Jasper, Alta.; BOZ, Bozman, Mont.; AX2AL; Alexander City, Ala.;

TUC, Tucson, Ariz.; COL, College, Alaska; LASA, Large Aperature Seismic Array, Mont.; OXF, Oxford, Miss. Data symbols: ▲ LRSM stations; Δ, LRSM stations where reversed polarity was observed; ■ WWSSN stations; ●, CSSN stations.

Figure 8. Map of Yucca Flat showing the fault plane orientation of the explosions studied, explosion-produced fractures, and major natural faults in the area (geology after Fernald et al 1968).

Figure 9. Map of Pahute Mesa showing the fault plane orientations of the explosions studied, explosion-produced fractures, and natural faults in the area (faults after Orkild et al 1969).

Figure 10. Source mechanisms determined for the Boxcar and Benham events compared to natural faults and explosion-produced fracturing, and aftershock distribution. Aftershock distribution for Benham (Hamilton & Healy 1969), is that of the larger aftershocks (magnitude 3 to 4.2). Aftershocks from Boxcar (Ryall & Savage 1969) are those occurring in the first two days after the event. The circles are of radius 5 km centered on the ground zero of the explosion.

Figure 11. $M_S - m_b$ for 13 American underground nuclear explosions from the data of Liebermann & Pomeroy (1969), Basham (1969), and Wagner (1970).

Figure 12. Rayleigh wave radiation pattern for Pile Driver with the azimuthal range of Canadian stations from the event.

Figure 13. Amplitude spectra of the source-time function for Bilby ($\eta = 1.5$ sec^{-1}) at three stations after correction for propagation effects. Circles indicate data uncorrected for attenuation; triangles indicate the data corrected taking $Q = 100$.

Figure 14. Vertical component amplitude spectra, corrected for instrument response, from eight explosions recorded at LASA. Curves 1, 2, and 3 are computed Rayleigh wave spectra (observed explosion spectra and Curves 1 and 2 from Lande & Filson 1970).

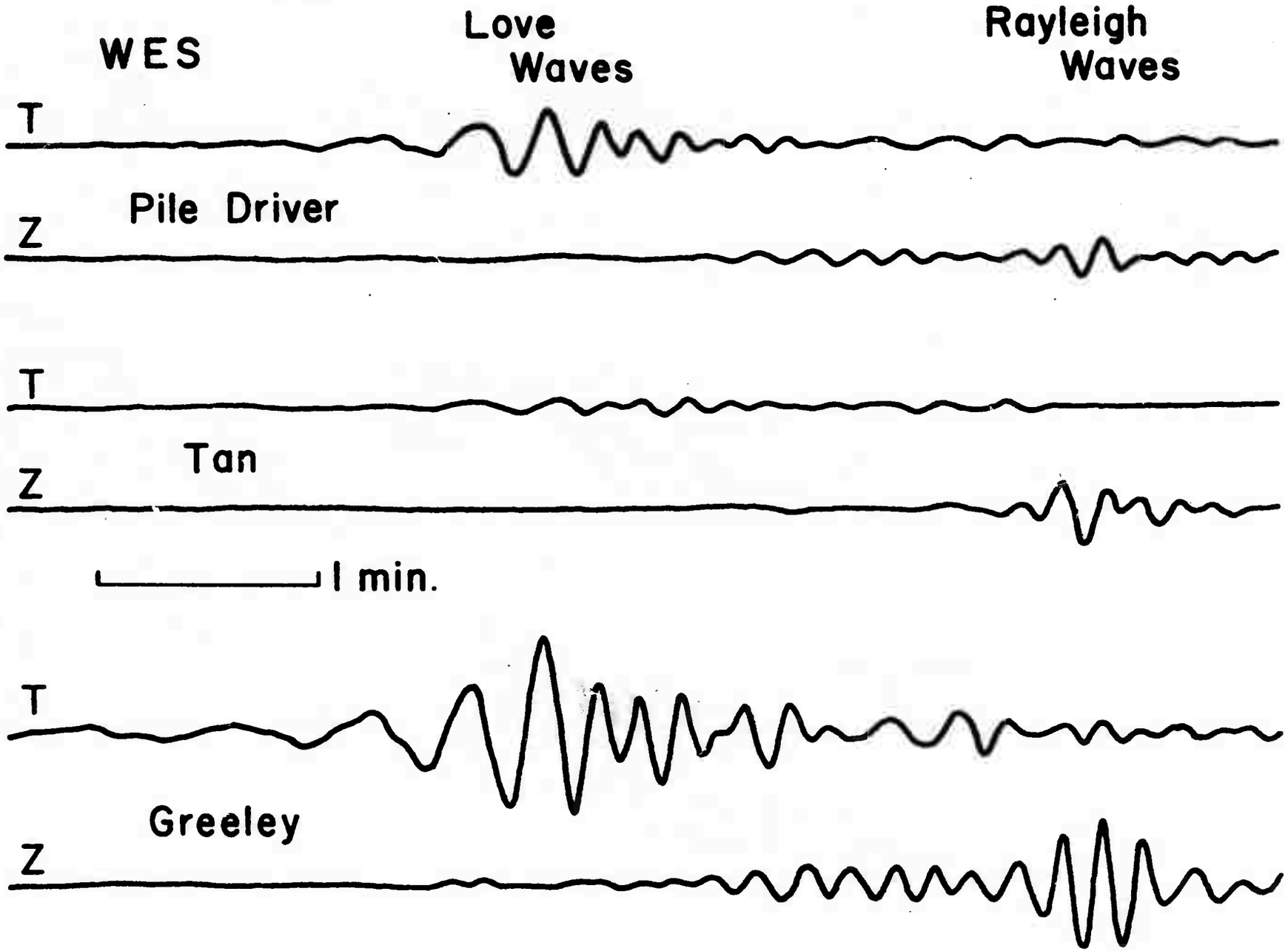
WES
Love
Waves
Rayleigh
Waves
T
Pile Driver
Z
T
Tan
Z
1 min.
T
Greeley
Z

Fig. 1

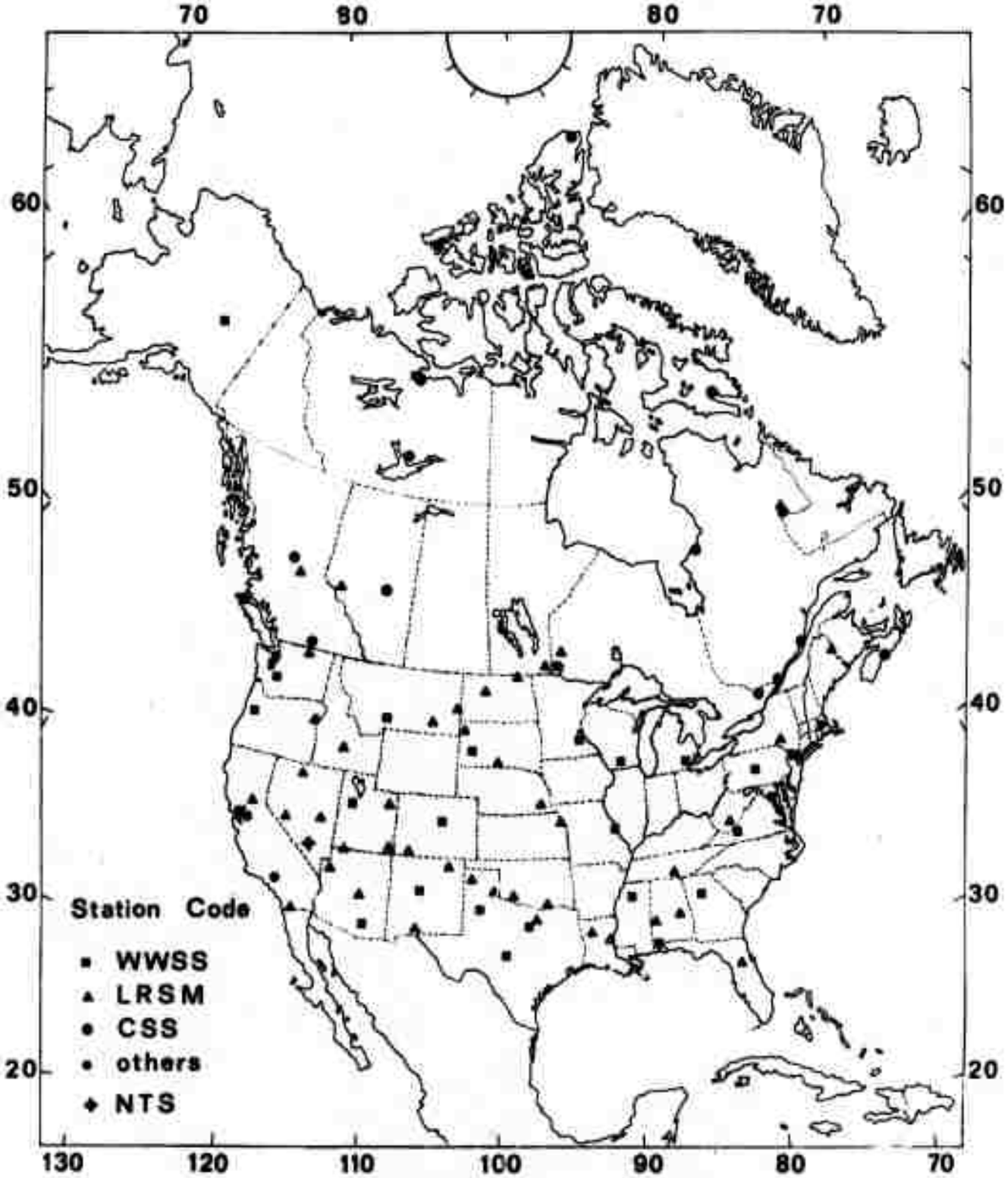
70
80
80
70
60
60
50
50
40
40
30
30
20
20
130
120
110
100
90
80
70
Station Code
WWSS
LRSM
CSS
others
NTS

Fig. 2

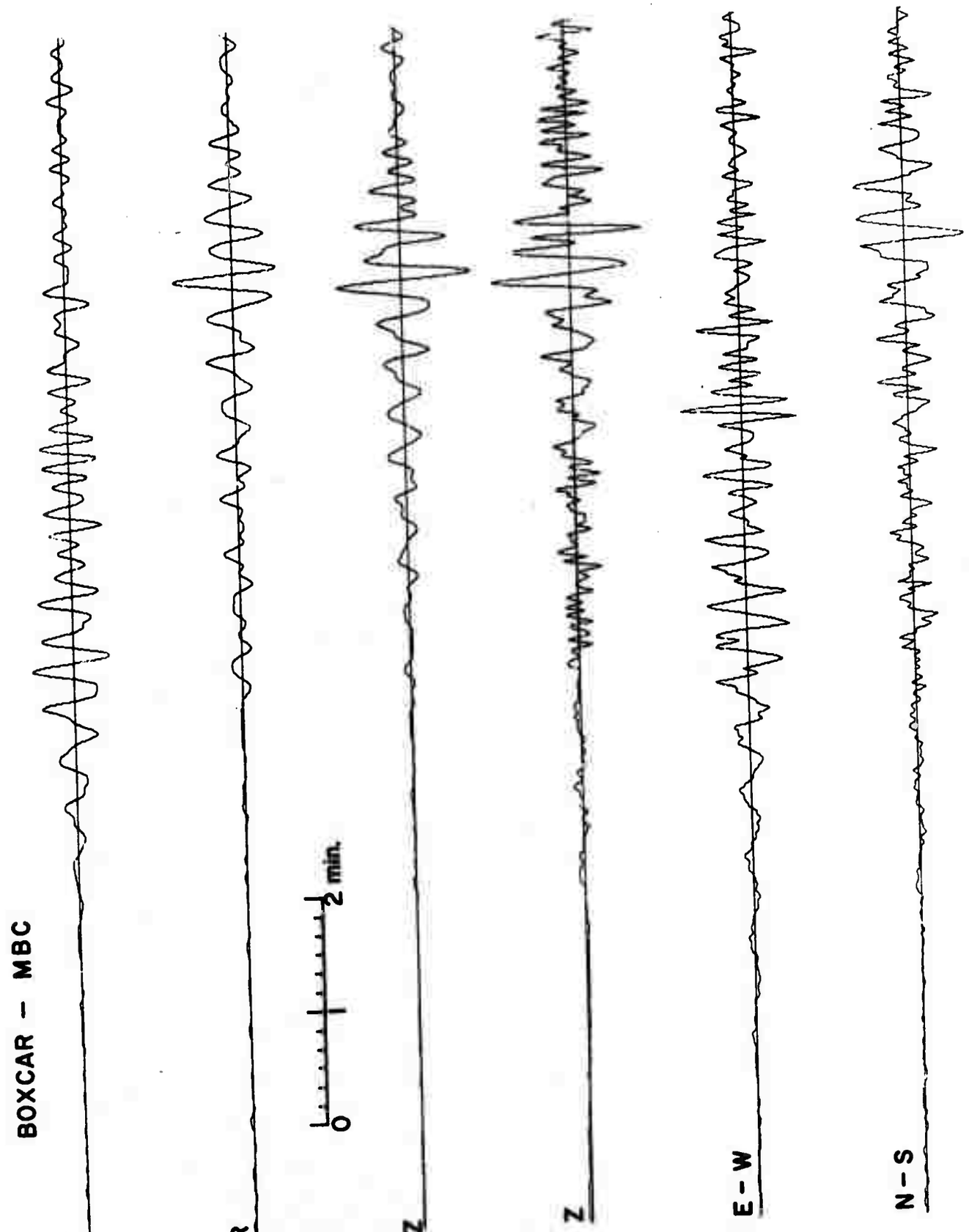

Fig. 3

Fig. 4

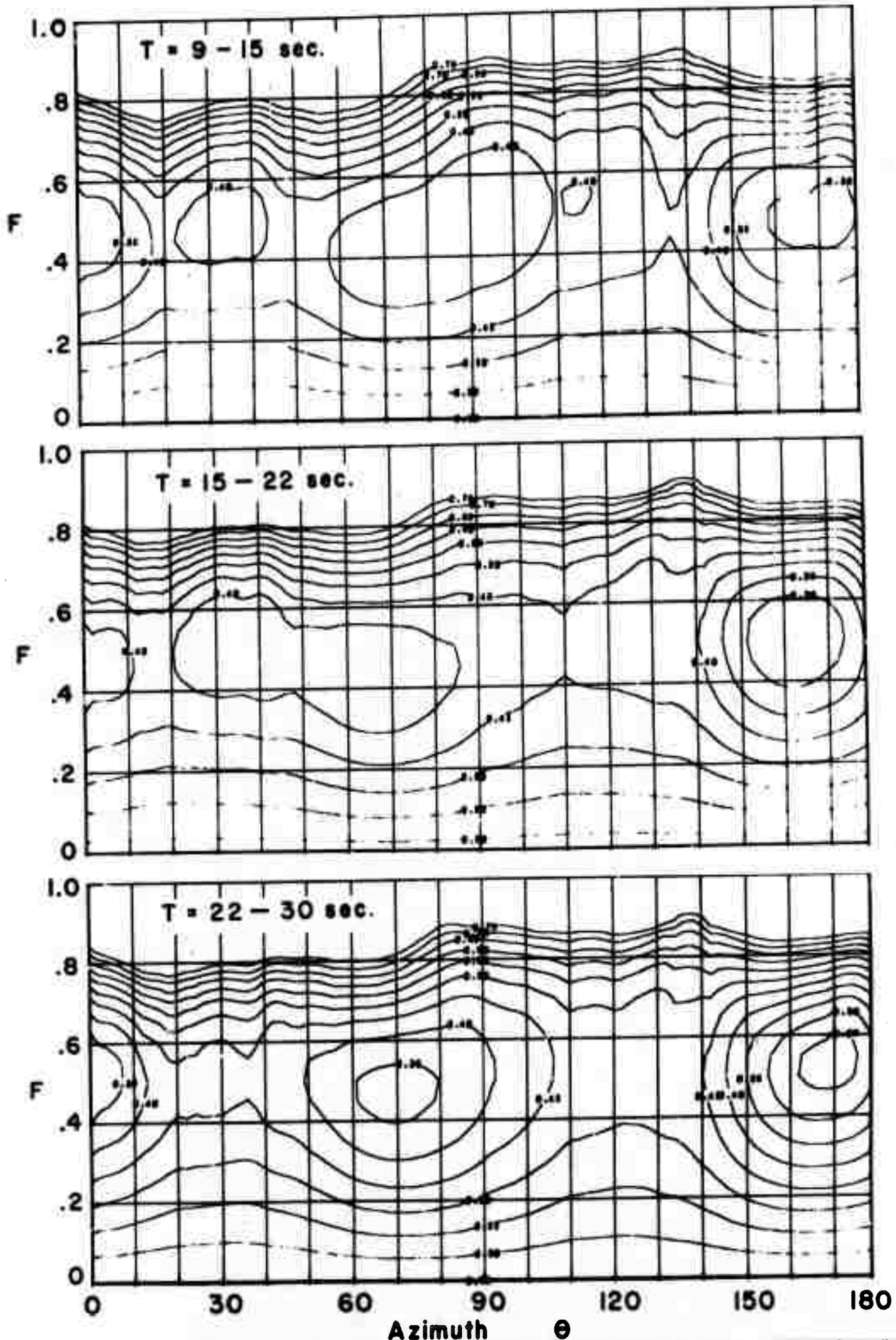
T = 9 – 15 sec.
T = 15 – 22 sec.
T = 22 – 30 sec.
F
1.0
.8
.6
.4
.2
0
0
30
60
90
120
150
180
Azimuth θ

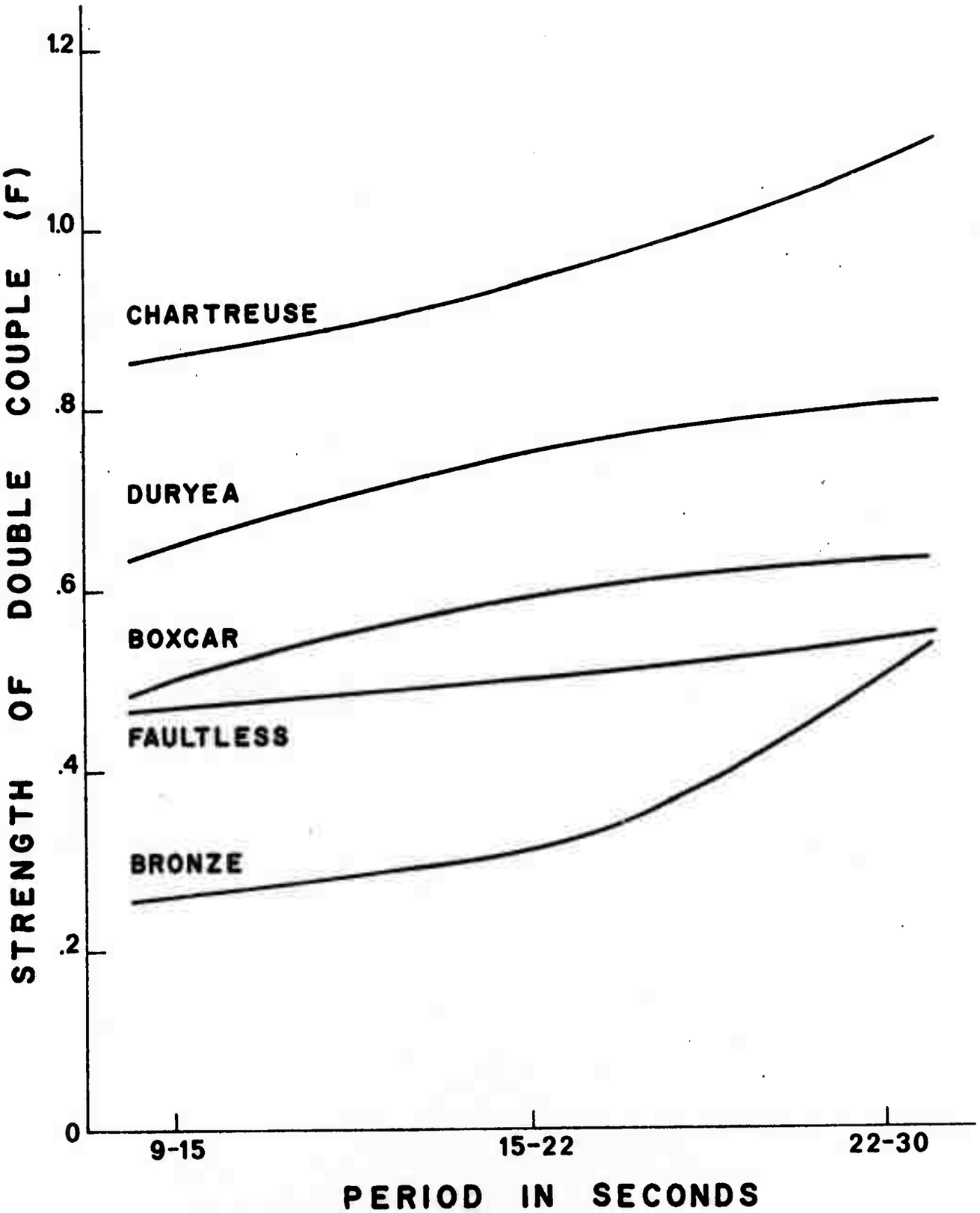
STRENGTH OF DOUBLE COUPLE (F)
1.2
1.0
.8
.6
.4
.2
0
CHARTREUSE
DURYEA
BOXCAR
FAULTLESS
BRONZE
9-15
15-22
22-30
PERIOD IN SECONDS

Fig. 5

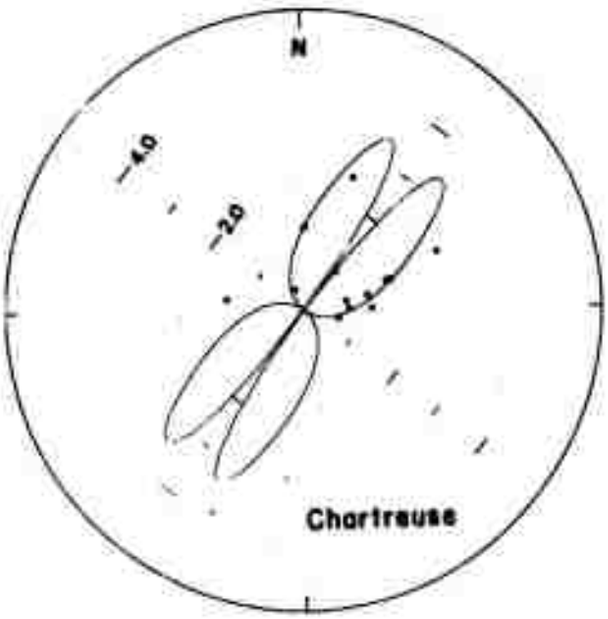

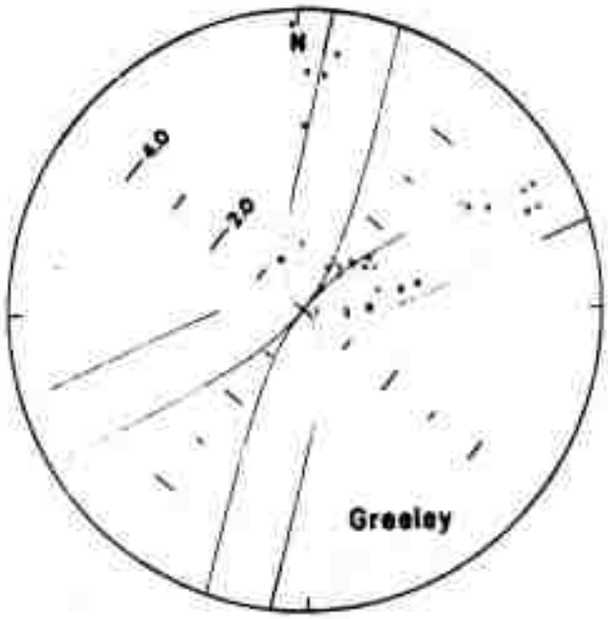

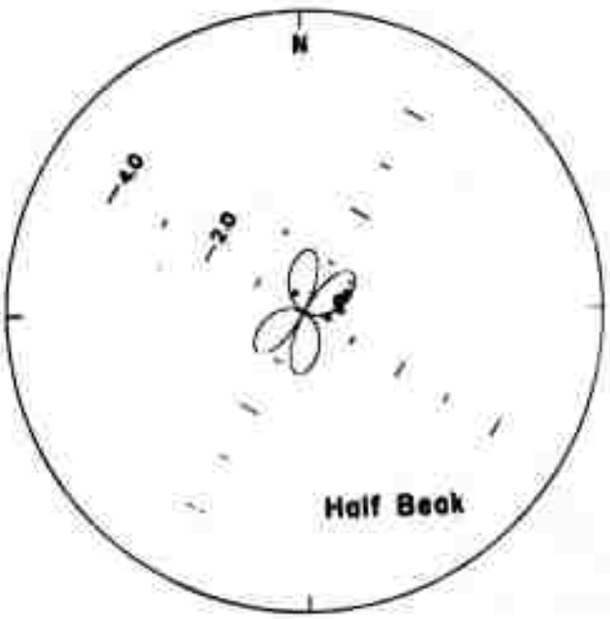

	F	θ
Greeley	1.60	355°
Chartreuse	.90	353°
Half Beak	.67	345°

x LRSM
□ WWSSN
o CSSN
* Pasadena, Cal.

Fig. 6

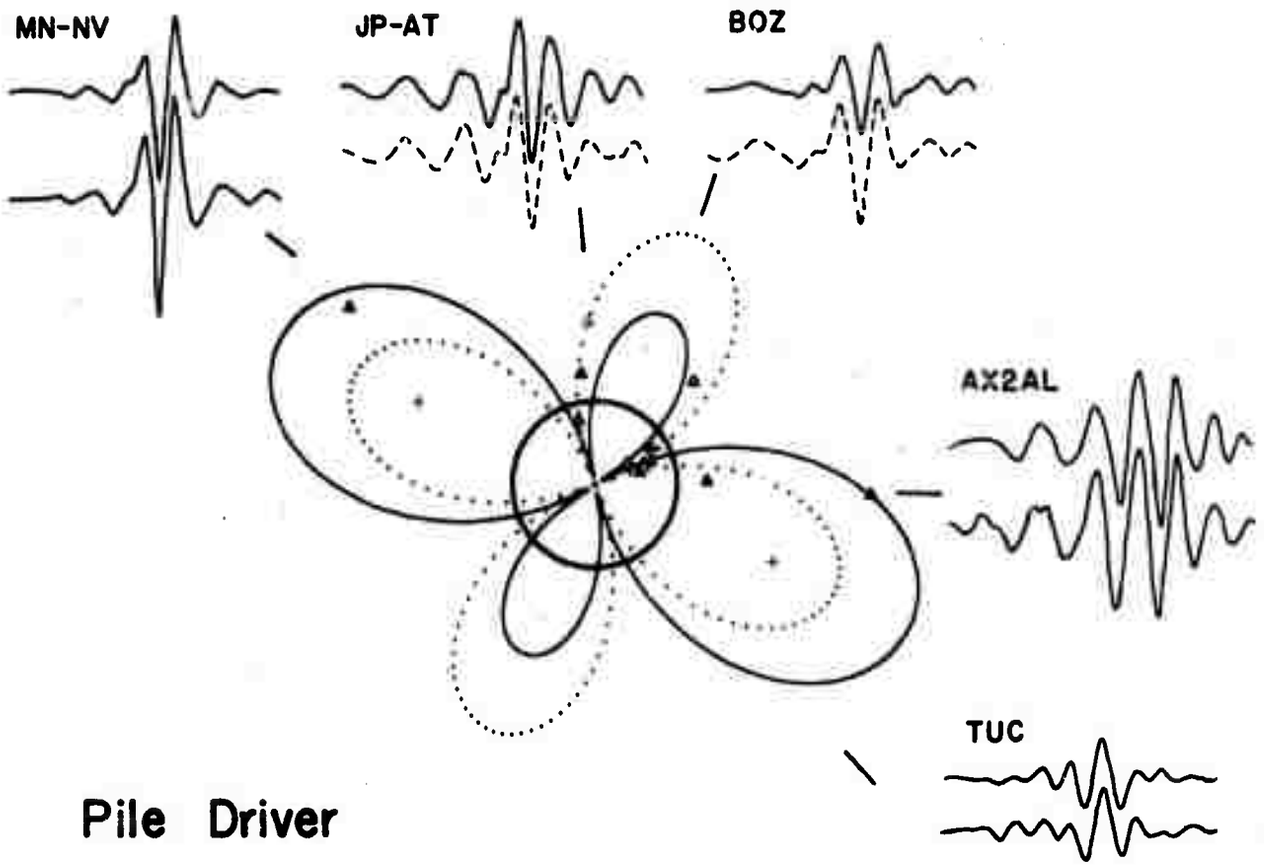

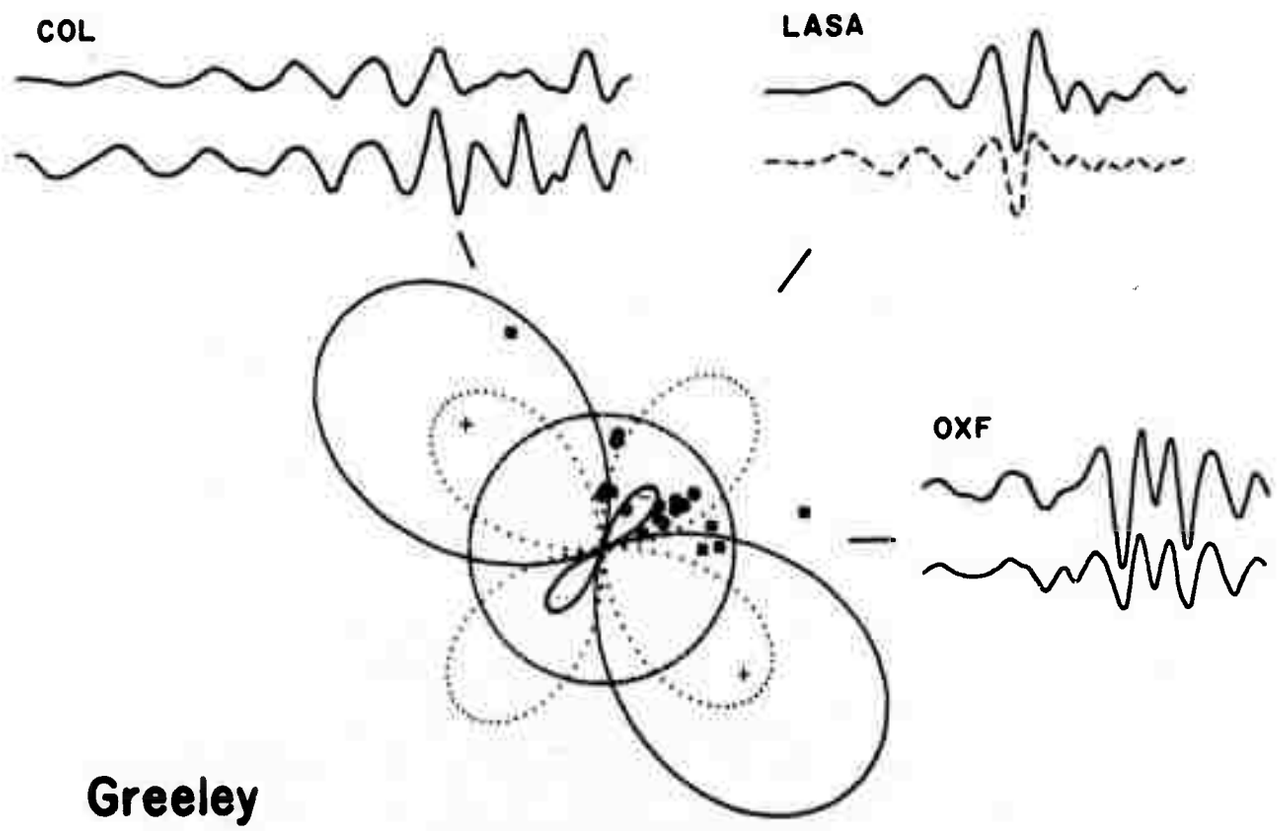

Fig. 7


PILE DRIVER
HARDHAT
CORDUROY
CUP
BRONZE
BUFF
TAN
BILBY
HAYMAKER
37°10'
116°00'
0
5 km
Volcanic rocks
Granitic rocks
Clastic rocks
Carbonate rocks
Alluvium and other surficial deposits
Natural faults
Bar on downthrown side
Explosion-produced fractures

Fig. 8

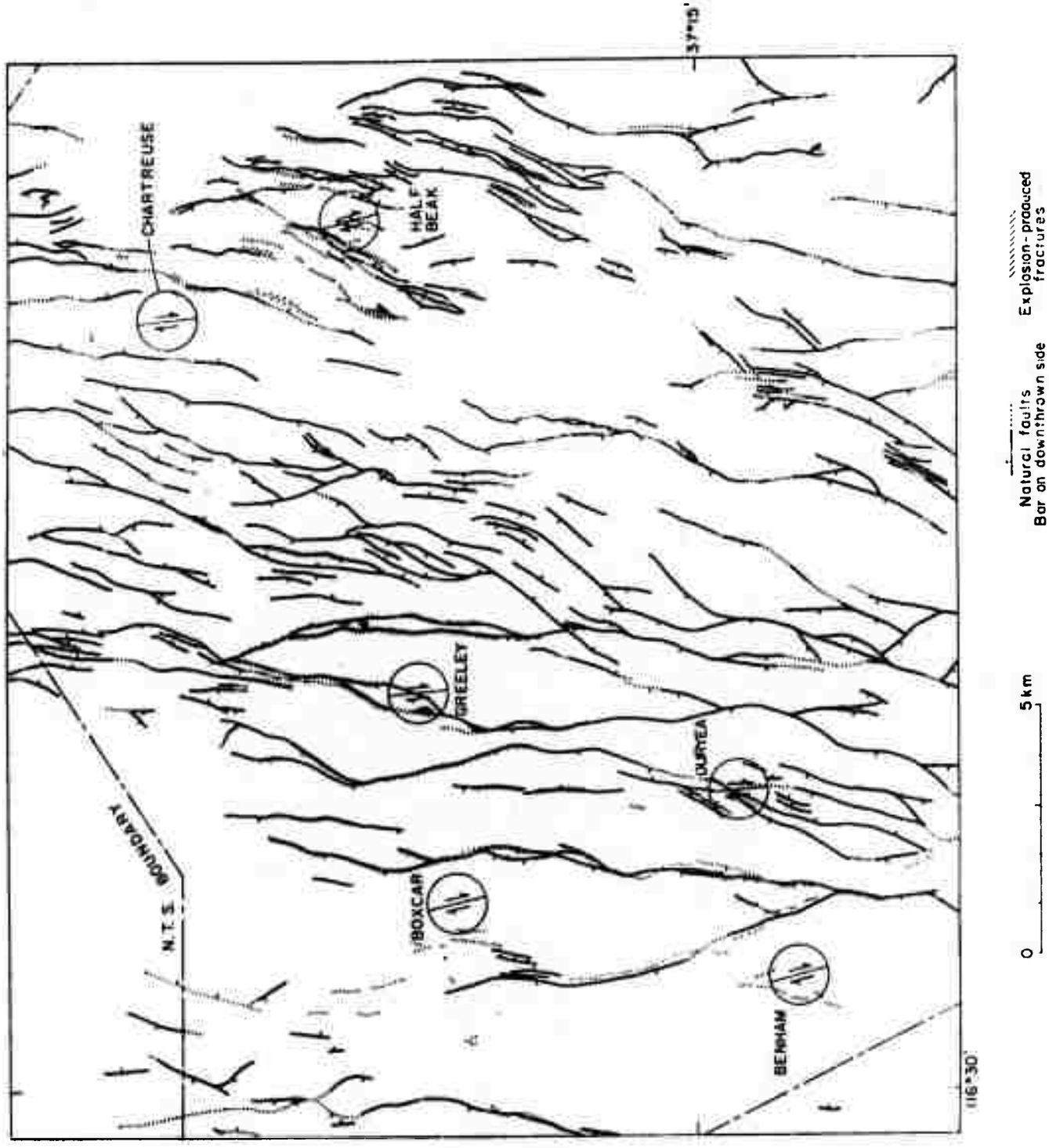
37°15'
CHARTREUSE
HALF BEAK
GREELEY
DURTEA
BOXCAR
BENHAM
N.T.S. BOUNDARY
116°30'
Natural faults
Bar on downthrown side
Explosion-produced fractures
0
5 km

Fig. 9

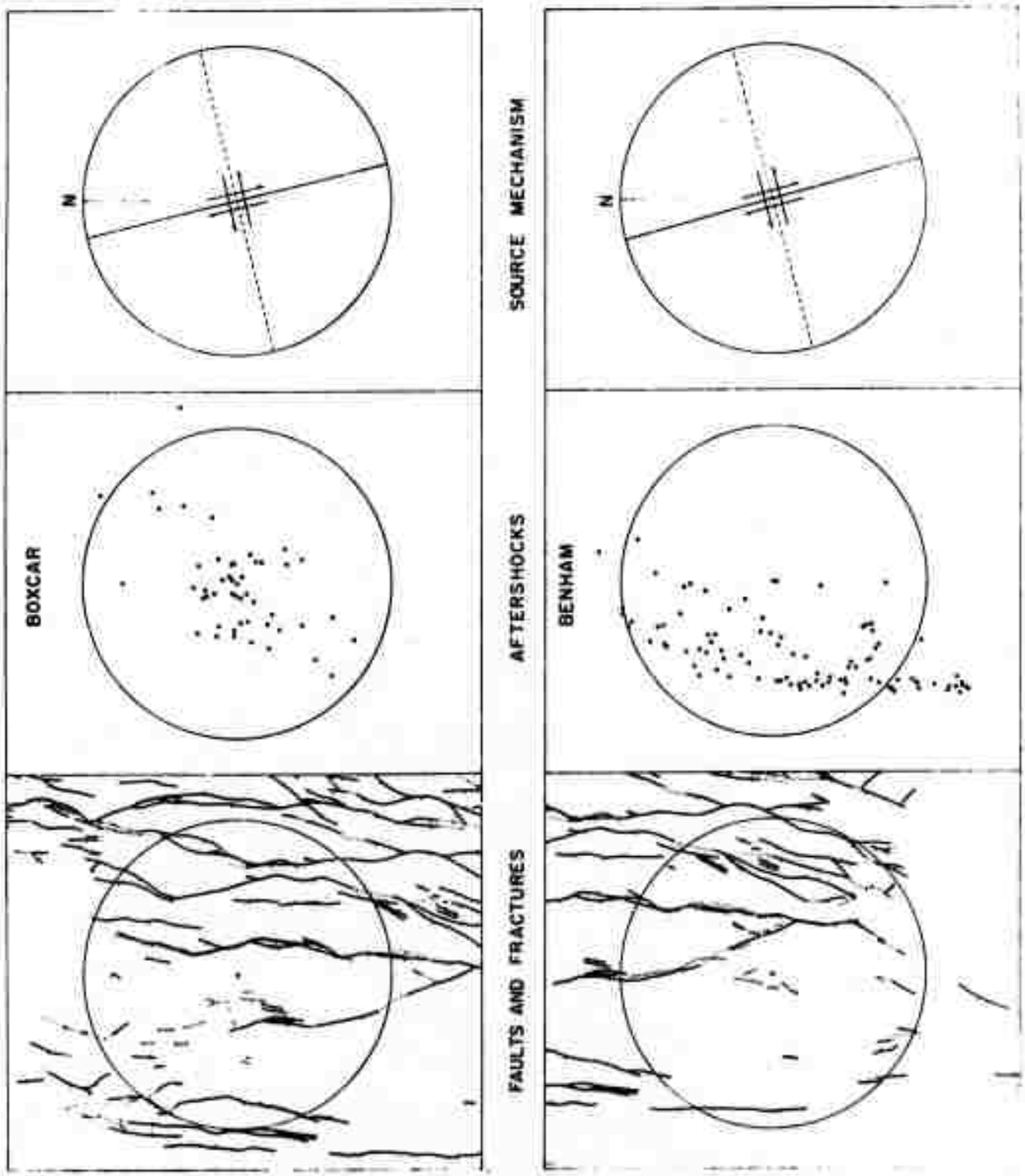
BOXCAR
BENHAM
N
N
SOURCE MECHANISM
AFTERSHOCKS
FAULTS AND FRACTURES

Fig. 10

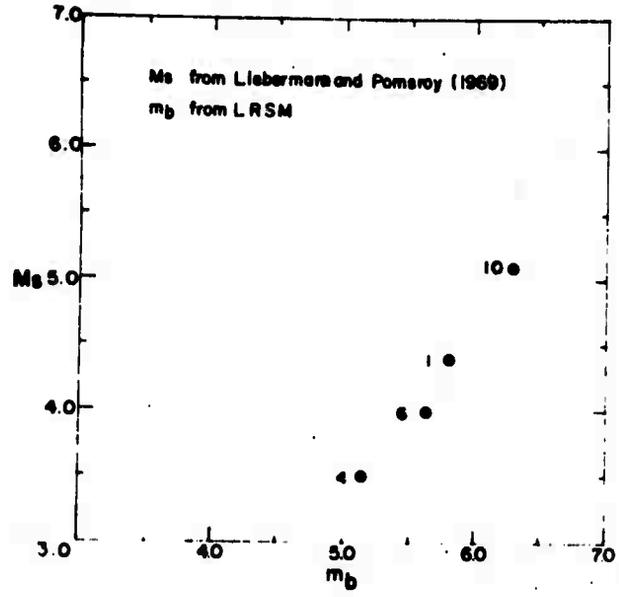

1 BILBY
2 BOXCAR
3 BRONZE
4 BUFF
5 CHARTREUSE
6 CORDUROY
7 CUP
8 DURYEA
9 FAULTLESS
10 GREELEY
11 HALFBEAK
12 PILEDRIVER
13 TAN

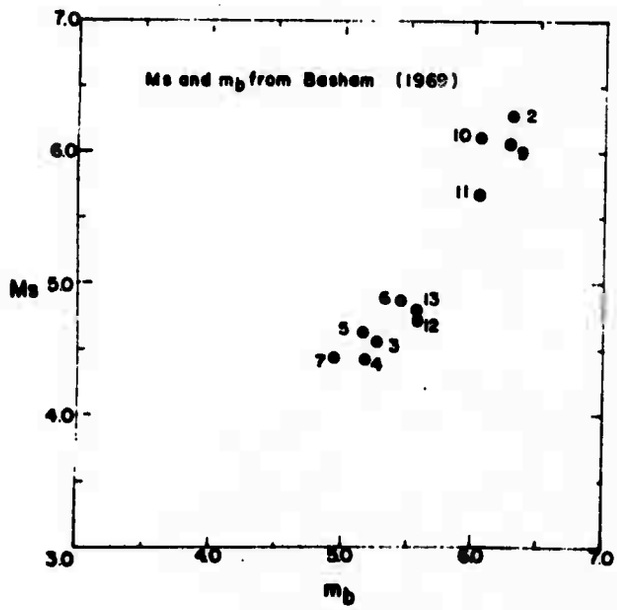

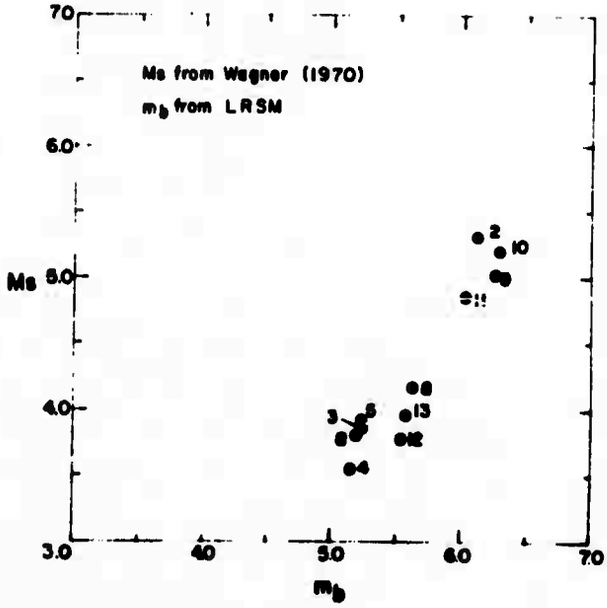

Fig. 11

Canadian Stations
Pile Driver
▲ LRSM stations with reversed polarity

Fig. 12

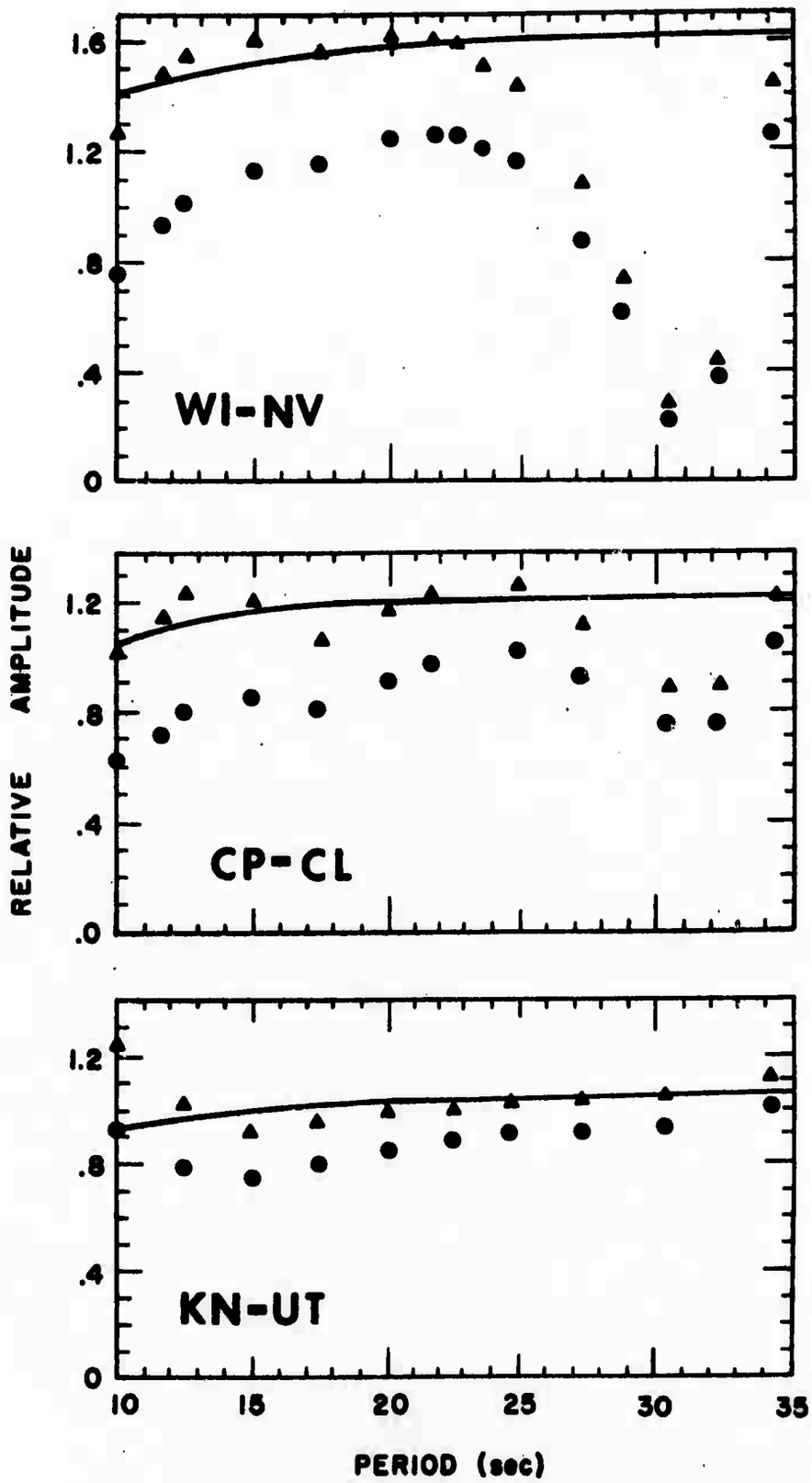
1.6
1.2
.8
.4
0
WI-NV
1.2
.8
.4
.0
CP-CL
1.2
.8
.4
0
KN-UT
RELATIVE AMPLITUDE
10
15
20
25
30
35
PERIOD (sec)

Fig. 13

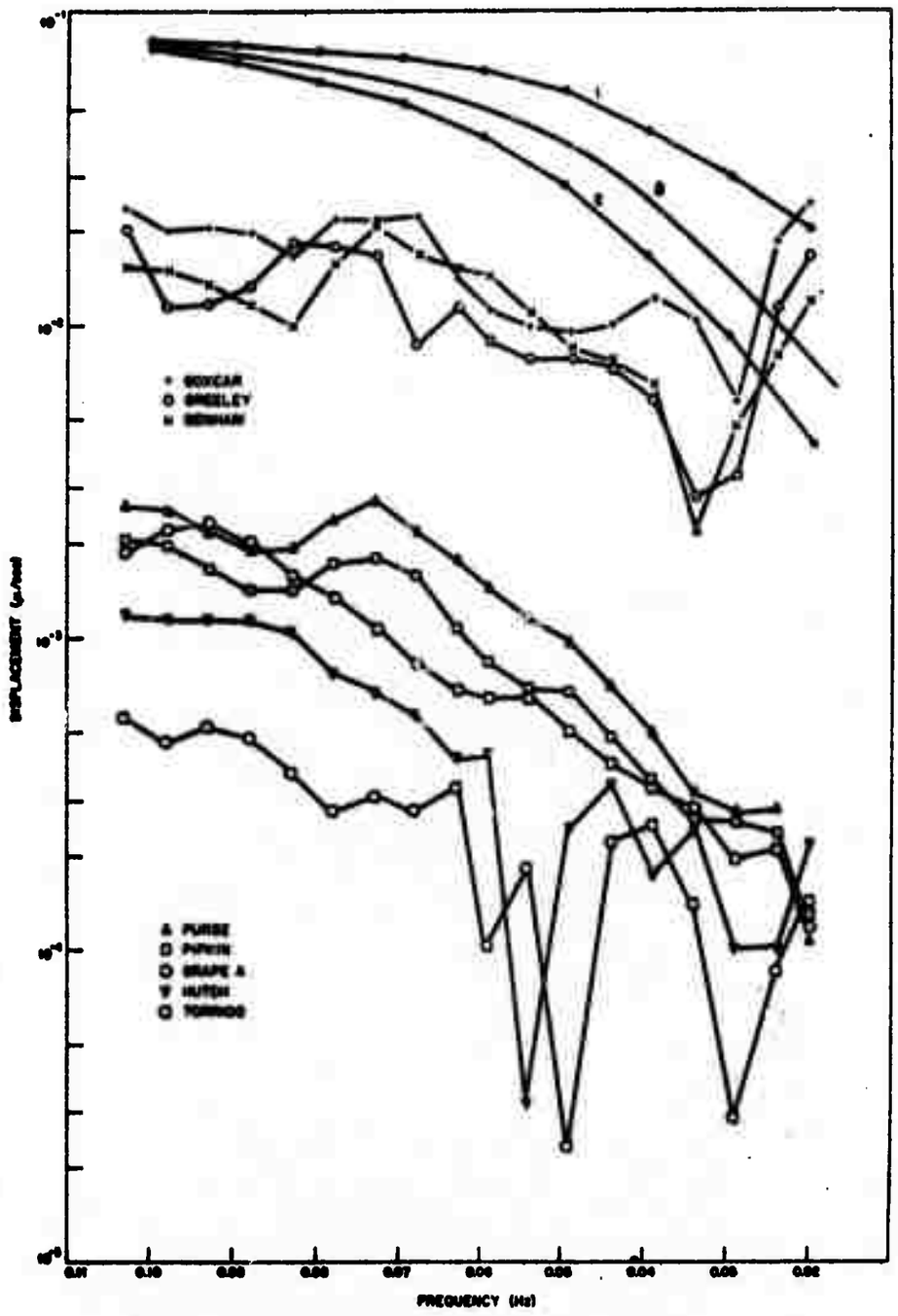
DISPLACEMENT (μ/sec)
FREQUENCY (Hz)
0.10
0.09
0.08
0.07
0.06
0.05
0.04
0.03
0.02
BOXCAR
BRESLEY
BERMAN
PURSE
PAPKIN
GRAPE A
HUTCH
TORRIDS

Fig. 14

4. EARTH STRUCTURE

4.1 Seismic-Wave Attenuation and Partial Melting in the Upper Mantle of North America by Sean C. Solomon

(Abstract)

A model of Q^{-1} based on Walsh's theory for attenuation in partially melted rock is proposed for the upper mantle of western North America. The asthenosphere (or low-Q zone), in which attenuation is attributed to a superposition of thermally activated relaxation processes, is 300 km thick in the model and must be vertically inhomogeneous. The lithosphere (or high-Q lid) is 60 km thick. The model is consistent with a wide assortment of attenuation and velocity data, in all spanning approximately three decades in frequency. Both the shear modulus and Q^{-1} for shear waves are frequency dependent in the asthenosphere. The viscosity and volume concentration of melt can be estimated from the relaxation parameters. Further, if lateral changes in these parameters, determined from the differential attenuation and travel-time delays of P and S waves, are attributed to horizontal temperature variations, then these temperature differences in the asthenosphere need be no larger than 100 to 200°K at a depth of several hundred kilometers. The highest temperatures determined in this fashion are beneath the Rocky Mountain and Pacific border regions.

4.2 On Q and Seismic Discrimination by Sean C. Solomon

Summary

The vagaries of seismic attenuation, or Q, in the earth render uncertain the estimates of many seismic source parameters made by the unwary. In particular, the discrimination of waves produced by earthquakes from those of explosions, if the waves have traveled dissimilar paths, or the characterization of a seismic source from the seismic-wave amplitude spectrum require concern for the spatial and frequency dependence of Q. Surface-wave amplitudes are most affected by attenuation at periods long enough (30 sec and greater) so that much of the energy propagates in the low-Q asthenosphere, and at periods short enough (less than 15 sec) so that near-surface structure is important. Thus the standard surface-wave magnitude is largely insensitive to anelastic losses, though for the surface-wave spectral shape to be diagnostic of source depth, such losses must be considered. The amplitudes of body waves that have penetrated the low-Q asthenosphere reflect the extreme variations of Q within that zone. Seismic discrimination criteria based on the body-wave magnitude should be restricted to comparison of events from the same tectonic province. Further, estimates of such source properties as source dimension and fractional stress drop depend critically on properly accounting for the frequency dependence of Q.

1. Introduction

The problem of discriminating shallow earthquakes from underground nuclear explosions may be visualized as an attempt to distinguish between the signals from two dissimilar, broad-band sources after those signals have passed through a complicated narrow-band filter, the earth. That the characteristics of this terrestrial filter depend upon the precise location of source and receiver adds further difficulties. A major component of the filter is seismic-wave attenuation, most conveniently represented by the quantity Q, the dimensionless quality factor. The distribution of Q in the earth determines both the absolute amplitudes of the various types of seismic waves and the shape of their amplitude spectra. In this paper, the measured properties of seismic attenuation in the earth are shown to have potentially important effects on estimates of seismic source parameters and, in particular, on some of the techniques currently used to discriminate between earthquakes and explosions.

It should perhaps be stated at the outset that the remarks below have no special bearing on the seismic discrimination problem if explosion and earthquake source are in close proximity and if signals from both are observed by the

same receiver. Only if signals that have traveled different paths or that have been recorded over different frequency bands are to be compared or contrasted does careful note need be made of corrections for attenuation and other phenomena of propagation.

2. Some Properties of Q

There are three features of the distribution of Q in the earth that are relevant to the discussion of seismic discrimination:

(1) Depth dependence. Q, considered as a material property, is a strong function of depth in the earth. Studies bohh of the attenuation of surface waves and free oscillations as a function of period (Anderson et al. 1965; Tsai & Aki 1969), and of body-wave amplitudes as a function of distance (Wadati & Hirono 1956; Archambeau et al. 1969) indicate a zone in the upper mantle within which Q is significantly lower than in the crust or the remainder of the mantle. This low-Q zone is identified with the asthenosphere in the new global tectonics (Isacks et al. 1968). Typically Q in the asthenosphere is an order of magnitude lower than in the overlying lithosphere.

(2) Lateral variation. Q is also region-dependent. The most dramatic lateral variations occur at island arcs, where the high-Q lithosphere is downthrusting into the mantle (Oliver & Isacks 1967), and at other regions where the lithosphere is abnormally thin or discontinuous (Molnar & Oliver 1969). Q also shows lateral changes within the lithosphere and asthenosphere. The most pronounced effects on seismic-wave amplitudes recorded at different stations are produced by the Q variations within the low-Q asthenosphere (Solomon & Toksöz 1970). These variations are most simply explained by relatively modest horizontal temperature gradients (Solomon 1972).

(3) Frequency dependence. At least within the asthenosphere, Q is a function of frequency. That Q may increase with frequency for short-period P waves in the mantle is suggested by the high values of Q_p (greater than 1000) determined for the frequency range 1-10 Hz (Asada & Takano 1963; Sumner 1967; Filson 1970) contrasted with values an order of magnitude lower for frequencies in the range .01 to 1 Hz (Teng 1968; Hirasawa & Takano 1966; Kanamori 1967). Further, Q approximately proportional to frequency has been observed for P and S waves over various paths and over assorted frequency bands within the frequency range .3 to 20 Hz (Frantti 1965; Kurita 1968; Fedotov & Boldyrev 1969; Archambeau et al.

1969; Mendoza 1970). The suggestion has also been made that the attenuation of surface waves and free oscillations is best fit by a frequency-dependent Q in the mantle (Tsai & Aki 1969; Jackson 1972).

The best test of the frequency dependence of Q comes from a consideration of data taken over a broad frequency band. A set of measurements of elastic and anelastic properties of the upper mantle of western U.S., in all spanning a factor of 1000 in frequency, could not all be satisfied by a Q model independent of frequency (Solomon 1972). On the other hand, a relatively simple, frequency-dependent Q model, based on the expected behaviour of attenuation in partially melted rock (Walsh 1969), could be made to satisfy the entire set of observations.

3. Surface waves

The above properties of seismic attenuation in the earth affect surface waves and body waves differently, so these two modes of energy propagation are considered separately below. For our purposes, the important distinctions between surface and body waves are the typically fewer number of

wavelengths per total propagation path and the generally narrower width of the relevant frequency band of the former relative to the latter. These distinctions imply that the amplitudes of Love and Rayleigh waves from a given seismic event are less controlled by anelastic losses than are those of P and S waves, and that surface-wave amplitudes are generally less sensitive than those of body waves to the frequency dependence of Q.

Principally because Q in the earth is a strong function of depth, the attenuation of surface waves is period-dependent. The contribution of any depth interval in the earth to the attenuation of a surface wave is proportional to the fractional potential energy stored per cycle within that interval (Anderson & Archambeau 1964). In Figure 1 is shown the fractional potential energy per unit depth stored per cycle for Rayleigh waves of 10, 20 and 40 sec periods. The boundary between high-Q lithosphere and low-Q asthenosphere is indicated schematically at a depth of 60 km. Discontinuities in the energy as a function of depth are due to abrupt changes in the elastic properties of the particular velocity-density model used, the shield model of Harkrider & Anderson (1966). The important point of Figure 1 is that Rayleigh waves of 10- and 20-sec period store a relatively small fraction (.002 and 5 percent, respectively) of their strain energy in the low-Q

asthenosphere, while 40-sec Rayleigh waves store over half their potential energy per cycle below 60 km depth. Thus in regions of the earth where Q in the asthenosphere is low, the attenuation of surface waves of 40 sec period should be more pronounced than at shorter periods. At periods less than about 10 to 15 sec, surface-wave attenuation is very sensitive to near-surface values of Q (see Figure 1) which can also be path-dependent. For oceanic or continental paths crossing sediment basins, for instance, surface-wave attenuation at these periods might be expected to be severe.

In Figures 2 and 3 are given the measured Love-wave and Rayleigh-wave attenuation (Q_L^{-1} and Q_R^{-1}) for east-central and western United States and for predominantly ocean paths. The values for western U.S. were reported earlier (Solomon 1972); those for east-central U.S. were determined using standard two-station techniques from surface waves which had traveled between WWSSN stations at Rapid City, South Dakota (RCD) and Atlanta, Georgia (ATL). Details of both sets of measurements may be found in Solomon (1971).

At periods less than 25 to 30 seconds, Q_L and Q_R exceed 200 and are not markedly path-dependent. This reflects the uniformly high Q of the lithosphere. At longer periods, both Q_R^{-1} and Q_L^{-1} generally increase with increasing period, due to the relatively larger fraction of energy stored in the

asthenosphere at these periods. Further, since lateral variations in the anelastic properties of the earth are pronounced within the asthenosphere, the regional differences in surface-wave attenuation are greatest in the period range 30 to about 100 sec. Q_R^{-1} and Q_L^{-1} for the tectonically active western U.S. are consistently larger in this period range than for the more stable regions to the east.

These findings have considerable significance for the interpretation of surface-wave magnitudes and spectra. In Figure 4 is shown the vertical displacement amplitude spectrum of a Rayleigh wave from a nuclear explosion (Tsai & Aki 1971). Also shown are the Rayleigh-wave spectra predicted for 3000-km propagation paths through "western U.S." and "eastern U.S." (A flat earth has been assumed, so that geometrical spreading is ignored.) At periods less than 25 sec, the attenuated spectra are quite similar. In particular, the surface-wave magnitude, if computed from the amplitude of 20-sec waves (Gutenberg 1945), would be identical for western and eastern U.S. paths.

At periods longer than 25 sec, the two attenuated spectra diverge. Thus some concern for propagation path must be exercised if one bases a discrimination criterion on the amplitudes of 40 sec surface waves (Molnar et al.1970; Savino et al. 1971). Still, differences in surface-wave "magnitude"

would amount to less than .1 at periods of 40 to 50 sec, and less than .3 at periods near 30 sec for the two 3000-km paths.

Another cautionary note should be raised. Anelastic losses do affect the shape of surface-wave amplitude spectra (Figure 4). Thus discrimination criteria based on the sensitivity of surface-wave spectral shape to depth of focus (Tsai & Aki 1971) require accurate knowledge of Q. The attenuated spectra of Figure 4, if "corrected" for attenuation by assuming Q_R is proportional to frequency (Tsai & Aki 1970, 1971), would appear to be from an event as deep as 5 km (see Figures 5, 6 and 7 of Tsai & Aki 1971). Such an event might be incorrectly classified as an earthquake if good azimuthal coverage were not possible or if other discrimination criteria were not available.

4. Body waves

The amplitudes of P and S waves depend critically on both the spatial and frequency dependence of Q in the earth. Because Q in the lithosphere is high, the attenuation correction for P and S waves recorded within a few hundred km of the source

will be small and insensitive to regional variations. For source-receiver distances greater than about 1000 km, direct P and S waves must propagate through the asthenosphere or low-velocity zone, in which the waves are strongly damped and within which lateral variations in Q can noticeably alter the relative amplitudes between different stations.

One measure of the lateral variation of Q in the asthenosphere of North America is the differential attenuation of long-period body waves (Solomon & Toksöz 1970), mapped for P waves in Figure 5. The differential attenuation δt^* at a seismometer station is related to the difference between the value of Q^{-1} in the upper mantle beneath the station and the average $\overline{Q^{-1}}$ for a spherically symmetric earth:

$$\delta t^* = \pi \int_S [Q^{-1} - \overline{Q^{-1}}] v^{-1} ds$$

where ds is an increment of distance along the ray path S and v is the wave velocity. In practice, the difference between δt^* at two stations is given by the negative of the slope of the body-wave spectral ratio, corrected for the different distances from the source to the two stations, versus frequency. Sources of body waves used to determine values of δt^* in Figure 5 were deep earthquakes at distances greater than 40 degrees, so that variations in Q along near-source

segments of paths were minimized.

In Figure 5 may be seen a large area of above-average attenuation (positive δt^*) of P waves between the Rocky Mountain front and the Sierra Nevada-Cascade ranges. One consequence of Figure 5, if variations in upper mantle Q^{-1} implied by differences in δt^* may be at least qualitatively extrapolated to higher frequencies, is that the magnitudes of P waves recorded from teleseismic events at stations in the Basin and Range and Rocky Mountain provinces should be smaller than those determined at eastern U.S. stations. This is generally observed (Cleary 1967; Evernden & Clark 1970). A second consequence is that the body-wave magnitude m_b of earthquakes in the Basin and Range province should be less than for earthquakes of comparable surface wave magnitude M_S in the neighboring California Border and Great Plains provinces, providing that body waves are recorded at teleseismic distances, that surface waves of period 20 sec or less are used to determine M_S, and that depth of focus and other source parameters are similar for earthquakes in the two regions.

As a test of this latter hypothesis, we reproduce in Figure 6 Basham's (1969) measurements at Canadian stations of m_b and M_S for earthquakes and explosions in southwestern North America. Unlike Basham's original figure, the earthquake

population is segregated into two groups: (i) those that occur within the zone of high attenuation in Figure 5 (10 in the Basin and Range Province and 6 in the Gulf of California), and (ii) those that occur outside the zone (8 in the California Border Province, 2 in western Baja, California and 1 near Denver). The earthquakes in group (ii) cluster very tightly about a straight line. With one exception, earthquakes in group (i) lie well above that line. From the fitting of straight lines, using a least-squared-error criterion, to the two populations, it may be concluded that in the m_b range 4.5 to 5.5 earthquakes of a given surface wave magnitude in the Basin and Range-Gulf of California region show apparent body wave magnitudes 0.3 to 0.4 less than do comparable earthquakes in adjacent areas (principally the San Andreas region of California). This conclusion receives support from the more recent measurements of Savino et al. (1971); see Figure 1 of their paper. That this difference in the $M_S - m_b$ curve is due to lateral variations of Q^{-1} in the upper mantle is strongly suggested, though not proven. Differences in average depth of focus or source volume for earthquakes of the two areas is another possible explanation. The typically shallow depth of earthquakes in both regions, however, and the finding by Wyss & Brune (1968) that source dimensions of earthquakes in the Nevada-Arizona region are

similar to or smaller than those on the San Andreas fault system are compelling arguments that the latter explanation is not valid.

Thus the attenuative properties of a medium can significantly alter the $M_S - m_b$ relationship, the criterion most used to discriminate underground nuclear explosions from earthquakes. The anomalous $M_S - m_b$ pattern in western North America is at least in part due to greater-than-average attenuation of P waves in the upper mantle of that region (cf. Ward & Toksöz 1971). (The single Basin and Range earthquake of $M_S = 4.4$ shown in Figure 6 with an unusually large m_b serves to emphasize, though, that attenuation is not the only parameter controlling the $M_S - m_b$ relation for a region.) Even more importantly, by considering in Figure 6 only those earthquakes and explosions which occur in the same tectonic region (NTS is in the Basin and Range province) a more effective separation of explosion and earthquake populations is achieved than if all earthquakes from western North America are lumped into a single category.

Knowledge of the frequency dependence of Q in the earth, particularly within the low-Q asthenosphere, is exceedingly important if body-wave spectra are to be correctly interpreted in terms of source parameters. Seismological evidence currently supports the hypothesis that the asthenosphere,

especially in tectonic and oceanic areas, is partially melted (Anderson & Sammis 1970). Walsh's (1969) model for attenuation in partially melted rock has been successfully applied both to laboratory experiments and to seismic-wave absorption in the asthenosphere; a thorough discussion is given in Solomon (1972). The important predictions of Walsh's model are that losses in compression are negligible compared with losses in shear, verified for the earth by the work of Anderson et al. (1965), Solomon & Toksöz (1970), and others; and that Q_μ in shear behaves as for a relaxation process, illustrated in Figure 7. Both elastic modulus and Q are frequency dependent; there is a peak in the attenuation at an angular frequency ω equal to $1/\tau$, where τ is a characteristic time determined in Walsh's model by such properties as the viscosity and volume concentration of the melt and geometry of the melt-solid interfaces. At frequencies much less than $1/\tau$, Q^{-1} is proportional to frequency; at frequencies much greater than $1/\tau$, Q^{-1} is inversely proportional to frequency. Note that the attenuation peak in a partial melt can be no sharper than that shown in Figure 7, according to Walsh's model. In a more realistic parameterization of partially melted rock, the peak would be "smeared out" due to a superposition of several such relaxations.

An idealized shear-wave spectrum from an earthquake

source (Aki 1967; Brune 1970) is shown in Figure 8, together with the spectra expected after propagation at vertical incidence through two simple models of an attenuating upper mantle. In one, $Q_\mu = 100$ independent of frequency; in the second, Q_μ is given by Figure 7, with $2\pi\tau = 10$ sec and $Q_{min} = 20$. In both models, the attenuating zone is 300 km thick. At a frequency of about 1 Hz, Q_μ is identical in the two models.

The two attenuated spectra are quite different both in absolute amplitude and in spectral shape. If these two spectra were not corrected for absorption, then the measured "corner frequencies," diagnostic of source dimensions (Aki 1967; Brune 1970), might differ by a factor of 3 or more. The fall-off of spectral amplitude with frequency at frequencies greater than the corner value is related to fractional stress drop in Brune's (1970) model. Figure 8 demonstrates the impossibility of extracting such information if the attenuation is not well known. We should note that the amplitude changes produced by the above two simple models for upper-mantle attenuation are something of a maximum: if P waves rather than S waves were employed, if near-field rather than teleseismic observations were used to calculate spectra, or if the recording site were on a shield instead of a tectonic region, then the effects of attenuation on

spectral amplitudes would be less severe.

A partially melted asthenosphere has an attenuation spectrum more complicated than the single relaxation peak of Figure 7. In Figure 9 is shown a model of Q_μ, a function of both frequency and depth, in the upper mantle of western United States (Solomon 1972). There are at least three distinct relaxation peaks, each operative over a somewhat different depth interval. In Figure 10 is given the amplitude spectrum of a shear wave that has propagated vertically through the upper mantle of western U.S. Also shown are the assumed source spectrum and the attenuated spectrum for a constant-Q asthenosphere, both taken from Figure 8. As noted before, the corner frequencies and the overall shape of observed body-wave spectra are quite strongly dependent on the frequency dependence of Q in the upper mantle.

Workers interested in source spectra generally apply <u>some</u> correction for attenuation to the measured amplitudes. It is of interest to inquire what effect applying the wrong Q correction would have on the interpretation of spectral shape. In Figure 10 is shown the source spectrum that would have been calculated if the spectrum measured in western U.S. had been "corrected" by using the constant-Q model. Such a spectrum "corrected" to the source has a spurious relative maximum and a precipitous decrease in amplitude

with increasing frequency at frequencies in excess of the "peak" value. If the amplitudes of Figure 10 had been measured only at frequencies greater than .1 Hz or so, the "peak" would appear to be an absolute maximum. Inasmuch as Wyss et al. (1971) have proposed that such a peak in body-wave amplitude spectrum is diagnostic of an explosion source, the need for properly understanding the nature of Q in the earth before correcting spectra for attenuation is clearly demonstrated. It should be emphasized, however, that the above discussion in no way alters the conclusions of Wyss et al. (1971). Their findings were based on the recordings at a single fixed station of waves from explosions and earthquakes located within a single, small region. Further, the spectral peaks reported by Wyss et al. were present in the data before any attenuation correction. Note that a relaxation peak in Q^{-1} can never produce a relative maximum in an amplitude spectrum that is, prior to any attenuation, flat or a monotonically decreasing function of frequency. This is because Q^{-1} never decreases with increasing frequency f faster than as f^{-1} in the relaxation model.

5. Conclusions

Seismic-wave attenuation in the earth acts as a complicated low-pass filter for signals from all seismic sources. The important considerations discussed above that pertain to the problems of describing the seismic source in general and of discriminating earthquakes from underground nuclear explosions in particular may be summarized as follows:

1. Q in the earth is a function of space and frequency.

2. The effect of attenuation on amplitudes is not pronounced if all or nearly all of the energy of a wave propagates in the lithosphere below a few km depth. Examples include P and S waves recorded within about 1000 km of a shallow source and Love and Rayleigh waves in the period range 30 to about 15 sec.

3. If a major fraction of the wave energy propagates in the low-Q asthenosphere, then proper interpretation of source parameters requires consideration of the lateral variation and frequency dependence of Q.

4. Lateral variation of Q affects only mildly the

estimation of surface-wave magnitude. After propagating 3000 km through a tectonic region, as contrasted with a stable continental region, the surface-wave magnitude would be negligibly different at 20 sec and .1 to .3 magnitude units less at periods greater than 30 sec.

5. The shape of surface-wave amplitude spectra is governed to some extent by attenuation. The effect is most likely to increase the estimate of focal depth from spectral shape of waves from explosions if multi-azimuth observations are not available.

6. Body-wave magnitude is noticeably affected by the lateral variation of Q. The magnitude can be lower by at least several tenths of a magnitude unit in tectonically active as opposed to stable regions. An implication is that any comparison of body-wave amplitudes from earthquakes and explosions should be restricted to events from the same tectonic province.

7. Body-wave spectral shape is strongly influenced by the frequency dependence of Q. In particular, estimation of source dimensions or fractional stress drop may be in error or a spurious spectral peak may be introduced by improperly accounting for attenuation.

Acknowledgments

I thank M. Nafi Toksöz and Bruce Julian for reviewing this manuscript. I was fortunate to have been a Postdoctoral Fellow of the National Science Foundation during this investigation.

This research was supported by the Advanced Research Projects Agency and monitored by the Air Force Office of Scientific Research under contract F44620-71-C-0049.

REFERENCES

Aki, K., 1967. Scaling law of seismic spectrum, J. geophys. Res., 72, 1217-1231.

Anderson, D.L. & Archambeau, C.B., 1964. The anelasticity of the earth, J. geophys. Res., 69, 2071-2084.

Anderson, D.L., Ben-Menahem, A. & Archambeau, C.B., 1965. Attenuation of seismic energy in the upper mantle, J. geophys. Res., 70, 1441-1448.

Anderson, D.L. & Sammis, C., 1970. Partial melting and the low-velocity zone, Phys. Earth Planet. Interiors, 3, 41-50.

Archambeau, C.B., Flinn, E.A. & Lambert, D.G., 1969. Fine structure of the upper mantle, J. geophys. Res., 74, 5825-5865.

Asada, T. & Takano, K., 1963. Attenuation of short period P waves in the mantle, J. Phys. Earth, 11, 25-34.

Basham, P.W., 1969. Canadian magnitudes of earthquakes and nuclear explosions in southwestern North America, Geophys. J. R. astr. Soc., 17, 1-13.

Brune, J.N., 1970. Tectonic stress and the spectra of seismic shear waves from earthquakes, J. geophys. Res., 75, 4997-5009.

Cleary, J., 1967. Analysis of the amplitudes of short-period P waves recorded by Long Range Seismic Measurements stations in the distance range 30° to 102°, J. geophys. Res., 72, 4705-4712.

Evernden, J.F. & Clark, D.M., 1970. Study of teleseismic P, 2, Amplitude data, Phys. Earth Planet. Interiors, 4, 24-31.

Fedotov, S.A. & Boldyrev, S.A., 1969. Frequency dependence of the body-wave absorption in the crust and upper mantle of the Kuril-Island chain, Bull. Acad. Sci. USSR, Geophys. Ser., English Transl., no. 9, 553-562.

Filson, J.R., 1971. A direct measurement of the Earth's short period attenuation, in Seismic Discrimination, Semiannual Technical Summary Report to the Advanced Research Projects Agency, 1 July - 31 December 1970, Lincoln Laboratory, Massachusetts Institute of Technology, Lexington, 19-21.

Frantti, G.E., 1965. Attenuation of P_n waves from offshore Maine explosions, Bull. seism. Soc. Am., 55, 417-423.

Gutenberg, B., 1945. Amplitudes of surface waves and magnitudes of shallow earthquakes, Bull. seism. Soc. Am., 35, 3-12.

Harkrider, D.G., 1964. Surface waves in multilayered elastic media, 1, Rayleigh and Love waves from buried sources in a multilayered elastic half-space, Bull. seism. Soc. Am., 54, 627-679.

Harkrider, D.G. & Anderson, D.L., 1966. Surface wave energy from point sources in plane layered earth models, J. geophys. Res., 71, 2967-2980.

Hirasawa, T. & Takano, K., 1966. Differential attenuation of P waves as derived from a Hindu-Kush earthquake, J. Phys. Earth, 14, 49-57.

Isacks, B., Oliver, J. & Sykes, L.R., 1968. Seismology and the new global tectonics, J. geophys. Res., 73, 5855-5899.

Jackson, D.D., 1972. The attenuation of Love waves and toroidal oscillations of the earth, Geophys. J. R. astr. Soc., in press.

Kanamori, H., 1967. Spectrum of P and PcP in relation to the mantle-core boundary and attenuation in the mantle, J. geophys. Res., 72, 559-571.

Kurita, T., Attenuation of short-period P-waves and Q in the mantle, J. Phys. Earth, 16, 61-78.

Mendoza L.,E., 1970. Attenuation of short-period P waves in the central Andes (in Spanish), Publication No. 8, San Calixto Observatory, La Paz, Bolivia, 109 pp.

Molnar, P. & Oliver, J., 1969. Lateral variations of attenuation in the upper mantle and discontinuities in the lithosphere, J. geophys. Res., 74, 2648-2682.

Molnar, P., Savino, J., Sykes, L.R., Liebermann, R.C., Hade, G. & Pomeroy, P.W., 1969. Small earthquakes and explosions in western North America recorded by new high gain, long period seismographs, Nature, 224, 1268-1273.

Oliver, J. & Isacks, B., 1967. Deep earthquake zones, anomalous structures in the upper mantle, and the lithosphere, J. geophys. Res., 72, 4259-4275.

Savino, J., Sykes, L.R., Liebermann, R.C. & Molnar, P., 1971. Excitation of seismic surface waves with periods of 15 to 70 seconds for earthquakes and underground explosions, J. geophys. Res., 76, 8003-8020.

Solomon, S.C., 1971. Seismic-wave attenuation and the state of the upper mentle, Ph.D. thesis, Massachusetts Institute of Technology, Cambridge, 321 pp.

Solomon, S.C., 1972. Seismic -wave attenuation and partial melting in the upper mantle of North America, J. geophys. Res., 77, in press.

Solomon, S.C. & Toksöz, M.N., 1970. Lateral variation of attenuation of P and S waves beneath the United States, Bull. seism. Soc. Am., 60, 819-838.

Sumner, R.D., 1967. Attenuation of earthquake generated P waves along the western flank of the Andes, Bull. seism. Soc. Am., 57, 173-190,

Teng, T.L., 1968. Attenuation of body waves and the Q structure of the mantle, J. geophys. Res., 73, 2195-2208.

Tsai, Y.B. & Aki, K., 1969. Simultaneous determination of the seismic moment and attenuation of seismic surface waves, Bull. seism. Soc. Am., 59, 275-287.

Tsai, Y.B. & Aki,K.,1970 Precise focal depth determination from amplitude spectra of surface waves, J. geophys. Res., 75, 5729-5743.

Tsai, Y.B. & Aki, K., 1971. Amplitude spectra of surface waves from small earthquakes and underground nuclear explosions, J. geophys. Res., 76, 3940-3952.

Wadati, K. & Hirono, T., 1956. Magnitude of earthquakes - especially of near, deep-focus earthquakes, Geophys. Mag., 27, 1-10.

Walsh, J.B., 1969. A new analysis of attenuation in partially melted rock, J. geophys. Res., 74, 4333-4337.

Ward, R.W. & Toksöz, M.N., 1971. Causes of regional variation of magnitudes, Bull. seism. Soc. Am., 61, 649-670.

Wyss, M. & Brune, J.N., 1968. Seismic moment, stress, and source dimensions for earthquakes in the California-Nevada region, J. geophys. Res., 73, 4681-4694.

Wyss, M., Hanks, T.C. & Liebermann, R.C., 1971. Comparison of P-wave spectra of underground explosions and earthquakes, J. geophys. Res., 76, 2716-2729.

FIGURE CAPTIONS

Fig. 1. Fractional potential energy per km depth stored per cycle for Rayleigh waves of various periods T. The computational technique used to determine these curves is from Harkrider (1964). The velocity-density model is the shield model of Harkrider and Anderson (1966). The approximate boundary between high-Q lithosphere and low-Q asthenosphere (shaded) is also illustrated.

Fig. 2. Love-wave attenuation, Q_L^{-1}, *versus* frequency, f, (semi-log scale). The data of Anderson *et al.* (1965) and Tsai & Aki (1969) are for primarily oceanic paths. Values for western U.S. are from Solomon (1972). The surface wave path for east-central U.S. is between Rapid City, South Dakota, and Atlanta, Georgia. Error bars, showing standard deviations for selected determinations, indicate the precision of the measurements.

Fig. 3. Rayleigh-wave attenuation, Q_R^{-1}, *versus* frequency, f, (semi-log scale). Wave paths, error bars, and sources

of data are as in Figure 2.

Fig. 4. Rayleigh-wave vertical displacement amplitude spectrum from a nuclear explosion buried .5 km in tuff (Tsai & Aki 1971) and the spectra expected after propagation of such a wave through western and east-central United States (W.U.S. and E.U.S., respectively). A path length of 3000 km is assumed and geometrical spreading is ignored.

Fig. 5. Lateral variation of the differential attenuation δt_p^* of long-period P waves in the United States (from Solomon & Toksöz, 1970, with slight revisions). δt_p^*, in seconds, is the average of attenuation measurements for two deep earthquakes in South America. Dashed lines approximate the $\delta t_p^* = 0$ contours.

Fig. 6. Surface-wave magnitude, M_S, versus body-wave magnitude, m_b, for events in southwestern North America. M_S and m_b were measured at stations in the Canadian Network by Basham (1969). Earthquakes represented by solid symbols are located in regions of negative δt_p^* in Figure 5; those given by open symbols are located in regions of high attenuation (positive δt_p^*)

in Figure 6. Straight lines are (lowest line) Basham's fit to nuclear explosion data and (upper two lines) least-squared error fits to the two earthquake populations.

Fig. 7. Elastic modulus M and attenuation Q^{-1} for a relaxation process. M_U is the unrelaxed, or high-frequency, modulus; Q_{min} is the minimum value of Q; ω is the angular frequency; and τ is a characteristic time. A relaxation occurs at $\omega\tau = 1$.

Fig. 8. Shear-wave spectral amplitude from an idealized earthquake source (Aki 1967; Brune 1970) and the spectra expected after propagation of such a wave at vertical incidence through two simple models of upper mantle Q: (i) $Q = 100$ in a layer 300 km thick, and is infinite elsewhere; (ii) Q is given by the curve of Figure 7, with $2\pi\tau = 10$ sec and $Q_{min} = 20$, in a layer 300 km thick, and is infinite elsewhere.

Fig. 9. Q_μ^{-1} in western United States (Solomon 1972). Q_μ^{-1} is independent of frequency f above 60 km, and depends on frequency as shown in the inserts (semi-log scale) for the two layers 60 to 160 km deep and

and 160 to 350 km deep. $100/Q_\mu$ is plotted as a function of depth z for two specific frequencies.

Fig. 10. Shear-wave spectral amplitude from an idealized earthquake source (Aki 1967; Brune 1970) and the spectra expected after propagation of such a wave at vertical incidence through the Q model of Figure 9 ("Western U.S.") and the constant-Q model from Figure 8 ("Q = 100"). The curve labeled "'corrected' to source" is the source spectrum that would have been obtained if the western U.S. curve had been corrected for attenuation by using the constant-Q model.

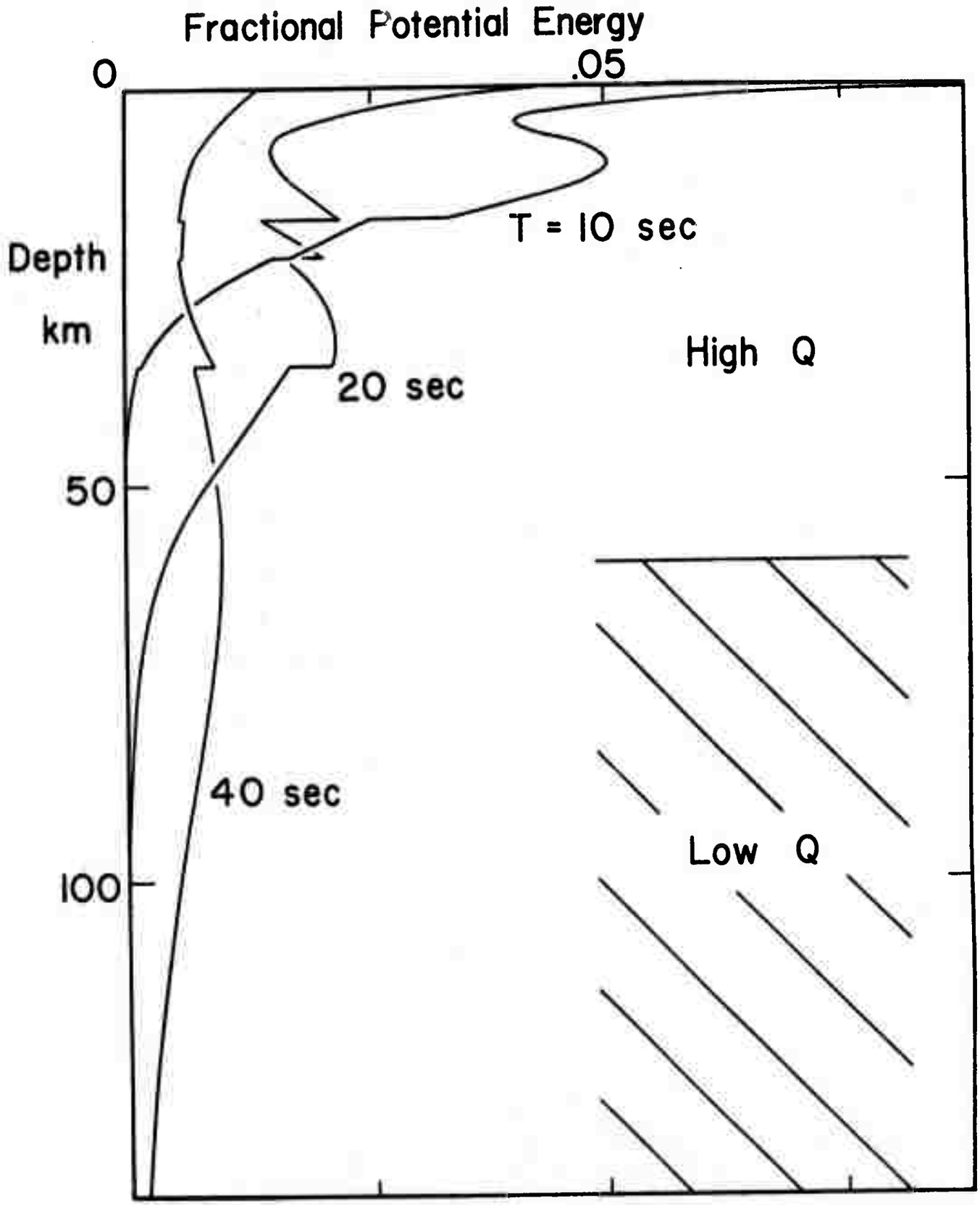
Fractional Potential Energy
0
.05
T = 10 sec
Depth
km
High Q
20 sec
50
40 sec
Low Q
100

Figure 1

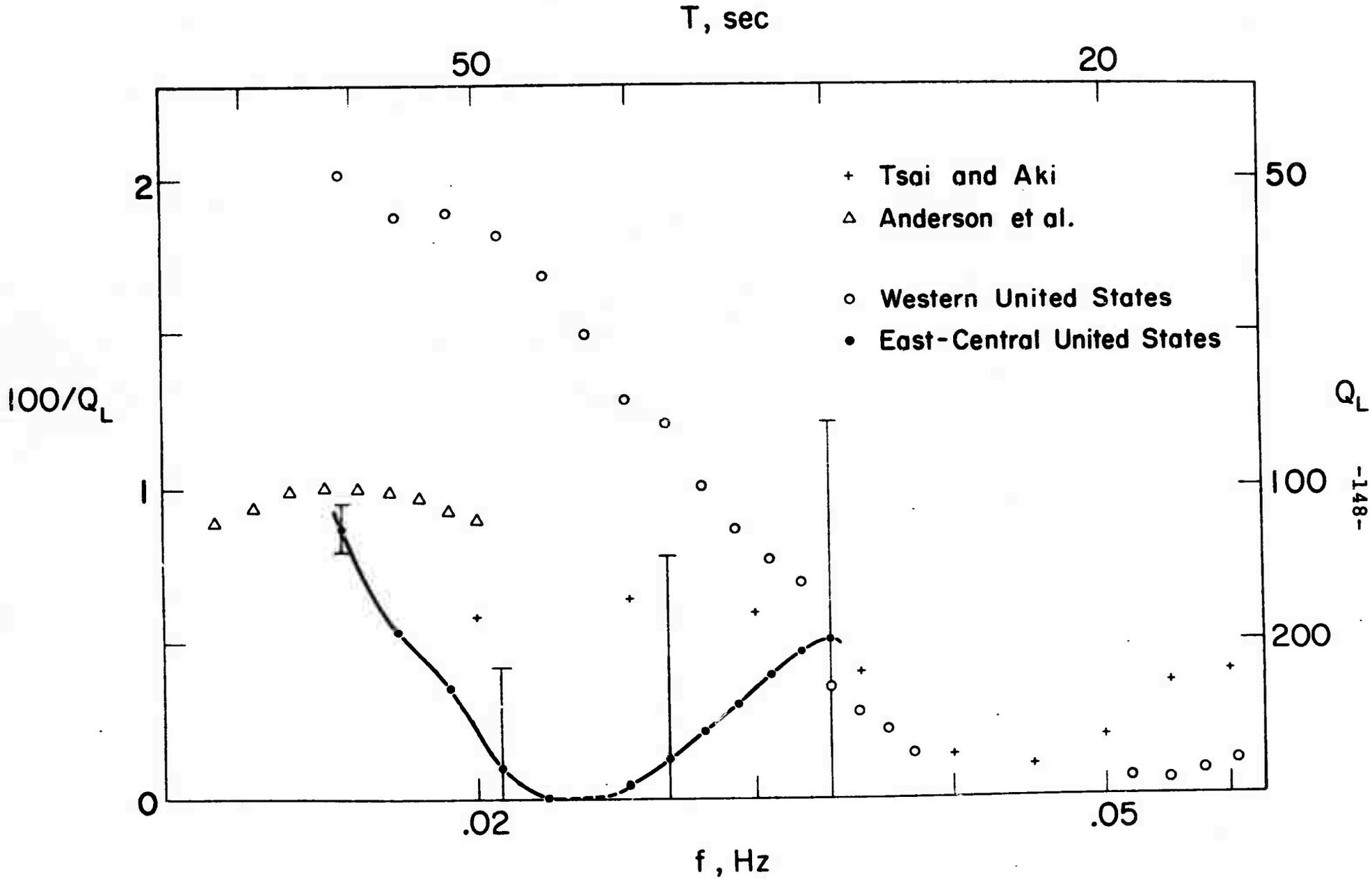
T, sec
50
20
2
1
0
100/Q_L
Q_L
50
100
200
.02
.05
f, Hz
+ Tsai and Aki
△ Anderson et al.
○ Western United States
• East-Central United States

Figure 2

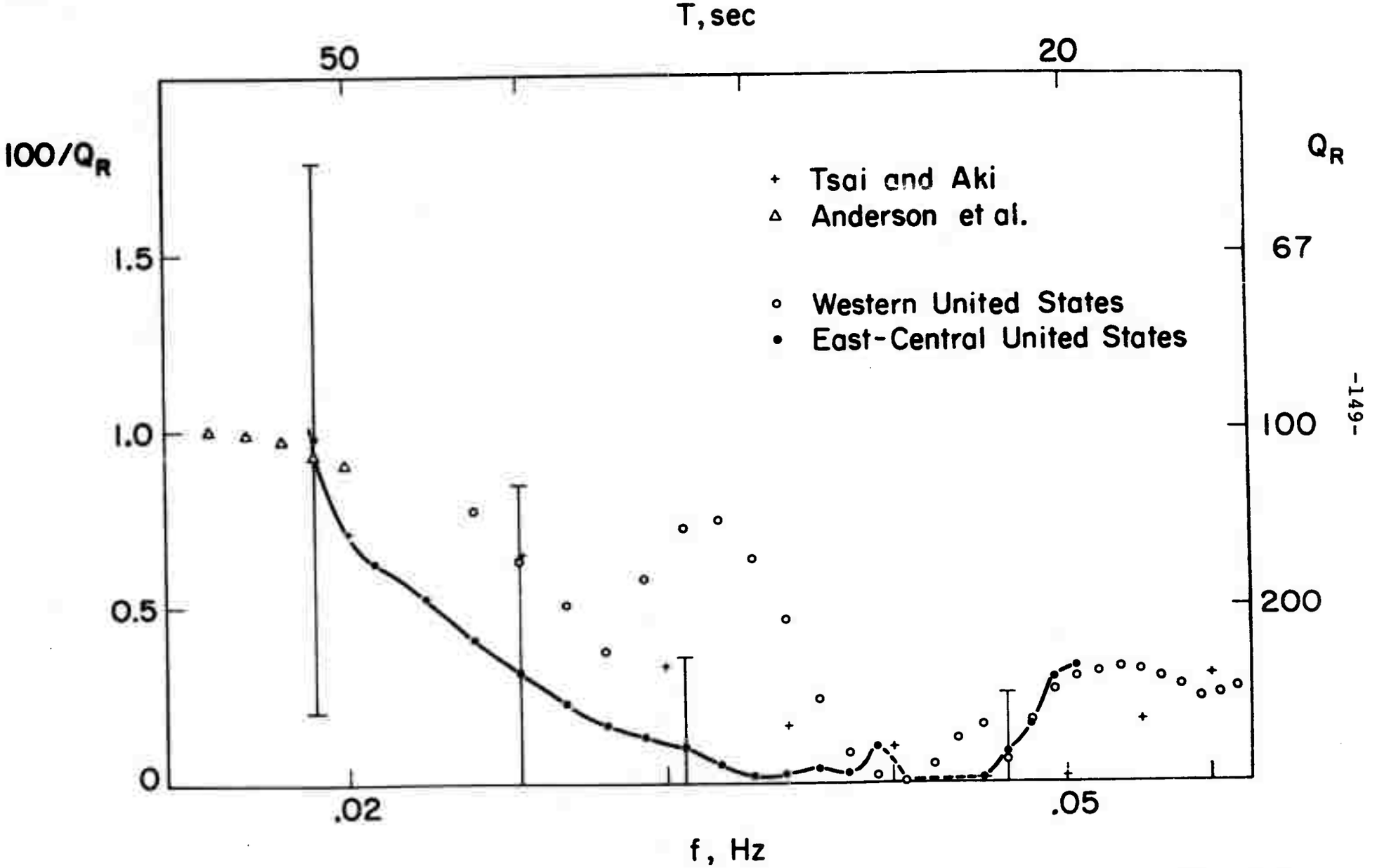
T, sec
50
20
100/Q_R
Q_R
Tsai and Aki
Anderson et al.
Western United States
East-Central United States
1.5
1.0
0.5
0
67
100
200
.02
.05
f, Hz

Figure 3

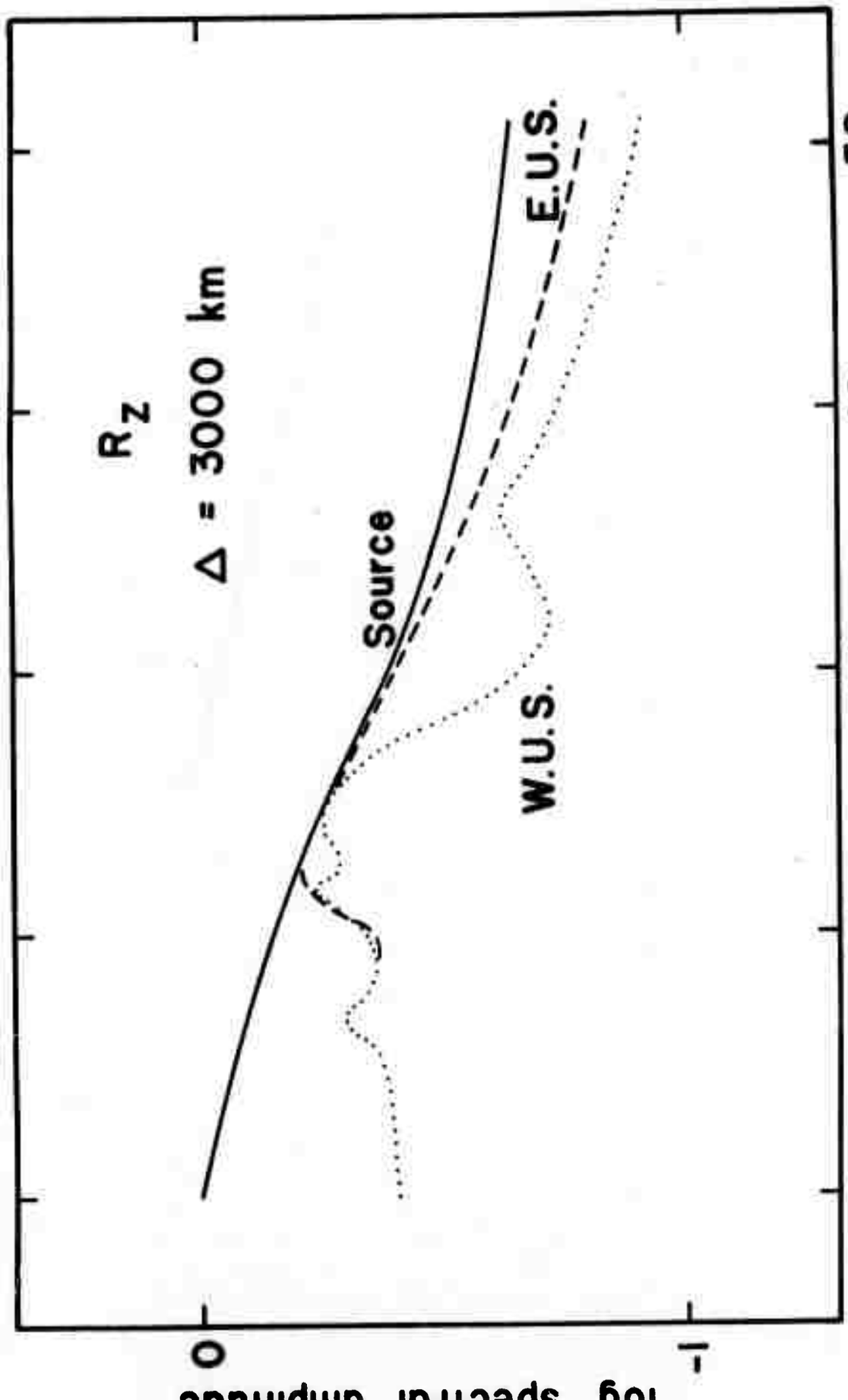
log spectral amplitude
0
-1
10
20
30
40
50
T, sec
R_Z
Δ = 3000 km
Source
E.U.S.
W.U.S.

Figure 4

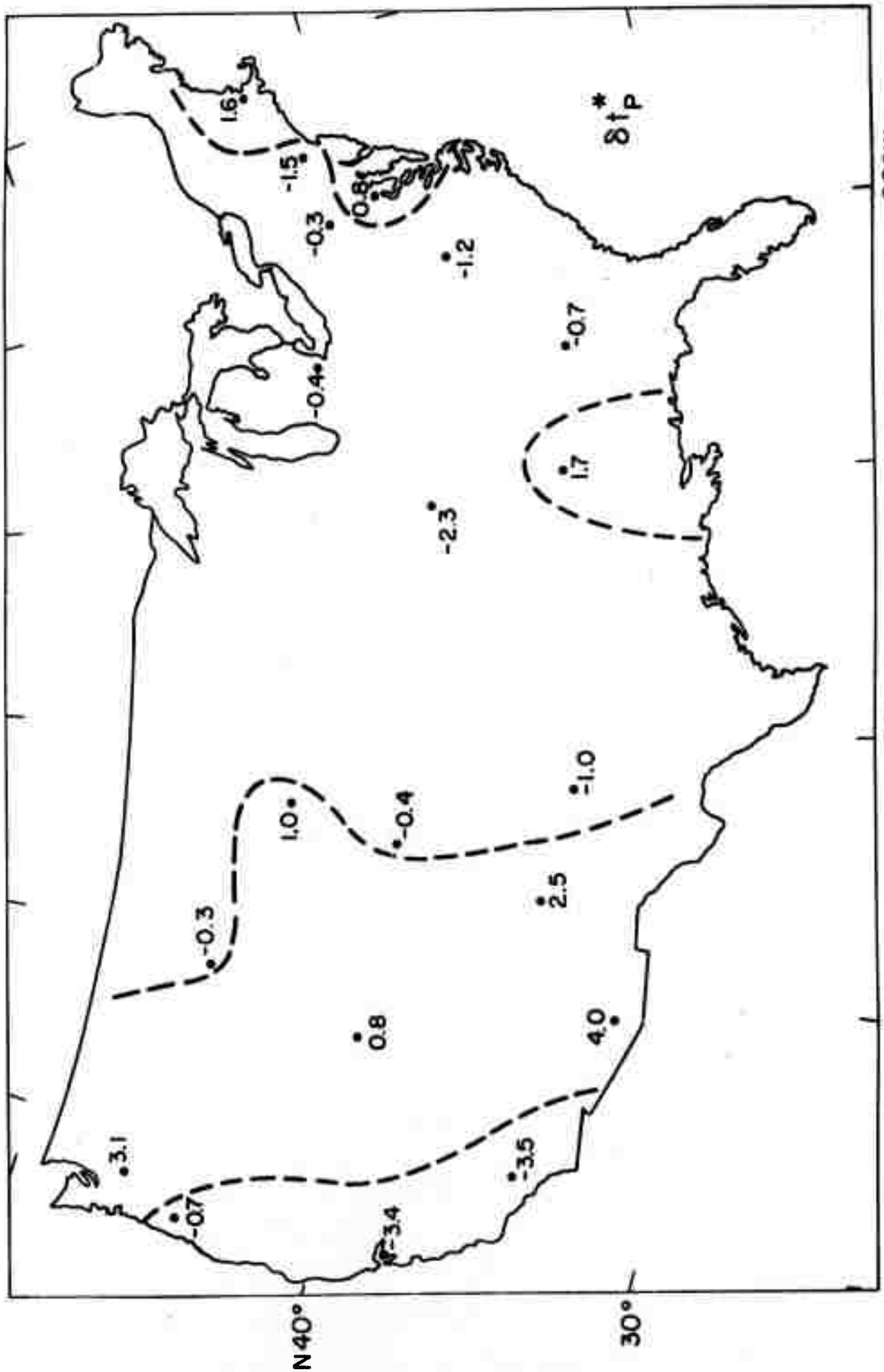
N40°
30°
100°
80°W
δt_p^*
1.6
-1.5
-0.8
-0.3
-1.2
-0.7
-0.4
1.7
-2.3
1.0
-0.4
1.0
-0.3
2.5
0.8
4.0
3.1
-0.7
3.4
3.5

Figure 5

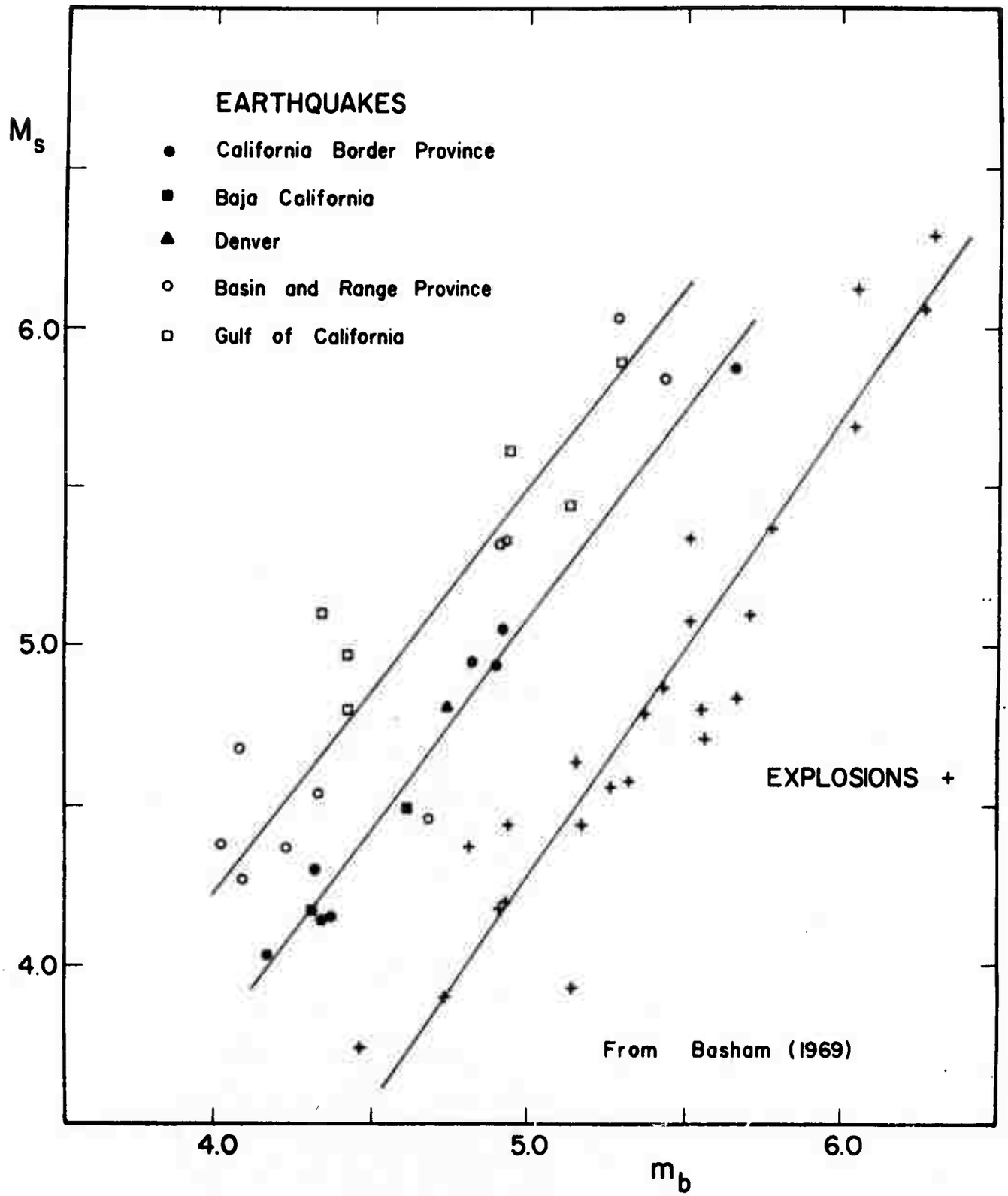
EARTHQUAKES
California Border Province
Baja California
Denver
Basin and Range Province
Gulf of California
EXPLOSIONS +
From Basham (1969)
M_s
m_b
6.0
5.0
4.0
4.0
5.0
6.0

Figure 6

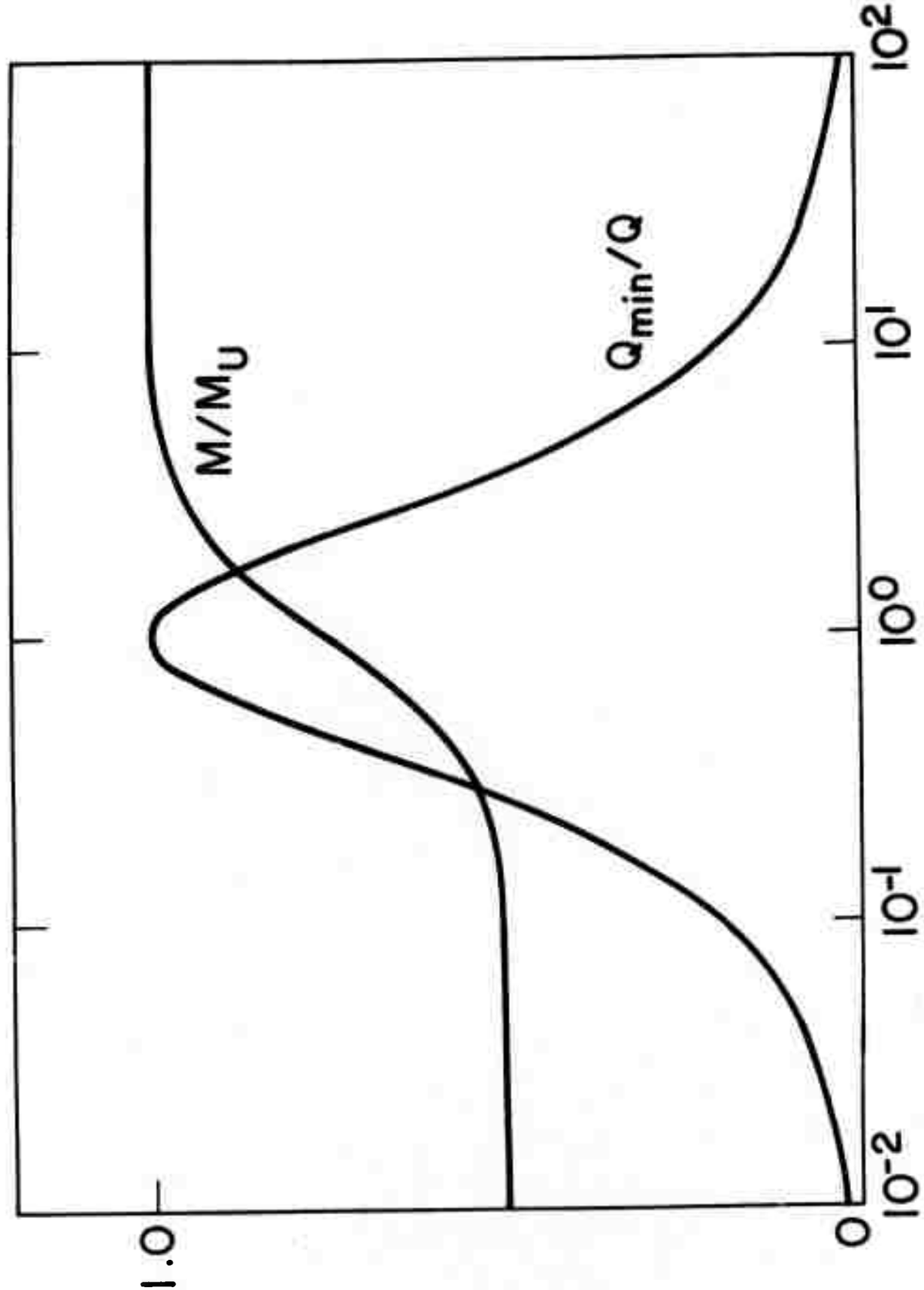

Figure 7

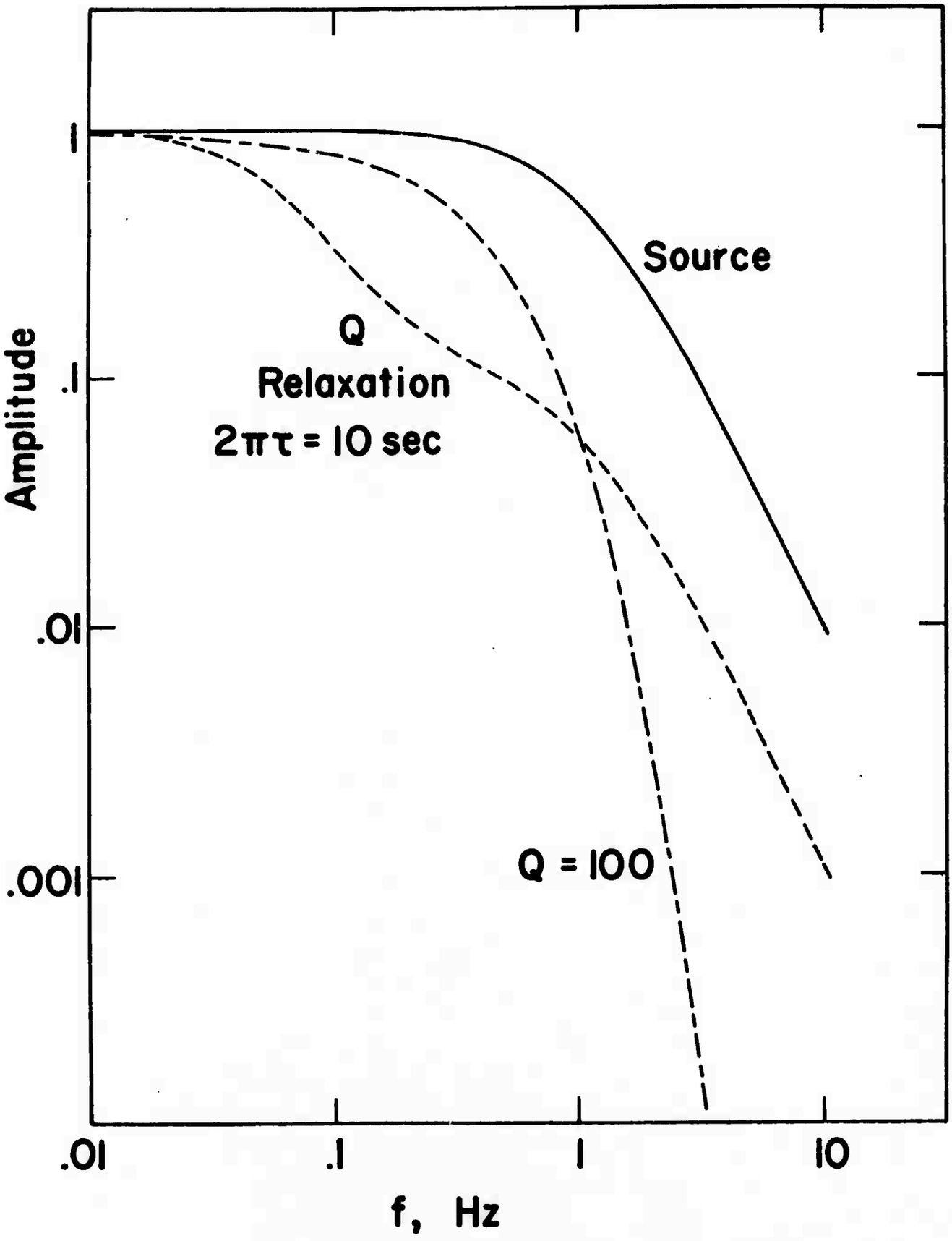
Source
Q
Relaxation
2πτ = 10 sec
Q = 100
Amplitude
1
.1
.01
.001
.01
.1
1
10
f, Hz

Figure 8

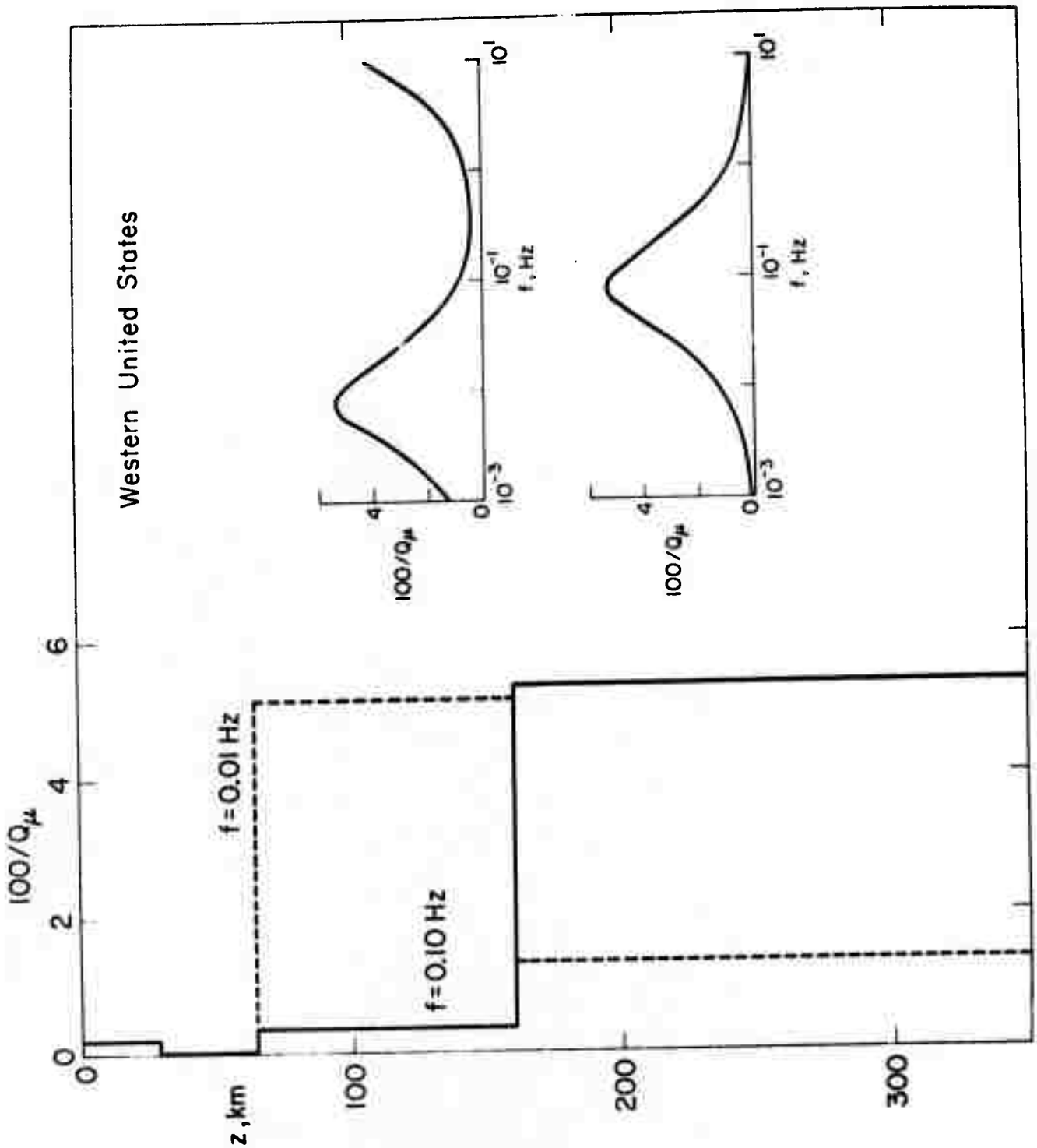
Western United States
100/Qμ
0
2
4
6
f=0.01 Hz
f=0.10 Hz
z, km
0
100
200
300
10⁻³
10⁻¹
10¹
f, Hz
4
0

Figure 9

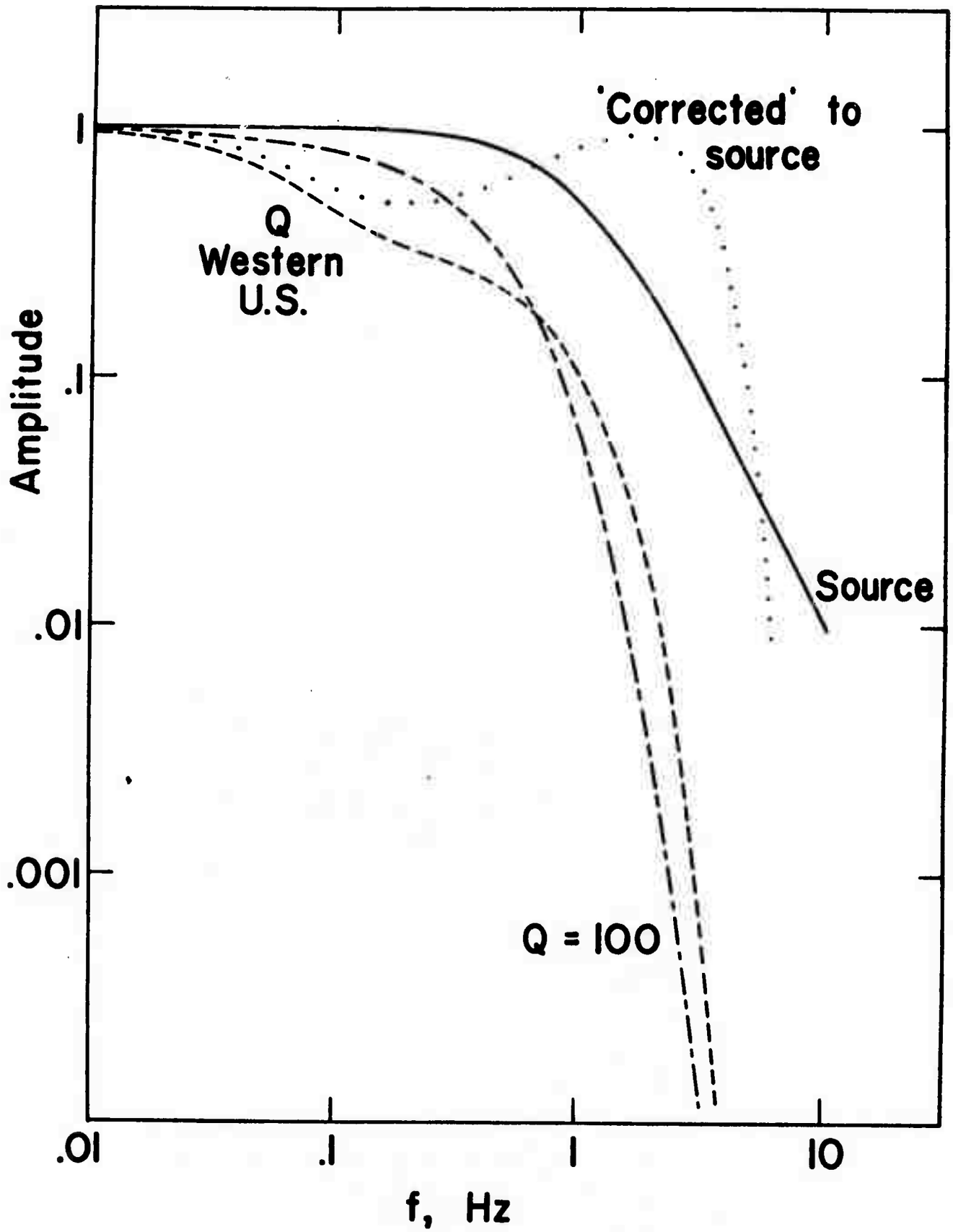
'Corrected' to source
Q Western U.S.
Source
Q = 100
Amplitude
1
.1
.01
.001
.01
.1
1
10
f, Hz

Figure 10

4.3 Stress Distribution Beneath Island Arcs by Albert T. Smith, Jr. and M. Nafi Toksöz

Summary

A numerical simulation of the descending lithosphere under island arcs is developed in order to describe stress distribution derived from earthquakes. The lithospheric slab and the adjacent mantle are simulated as an elastostatic problem with moduli corresponding to their effective rheologies. Assuming similar composition for the lithosphere and mantle and given the temperature regime for the mantle, gravitational body forces generated by thermal volume contraction of the colder slab and by elevation of phase boundaries are included. In addition, simulated convection is applied to the slab in order to distinguish its role as a driving mechanism. The regional applicability of gravitational sinking is then clarified using a simple numerical integration of the equilibrium equation and comparing this to available information for select island arcs. These analogues suggest a viable hypothesis for the dynamics of the subjecting lithosphere.

First, gravitational sinking induced by thermal density anomalies can explain the directions of the principle stress within the descending slab at island arcs without recourse to convective effects in the adjacent mantle. The rheologies of the mantle and slab represent instead the dominant effect. Second, under these assumptions the convergence rate of the island-arc system constitutes a major factor influencing the

stress distribution by means of the gravitational body forces and the mantle's resistance or support. The models indicate that a fine balance exists between these forces. Furthermore, if large deviatoric stresses are necessary for intermediate and deep earthquakes, the elevation of phase transformation boundaries are a necessary feature of the simulation for a mantle and slab with similar composition. The post-spinel phase change at the 650 km depth suggests itself as a possible factor in this mechanism. Finally, a low-strength channel corresponding to the seismic low-velocity zone and a stronger but constant-strength mantle yields reasonable agreement between the simulation and the regional stress patterns derived from earthquakes.

INTRODUCTION

New global tectonics implies both spreading of the sea floor and consumption of crustal plates into the mantle. Various geological and geophysical observations confirm the motion of these plates. Furthermore, they impose some constraints upon the general motion, both past and present. Yet the mechanism producing these motions is a topic of considerable debate. Gravitational sinking of the lithosphere, elevation of the mid-ocean ridges, and viscous drag have each been suggested as the mechanism coupling thermal convection to the lithosphere. One means of limiting the possible mechanisms causing the motion is to compute models of the stresses within a downgoing slab, incorporating various driving mechanisms and relevant body forces. Comparing the stress patterns, seismicity, energy, and focal mechanisms of earthquakes yield constraints upon the type of mechanism producing the plate motion. This technique has been used for just this purpose in this paper. Studies of the source mechanisms of shallow, intermediate and deep focus earthquakes have been conducted in most of the subduction regions. A comprehensive summary of the results are given by Isacks & Molnar (1971). Theoretical calculations of the stress distributions associated with a descending lithosphere have not kept up with the observational data. Using an analytical solution for the slab's thermal regime (McKenzie 1969) approached the problem of the stresses within the slab and

surrounding mantle. Griggs (1971) related the seismic effects to gravitational forces due to density anomalies arising from temperature differences and phase changes in an infinitely long slab.

In this paper we utilize a numerical scheme to approach the stress problem in the descending lithosphere. We model the descending slab and the surrounding mantle as an elastostatic problem, incorporating body forces due to thermal density differences between the colder slab and surrounding mantle. Symmetry of the ideal slab geometrically allows a plane strain formulation; consequently, the simulation reduces to an elliptic boundary value problem allowing numerical solution. Knowing the temperature regime within the slab (Toksöz et al. 1971), the induced stresses are then computed for elastic moduli selected to simulate the viscous and elastic support provided by the surrounding mantle. These models provide insight and restrictions upon the probable driving mechanism, and in conjunction with other data can improve our understanding of the motions of lithospheric plates.

In the following sections the theoretical assumptions and practical considerations required for these stress models are developed and the computational technique is described. The dependence of stresses upon the slab and mantle's rheology and their relationship to source mechanisms of earthquakes are discussed in the last section.

SIMULATION OF LITHOSPHERIC SLABS

The rheology of the earth represents a special problem for modeling the downgoing slab. The lithosphere and the mantle each exhibit different behavior to long-term stresses: the former acts nearly elastically (Walcott 1970), while the asthenosphere and probably the upper mantle approximate a fluid with a low yielding stress (Crittenden 1967). Consequently, a model of the descending lithosphere must incorporate the effects of these regions and the dynamic interaction of the system composed of the descending slab and asthenosphere. We model the lithosphere as an elastic model to reduce this to a tractable problem. We review the assumptions required for this formulation in the following sections.

Properties of Lithosphere and Descending Slab

Numerous data indicate that the lithosphere behaves elastically. It possesses a definite flexure rigidity (Walcott 1970) and displays phenomena such as bending at island arcs (Hanks 1970) which are attributed to its elasticity. Utsu (1967) and Davies & McKenzie (1969) have observed strong seismic-velocity anomalies at island arcs corresponding to a high velocity channel in the mantle. This appears to be a direct consequence of the colder lithosphere descending into the mantle (Minear & Toksöz 1970; Jacobs 1970). Furthermore,

the descending lithosphere attenuates seismic waves much less than the surrounding mantle (Utsu 1967; Molnar & Oliver 1969; Kanamori 1971, Mitronovas & Isacks 1971), again an indication of its elasticity. These and the observation of earthquakes support the assertion of an elastic lithosphere and its simulation as an elastic solid.

Yet it is not justified to assume constant elastic moduli throughout the slab, for it is not a constant temperature. The thermal gradient separating the core of the slab and the mantle must correspond to a change in the elastic moduli. Discussion of the temperature dependence will be postponed until a later section in order to first assess the behavior of the mantle.

Simulation of Mantle Properties

To treat the effects of the surrounding mantle with an elastic model, the mantle must be modeled as a 'soft' elastic solid capable of partially supporting the downgoing slab. The low yielding strength and the viscosity of the asthenosphere and the upper mantle have been deduced primarily from uplift data after glacial loading (Crittenden 1967; McConnell 1968; Cathles 1970). A low-viscosity channel of $10^{20 \pm 1}$ poise is generally agreed upon, while viscosities of 10^{23} poise are indicated for depths of 600 to 1200 km. Both experimental and theoretical results support the low creep strength of the upper

mantle (Carter & Ave'Lallemant 1970; Weertman 1970; Goetz 1971). Seismic attenuation (Anderson et al. 1967; Kanamori 1968), electrical conductivity (Everett & Hyndman 1968), and geothermal and melting information (Clark & Ringwood 1964) substantiate the marked differences bewteen the lithosphere and the asthenosphere which has been attributed to partial melting (Anderson & Sammis 1970). The upper mantle must then be approximated as a low-strength zone whose effect upon the lithosphere arises from both dynamic stresses and static support. The simulation must incorporate these two effects consistently with the geophysical observations.

For our calculations, the elastic constants are selected appropriate to the degree of support by the surrounding mantle. A rough guide can be had from the effective viscosities and elastic-viscoelastic analogy (Christensen 1971). Suppose one observes at an instant in time the stress distribution within the mantle and assumes that the stresses all originate dynamically from viscous drag. As the slab is moving at a constant velocity, a very rough assumption of constant strain rate, $\dot{\varepsilon}$, can be used with the effective viscosity η to define the resulting stress:

$$\sigma = \eta \cdot \dot{\varepsilon} \qquad (1)$$

This represents the supporting stress imposed upon the descending lithosphere within the limitations of a linear theory. The elastic moduli of the mantle region is adjusted to fit these approximate stresses to yield the corresponding support of the downgoing slab.

Figs. 4 to 10 display Young's modulus for the computed models as a function of depth. These models are selected to illustrate a range of mantle conditions: from constant elastic moduli throughout the mantle and slab to a very low-strength mantle relative to the slab. Intermediate cases having a 'soft' asthenosphere and 'hard' mantle offer closer approximations to the viscous models deduced by McConnell (1968). The relative importance of these factors can be judged from the resulting models.

Temperature Dependence of Elastic Moduli

One crucial factor remains for realistic simulation of the slab: the elastic constants are temperature dependent. The thermal effects upon elastic moduli for seismic frequencies are found to be $\frac{1}{E}\cdot\frac{\partial E}{\partial T} = -1.5 \times 10^{-4}/°C$ for olivine (Chung 1971), where E is an effective Young's modulus. But for long-term stresses this dependence is not realistic; a more appropriate relationship uses the rate of diffusion creep at high temperatures. For this form of creep an exponential dependence

of strain rate upon temperature is implied by theoretical and experimental evidence (Weertman 1970; Carter & Ave'Lallemant 1970):

$$\dot{\varepsilon} = f(\sigma)\exp(-Q/RT) \tag{2}$$

where Q is the activation energy for diffusion, R is the gas constant, T is the absolute temperature, and $f(\sigma)$ is a function that depends primarily on the stress but that may contain other variables. For constant load time Δt and stress σ, it follows that

$$E \simeq \sigma/\Delta\varepsilon \simeq \frac{\sigma}{\Delta t \cdot f(\sigma)}\exp(Q/RT) \simeq E_o\exp(Q/RT) \tag{3}$$

or to first order the dependence is

$$\frac{\Delta E}{E_o} \simeq -\frac{Q}{RT^2} \cdot \Delta T \tag{4}$$

Using approximate values for the parameters, a very rough upper bound results for the descending slab (Weertman 1970):

$$\frac{1}{E}\cdot\frac{\Delta E}{\Delta T} \simeq 2.2 \times 10^{-2}\ {}^{o}C^{-1} \tag{5}$$

when Q = 100 kcal., T = 1500 ^{o}C, and E is the value of Young's modulus. Figs. 5 to 7 give models incorporating a temperature dependence for the descending slab lying within the bounds of static (creep) and the high-frequency limits. These models provide a means of illustrating the marked effect that the slab's material strength has upon the resulting stress distribution; one expects the real earth to lie within this range.

COMPUTATION OF STRESSES

Simplifying the rheologies of the slab and mantle to effective elastic moduli allows solving an elastostatic problem instead of a difficult viscoelastic problem. With this in mind the representation of the descending lithosphere reduces to a plane strain, elastostatic problem adopting moduli corresponding to the mantle's support and using body forces based upon the slab's density anomalies. Assuming similar composition, the body forces originate from buoyancy due to the temperature difference between the slab and the adjacent mantle. A region within the colder slab is denser relative to the surrounding mantle; thus, it has a tendency to sink, thereby inducing stresses within the slab and mantle. These lateral density variations are

computed using the temperature regime obtained by Toksöz et al. (1971) for a slab with a spreading rate of 8 cm/yr. The value of volume expansion, σ, is derived from an average of Birch & Verhoogen's (Toksöz et al. 1971):

$$\alpha = \exp(3.58 - 0.0072z) \tag{6}$$

where z is depth in km. and α has units of $10^{-6}\ {}^{o}C^{-1}$. For average density ρ_o of the slab, the vertical body force F_y due to negative buoyancy becomes

$$F_y = g\rho_o\alpha\Delta T \tag{7}$$

where g is the acceleration of gravity, and ΔT is the horizontal temperature contrast between the mantle and the slab. Two separate values of the heat conduction have been used for the temperature calculations illustrated in Fig. 1 and 2. One set of models uses MacDonald's formulation of the radiative term (Toksöz et al. 1971), while the second set has a reduced radiative term derived from Schatz's (1971) experimental investigations for olivine. In the latter case the radiative conductivity is given by

$$K_R = 0 \quad \text{for } T \leq 500^{o}K, \text{ and}$$

$$K_R = 5.5\times10^{-6}(T-500.) \quad \text{for } T>500^{o}K \tag{8}$$

In addition the effect of the phase change is included in the body force as a separate problem. The depth and density changes of the olivine-spinel transition are estimated using Ringwood & Major's data (1970), and the elevation of the boundary is derived from the thermal regime in accordance with Toksöz's calculations. With the inclusion of these parameters, the problem reduces to an elliptic boundary value problem with variable coefficients.

A finite-difference scheme with a 20 km grid spacing has been used to solve this problem for an 840 by 680 km region enclosing the slab and adjacent mantle. The digital computer program has been developed for on-line solution of generalized elliptic boundary value problems by C. Tillman (1971) using a nine-point, integral formulation of the difference equations and successive point over-relaxation to obtain a solution. Utilization of this program has allowed solution of the equilibrium and constitutive equation for an inhomogeneous, isotropic body with infinitesimal deformation (Nowinski & Turski 1953):

$$\sigma_{\alpha\beta,\beta} = -F_\alpha(x_1,x_2) \qquad (\alpha,\beta = 1,2)$$

$$\sigma_{\alpha\beta} = \frac{\nu E(x_1,x_2)}{(1+\nu)(1-2\nu)}\,\delta_{\alpha\beta}\theta + \frac{E(x_1,x_2)}{2(1+\nu)}\,(u_{\alpha,\beta} + u_{\alpha,\beta}) \qquad (9)$$

$\theta = u_{\alpha,\alpha}$

$u_\alpha \equiv \alpha$ component of displacement

$\nu \equiv$ Poisson ratio $\qquad E(x_1,x_2) \equiv$ Young's modulus

Reducing these to the divergence form in terms of displacements, one has a set of coupled equations:

$$\frac{\partial}{\partial x}\left[\frac{(1-\nu)E(x,y)}{(1+\nu)(1-2\nu)}u_{x,x} + \frac{\nu E(x,y)}{(1+\nu)(1-2\nu)}u_{y,y}\right] + \frac{\partial}{\partial y}\left[\frac{E(x,y)}{2(1+\nu)}(u_{x,y}+u_{y,x})\right] = -F_x = 0$$

$$\frac{\partial}{\partial x}\left[\frac{E(x,y)}{2(1+\nu)}(u_{x,y}+u_{y,x})\right] + \frac{\partial}{\partial y}\left[\frac{E(x,y)}{(1+\nu)(1-2\nu)}u_{x,x} + \frac{(1-\nu)E(x,y)}{(1+\nu)(1-2\nu)}u_{y,y}\right] = -F_y(x,y) \tag{10}$$

where $F_\alpha \equiv \alpha$ component of body force,

$$\frac{\partial u_i}{\partial x_j} = u_{i,j}\ , \text{ or } \frac{\partial u_x}{\partial y} = u_{x,y}\ , \text{ etc.}$$

The spatial variations of body forces and elastic parameters are introduced and a solution follows from the difference

scheme with the appropriate boundary conditions.

If the boundaries surrounding the slice of mantle are far enough from the slab, their effect upon the descending lithosphere will be minimal. This corresponds to St. Vincent's principle in elastostatics. The two extreme cases are a rigid boundary (no displacements) and a free surface (no tractions). For the side boundaries, the computations indicate minimal effect of the boundaries upon the stress distribution within the descending slab. Our previous arguments for a relatively soft mantle suggest small tractions at the side boundaries; hence, these have been selected for our computations. The top face, corresponding to the earth's surface, is also specified as free, whereas the bottom face is made rigid. This lower boundary is necessary to satisfy the requirements for a static problem: the sum of all couples and forces must be zero for the region. Again the boundary does not seriously effect the stresses within the slab. In addition, some models have the edges of the lithosphere rigid to simulate the junction of the descending slab and the crustal plate. Yet due to the limitations of these boundary conditions, the lack of information for the lithosphere as it bends into the mantle, and the characteristics of the plate boundaries, these models cannot hope to indicate the stresses for depths less than about 100 km, and that is not their intent. Rather, the

intermediate and deep regions of the downgoing slab are within the realistic domain of the models.

Stability and convergence of the solution is ensured by both test problems and on-line inspection of convergence. The program has successfully solved a variety of problems including potential flow, bending of plates, and others (Tillman 1971). This series has confirmed the utility and stability of the difference scheme. In addition, inhomogeneous, plane strain elastic solutions confirm the stability for problems such as the descending slab (appendix). The 20 km grid spacing used for the slab is adequate for the broad features encountered in the thermal regime and for the desired resolution of the stress distribution. Finally, on-line monitoring and selection of the relaxation parameters provides for optimum convergence and continual inspection of stability (Mitchell 1969).

RESULTS OF SIMULATION

Theoretical Results

A set of eight models simulating different rheologies and conditions are summarized in Table 1 together with the important parameters and results. Figs. 3 through 10 display these models including the mantle and slab's elastic

moduli, each figure depicting the variation of a particular parameter. The differences between the two thermal regimes in Fig 1 and 2 are not the controlling factor in these models; the reduced radiative conductivity increases the gravitational body force and density gradient, yet this is a minute effect compared to the changes in mantle support and slab rheology. The mantle and slab properties control the behavior of the stress pattern: the maximum shear stress concentrates within the colder, harder core for a slab with temperature dependent elastic parameters. Decreasing the mantle's total and distributed support alters the principle stress from compression downgoing to tension along the trend of the slab. These relationships will be clarified in the following discussion of the individual models.

Comparison of Models

A simulation is first necessary for a control case, specifically, a model having identical elastic moduli within the mantle and slab. Model 1 in Fig. 3 represents such a case. For this case the maximum shear stress occurs at the lower edge of the slab and within the adjacent mantle, whose stresses have not been contoured. The orientation and the maximum stress reflect the distribution of body forces; at the lower edge and within the adjacent mantle, the compressional axis is vertical as one expects from simple static

consideration. The distribution of body forces also introduces downdip tension for shallow depths. Given this example, the succeeding models illustrate the marked effects produced by different effective rheologies within the slab and mantle.

Models 2 and 3 in Fig. 4 represent slabs with constant properties and different surrounding mantle conditions. The slab can be thought of as a bending plate with different degrees of support along its length. In model 2 the mantle differs little from the slab, and only a small reduction in strength occurs in the asthenosphere. The slab is relatively immobile in the deep mantle, whereas the asthenosphere allows 'sagging' analogous to a plate held at its edges: compression along the top face and tension along the bottom. If the asthenosphere is 'softer' as in model 3, the slab almost hangs as though suspended by the lithosphere and only partially supported at its base. Compression then occurs at the bottom face of the slab and tension along its upper surface. Decreasing the mantle's support also increases the stress guided through the slab. Yet the shear stresses are concentrated at the edges of the slab as one expects for a bending plate but not necessarily for the descending lithosphere.

An alternate set of models is desired which concentrates the shear stress towards the slab's center; models 4 and 5 in

Fig. 5 show such a transition. The slab's strength is strongly dependent upon temperature according to equation (3) with a pressure term included:

$$E \propto \exp\left(\frac{Q + pV_{ac}}{RT}\right), \quad \text{or for } V_{ac} = 0,$$

$$E_{slab} = 5.0 \times 10^{10} \exp(-0.36 \times 10^{-2} \Delta T) + E_{mantle} \qquad (11)$$

where p is the pressure in kilobars, and V_{ac} is the activation volume for diffusion creep (Weertman 1970). The stresses are now strongly focused within the colder regions of the slab as expected from diffusion creep. In addition, two extreme cases of mantle support are illustrated: one having the tensional or minimal principle axis following the trend of the slab along its full length, the other with the compressional axis paralleling the slab. The downgoing slab in model 5 hangs from the lithosphere. With increasing strength and support by the mantle, the slab can be placed under compression as in model 4. A balance then exists between the mantle's support, the slab's strength, and the distribution of density anomalies within the slab. The next set of models clarifies this balance between the mantle's and the slab's rheology.

Suppose the strength of the slab is only weakly dependent upon temperature as given by:

$$E_{slab} = E_{mantle} + 5.0x10^{10}\left[1 - \frac{(100. + 0.895p)\Delta T}{2(T_{mantle})^2 x10^{-3}}\right] \quad (12)$$

Model 6 in Fig. 6 simulates such a condition for a mantle with a low-strength channel similar to model 4. Its stress distribution is an intermediate case between the downdip compression of model 4 and the bending stresses that are characteristic of model 2; however, the temperature dependence of the elastic moduli is insufficient to focus the stress towards the center of the slab. As in model 4 the narrow asthenosphere prevents tension along the slab's full length. Model 7 is similar to model 6 but has no temperature dependence for the descending lithosphere. As expected, its maximum shear stress concentrates at the edges of the slab; however, the soft asthenosphere introduces tensional features at intermediate depths. The models suggest that a critical value for the temperature dependence may be necessary in order to focus the stress within the slab.

On the other hand, increasing the contrast of the elastic moduli within the slab strongly focuses the stress and can induce tension at intermediate depths. Fig. 7 illustrates this case with model 8 for a temperature dependence given by

$$E_{slab} = E_{mantle} \exp[\, -(1.2\times10^{-2} + 5.5\times10^{-5} p)\,\Delta T] \qquad (13)$$

A very soft asthenosphere combined with a hard central core for the slab produce high shear stresses with the tensional axis following the slab at intermediate depths and with downdip compression for greater depths.

Three parameters are resolved that best described these categories. The first measures the ratio of mantle strength at two depths, 140 and 440 km, thereby resolving the differential support of the asthenosphere and the deeper mantle. Yet this is incomplete without a measure of the contrast between the mantle and the slab, as given by the ratio of their elastic constants at 460 km depth. The final parameter measures the temperature dependence of the slab's elastic moduli. It is the ratio of moduli at its edge compared to its center at 160 km depth. Fig. 8 gives a three dimensional perspective of these models in terms of the parameters. The categories are representative of the model space spanned by this series of computations. Thus, regions are blocked off depending upon the models locations and characteristics. The boundaries are merely to illustrate the regional dependence and should only be interpreted as guidelines.

Phase Changes and Convection

Fig. 9 considers the elevation effect of the olivine-spinel phase change within the slab (Schubert & Turcotte 1971). Using Ringwood & Major's (1970) estimation of the slope for the phase transformation boundary, 30 bar/^{o}C. the density anomalies within the slab are computed using Fig. 1 when the transition occurs over 50 km (Toksöz et al. 1971). The problem then lends itself to superposition: calculating the solution independently and summing the stresses for the separate models. The transition induces local stress concentrations directly above and below the perturbed depth. The slab tends to be under tension at or above 350 km and in compression below this depth. Consequently, if the slab is originally under compression at 350 km, the transition reduces the maximum shear stress above that region while increasing it below the phase change.

In the same manner the convection problem in Fig. 10 is treated as a slab with boundary tractions along its faces. The right-hand problem does not include the mantle's support; instead, the slab acts as a free plate with applied tractions. The figure illustrates an example using 50 bars resistance along the slab's upper surface and no tractions along its bottom face. This roughly simulates convection along the bottom face and viscous drag on the top. As expected for a plate, bending effects are superimposed upon the dominate

horizontal principle stress. The left-hand model with mantle support incorporates a shear couple along the upper, mantle-slab boundary to simulate drag. The stress orientations are now more complicated due to the mantle support. Yet the models reveal that such convection generally increases compression along the trend of the slab.

Comparison to Island Arcs

Isacks & Molnar (1971) have summarized the observed stress patterns for island-arc regions and their relationship to the regional tectonics and gravitational sinking of the descending lithosphere. Fig. 11 gives their interpretation of the principle stresses derived from focal-mechanism solutions. Three crucial regions are apparent in the stress pattern and the numerical models: at shallow depths the tensional principal stress, T, parallels the slab's orientation; intermediate orientations, B, or down-dip extension occurs at intermediate depths; and down-dip compression, P, dominates for greater depths. The following sections will show the correspondence between the computed models and the regional stress distribution, and in addition, will corroborate the sinking lithosphere hypothesis. Regions have been selected as representative of island-arc systems and for adequate knowledge of the arc, a prerequisite for discriminating the crucial elements of the mechanism. Unless referenced to

the contrary, the seismicity and the focal-mechanism solutions are contained in Isacks & Molnar (1971).

Honshu

The dipping slab beneath North Honshu and the Sea of Japan closely resembles model 4: a 30 degree dipping slab under compression for depths greater than 80 km. The seismic activity is continuous and does not extend much beyond 600 km in depth. Concentrating upon the relatively uncontorted central region, compression is preferred for the majority of solutions. Closer inspection of the data reveals a slight rotation towards down-dip tension of the P axis with decreasing depth, yet nothing that can be termed definitive. Kanamori's (1971) solution of the Sanriku earthquake of 1933 has down-dip extension and is located near the trench axis. Only for shallow depths, then, is the slab under tension; the bulk remains under down-dip compression as attested by the focal-mechanism solutions.

Comparing these orientations to those of model 4 in Fig. 5, the principle stress is also down-dip compression for intermediate and greater depths. The simulation implies that a narrow, low-strength asthenosphere can exist if sufficient support is provided by the metasphere. In addition, the model suggests rotation of the stress orientations for intermediate depths. The nature of these rotations cannot be

determined on the basis of a two-dimensional simulation of the real earth. Moreover, Kanamori's (1971) tensional solution for the Sanriku earthquake demonstrates that the simulation is not fully satisfactory; the theoretical model is still compressional for shallow depths. This effect has its origin from either of two related factors: the slab's core is insufficiently 'hard', or its corrolary, the mantle is supporting an excessive fraction of the slab's body force. The major factor, however, could be the rigid boundary at the edge of the lithosphere. It, in effect, simulates the lithosphere pushing the descending slab. Consequently, a simulation having parameters intermediate to models 4 and 8 is necessary for extension at shallow depths.

Tonga

The marked similarity between Tonga and Honshu in Fig. 11 dictates a corresponding interpretation of the models; both involve support by the mesosphere and a soft asthenosphere as suggested by Isacks & Molnar (1969). Both convergence rates are approximately 9 cm per year (Le Pichon 1968) implying greater density anomalies and depth before equilibrium (Minear & Toksöz 1970), higher strength within the colder slab, alterations of phase boundaries, and perhaps greater resistance or drag by the mantle. Their interrelationship clarifies itself when additional regions are examined.

Kermadec

The Kermadec arc, lying just south of Tonga, represents a marked change in the stress distribution. The inclined zone parallels a slab dipping 60 degrees west and extends to 500 or 550 km depth (Sykes 1966). Limited focal plane solutions show down-dip extension at 230 km depth and compression for 350 km. The region corresponds, then, to model 8 in Fig. 7, if the mantle support is further reduced to allow extension at 230 km depth. Thus in Fig. 8 the regions are evolving towards decreasing mantle support. Moreover, the convergence rate at the Kermadec arc is markedly less than the preceeding two cases, 5.4 cm/yr as opposed to 9 cm/yr.

South America

Peru and Northern Chilean regions carry this deduction one step further: a gap in seismicity exists between intermediate depth, extensional earthquake mechanisms and compressional mechanisms at 600 km. Briefly, the shallow or intermediate zone is characterized by down-dip tension for a shallow dipping slab; however, no conclusive seismic activity occurs between 200 or 300 km and 500 km for Peru and Chile, respectively. Between 500 and 600 km the seismic activity dramatically increases, and the mechanisms indicate down-dip compression. Whether the slab is continuous through the

seismicity gap remains a conjecture. In Chile high-frequency shear waves pass through the gap, while the results are inconclusive for Peru and western Brazil (Molnar & Oliver 1969; Sacks 1969). Either the zone of attenuation in the mantle occurs above the gap, or the descending lithosphere is continuous to depths of 650 km.

Assuming the slab is continuous, the seismicity and focal mechanisms could follow from the dynamics of gravitational sinking. The North Chilean slab extends 200 km deeper than Kermadec, but the convergence rate is similar, 5.2 cm/yr (Le Pichon 1968). The additional length of slab has two opposing effects: the total body force is increased by the added segment and by the contribution of any deep phase changes within the slab. Yet deeper penetration of the slab and variations in the mantle's resistance or support opposes the increased body force. An extrapolation of model 8, which has tension at intermediate depths, could produce such a gap given the proper combination of mantle and slab support, body forces, and perhaps elevation of phase-transformation boundaries. The additional length of slab increases the total body force and offsets any mantle support gained by greater penetration. A balance must exist between the body force, mantle resistance, and depth of penetration for the occurrence of this pattern. For Kermadec and Chilean slabs, the resistance or support at each depth is held constant by similar convergence rates; consequently, the effects caused by the additional length of slab are present given that

their preceding history is inconsequential. The latter assumption is questionable. Otherwise, if the slab is continuous and if the convergence rate has been reasonably stable over the past 10 million years, it is an adequate proposition.

Other evidence from South America suggests that the slab behaves as a stress guide for both shallow and deep earthquakes. Carr et al. (1971) reported evidence of lithospheric bending for shallow depths: tensional earthquakes near the surface and down-dip compression along the bottom face. This cannot be attributed to thrusting of one lithospheric plate under another. The Kurile arc also shows compression for shallow depths at the lower face. For greater depths Fukao (1971) has obtained the solution for a deep-focus earthquake (577 km) in western Brazil including the fault plane parameters. It verifies shear faulting for deep earthquakes and indicates that the P axis is nearly vertical, corresponding to the trend of the slab. The stress drop, 300 to 460 bars, implies that the compressional principle stress is greater than 600 to 920 bars. Moreover, the faulted area, 510 to 580 km^2, the average dislocation, 265 to 355 cm, and the location of subsequent earthquakes suggests large-scale faulting over nearly the entire thickness of the descending lithosphere. These observations are consistent with gravitational sinking as the mechanism inducing earthquakes within the descending lithosphere.

Middle America and the Aleutians

The Middle American arc corresponds to a short slab dipping about 40 to 60 degrees at depths greater than 85 km. Focal-mechanism solutions are consistent with down-dip extension along its 200 to 300 km length. Thus, the arc resembles model 5 with minimal support from the surrounding mantle.

The Aleutian arc also conforms to a shallow-slab representation with a dip of approximately 60 degrees (Davies & McKenzie 1969) and with seismicity generally less than 200 to 300 km deep. Unlike the Middle American arc, compressional solutions are evident for intermediate depths, while down-dip tension occurs for shallow depths adjacent to the trench (Stauder 1968a,b). The arc could illustrate a truncated version of model 8, similar perhaps to model 7; however, the factors that determine the individuality of the Aleutians and Middle American arcs remain obscure. Conceivably, the distinctive stress distributions result from the increased convergence rate of the Aleutian arc, 5.2 cm/yr (Le Pichon 1968) compared to roughly 3.5 cm/yr for Middle America (Molnar & Sykes 1969), thereby augmenting the thermal body forces and the mantle resistance and placing the slab under partial compression. These convergence rates are, however, questionable.

Kurile-Kamchatka

The Kurile-Kamchatka arc, dipping at 45 degrees, poses a crucial validation of these mechanisms. Contrary to the other island arcs, the seismicity suggests the maximum depth of the zone is probably less than 600 km and perhaps nearer 500 km. Yet the convergence rate is approximately 7.5 cm/yr (Le Pichon 1969). Based upon the proposed mechanism, one would expect a distribution similar to Kermadec with its 500 km slab but with additional body forces and mantle resistance generated by the faster convergence rate. Indeed, the effect is apparent in the stress distribution: a minimum in activity, and not an aseismic gap, is reported between about 200 and 400 km. The shallow events above the gap exhibit down-dip extension, whereas for events located beneath the gap the stress orientation is down-dip compression. Moreover, rotation of the principle axis occurs for events near the periphery of each region just as in model 8. These characteristics place the arc as an intermediate case between Kermadec and Tonga, and substantiate the idea that the descent velocity of the lithosphere plays a major role in the dynamics and manifests itself in the seismicity and stress orientations by means of the body force and mantle resistance.

DISCUSSION AND IMPLICATIONS - A MODEL OF DESCENDING LITHOSPHERE

The results discussed in the previous section suggest a simple, semi-empirical analogue to explain the regional stress patterns observed for island arcs. When the earthquake characteristics, the limiting depth of down-dip tension and compression, are plotted in terms of the convergence rate, a relationship appears between the seismicity, focal mechanisms, and the convergence rate. Fig. 12 illustrates this pattern in addition to a theoretical model. Beginning with New Zealand and slow convergence rates, a large seismicity gap occurs between down-dip tensional solutions and deep compressional solutions. For faster convergence rates with a deep slab, the zone narrows and then disappears for the Kurile island arc, yet a minimum in seismicity persists between 200 and 400 km in addition to fluctuations in the stress orientations. Tonga also displays a minimum within this range. The second figure indicates an analogous pattern for steeply-dipping slabs. Indeed, the relationship can be deduced from gravitational sinking of the descending lithosphere if a continuous slab is presupposed.

A simulation of gravitational sinking suggests the dependence of the stress distribution upon the body force and the mantle resistance via the convergence rate. Postulating the dependence of body forces and mantle support upon the

convergence rate of the island arc, and assuming the depth dependence for the support and phase changes, a numerical integration of the forces along the slab yields the stress within the slab as a function of convergence rate, length of slab, and dip. The stresses are only those along the direction of the slab and indicate whether tension or compression prevail. Fig. 14 portrays a numerical solution given the following assumptions: first, the body force due to thermal contraction is constant along the slab and varies as the square root of the rate. It has been normalized to yield 140 dynes/cm^3 at 8 cm/yr; the precise value does not affect the solution. The rate function roughly corresponds to the models of Minear & Toksöz (1970) and equals the rate of conduction for an infinite body with initial temperature distribution (Carslaw & Jaeger 1958). Alterations of the phase boundaries are also given this rate dependence when normalized to 8 cm/yr boundaries calculated by Toksöz et al. (1971). Viscous drag is now assumed for the support or resistance; thus, resistance is linearly dependent upon the rate. In addition, the resistance at its end is 2 to 5 times greater than at the faces. Increasing tension with decreasing convergence rate as in Fig. 12 suggests that resistance must decrease faster than the total body force if the slab is continuous through the aseismic gap. The dependence, controlled by mantle rheology, is then selected

to yield the desired distribution. Finally, the resistance is normalized at 10 cm/yr to obtain compression throughout the slab. To compute steeply dipping slabs, only the component of body force along the dip is altered, while other factors such as greater temperature contrasts remain constant. Restrictions upon the length of the downgoing slab and the convergence rate have not been imposed and are not necessary in this analogue (Luyendyk 1970). Table 2 summarizes the parameters and solution for one successful model.

Certain observations are in order regarding the characteristics of successful models: if stresses greater than 1 kilobar are deemed necessary (Wyss 1970; Fukao 1971) and if compositional differences are insignificant, the additional body force provided by elevated phase boundaries is a prerequisite. Alone, body forces from thermal contraction are insufficient to cause the seismicity and the large apparent stresses observed, particularly at great depths in South America. Perhaps the deep seismicity, maximum at 600 km reflects a change in the material properties of the slab as could occur in the post-spinel phase change. Only the depth of the phase change must decrease within the slab. A positive slope of dP/dT for the post-spinel phase transformation would imply both higher body forces and a change in physical properties at 600 km.

The analogues also employ a low-strength asthenosphere extending to 220 km; however, little or no increase in resistance is demanded for greater depths. This is in accord with a recent solution of glacial uplift data (Cathles 1971), but directly contradicts models of gravitational sinking relying upon monotonic increasing strength with depth along the length of the slab (Isacks & Molnar 1969, 1971).

Assuming a continuous slab for all seismic zones entails no presuppositions for the mechanism of separation. Instead, the aseismic gap stems from its low stress. Neither hypothesis subjects the deeper portions to stress; both must rely upon forces adjacent to and within the deep slab as the mechanism inducing deep earthquakes in South America and similar locales.

Fig. 13 further corroborates the model's relationship to seismicity. A distinct correlation appears between the regional seismicity and the stress levels within the hypothetical slab. Only the relative shapes of the curves are significant; the actual magnitude of stress within the slab depends upon the precise model. Underthrusting of lithospheric plates also contributes to shallow seismicity, and variations in the material properties of the slab may be important for all depths.

Finally, the models readily explain the pattern for

steeply dipping slabs: the greater down-dip component of the body force pulls the zone of tension further down the slab. Yet constant resistance along the length of the slab and localized body forces from phase transitions allow compression even for short slabs. This emphasizes the importance of these phase transformations upon the proposed slab dynamics.

CONCLUSIONS

Summary

Gravitational sinking induced by thermal density anomalies can explain the directions of the principle stress within the descending slab at island arcs without recourse to significant convective effects in the adjacent mantle. Rather, the rheologies of the mantle and slab are the dominant factors influencing the stress pattern. Earthquake source mechanisms together with the models indicate that the temperature dependence of the slab's material properties is significant; bending effects that are characteristic of a plate are only observed for shallow depths. Instead, the stress is transmitted predominately down-dip within the slab. A low-strength asthenosphere or channel below the lithosphere is also consistent with the models and with the regional earthquake mechanisms. These are in agreement with Isacks &

Molnar (1971).

Numerical integration for a simple model containing the relevant forces and their assumptions suggests a hypothesis for the dynamics of subduction. An essential element is the dependence upon the velocity of the converging lithospheric plates; it represents a major influence upon the dynamics of descent. The thermal body forces, boundaries of phase changes, and elastic constants are manifestations of the convergence rate. Yet a crucial dependence results between the mantle's support or resistance and the velocity in order to account for the regional distribution of earthquakes: the resistance increases with faster convergence rates. The viscous end-resistance may also be more important than hitherto acknowledged. Finally, increasing strength with depth in the mantle is not a prerequisite for simulating the regional stress distribution. A low-strength channel corresponding to the seismic low-velocity zone and a stronger but constant strength mantle yields reasonable agreement between the models and the regional stress patterns derived from earthquakes. If the mantle and slab have significantly different compositions, the simulations are no longer valid.

In addition, the contribution of phase changes is predicted as a crucial element of the hypothesis given the large apparent stresses observed for intermediate and deep

earthquakes and the initial assumptions for the models. The hypothesis is then consistent with a form of shear faulting as the dominant source mechanism for these earthquakes. The simple models suggest further that the post-spinel phase change at 650 km could provide a mechanism needed to induce deep earthquakes, given a positive slope for dP/dT at the phase boundary. Otherwise, the high stresses proposed for deep earthquakes are probably inconsistent with the hypothesis.

The computational results of this paper rely upon a variety of theoretical and experimental inferences that require further research.

Acknowledgments

The research has been supported by the Advanced Research Projects Agency monitored by the Air Force Office of Scientific Research through contract F44620-71-C-0049, NASA grant NGL 22-009-187, and NSF grant GA-29358.
One of the authors (Albert T. Smith, Jr.) has been supported by a Hertz Foundation Fellowship during part of this work.
We gratefully acknowledge many helpful suggestions made by Norman Sleep and Jorge Mendiguren.

Appendix

FORMULATION OF FINITE-DIFFERENCE EQUATIONS

The finite-difference approximation for equation (10) within the digital program (Tillman 1971) uses the self-adjunct form of the elliptic equations together with an integral formulation for the difference equations (Varga 1962). A complete development may be found in the references; however, we will review the formulation for the elastostatic problem.

The self-adjunct, elliptic boundary value problem has the form

$$\frac{d}{dx}\left(\underline{A}\frac{du}{dx} + \underline{B}\frac{du}{dy} + \underline{C}u\right) + \frac{d}{dy}\left(\underline{D}\frac{du}{dx} + \underline{E}\frac{du}{dy} + \underline{F}u\right) + \underline{G}u = H \tag{A-1}$$

where $\underline{x}$ and $\underline{y}$ are the independent variables, $u = (u_1, u_2, \ldots u_N)$ is the set of unknown functions to be determined, and $A = (\underline{a}_{kl})$, $\underline{B} = (\underline{b}_{kl})$, ..., $G = (\underline{g}_{kl})$ and $\underline{H} = (\underline{h}_k)$, k, l = 1, 1, ...N, are specified matrices whose components may vary with $\underline{x}$ and $\underline{y}$. The integral formulation of equation (A-1) reduces to an area integral over any subregion (Varga 1962; Tillman 1971):

$$\iint_R \left[\frac{d}{dx}\left(\underline{A}\frac{du}{dx} + \underline{B}\frac{du}{dy} + \underline{C}u\right) + \frac{d}{dy}\left(\underline{D}\frac{du}{dx} + \underline{E}\frac{du}{dy} + \underline{F}u\right)\right]dxdy$$

$$+ \iint_R \underline{G}u\,dxdy = \iint_R \underline{H}\,dxdy \qquad \text{(A-2)}$$

On application of Gauss's theorem, this becomes

$$\oint_\Sigma \left[-\left(\underline{A}\frac{du}{dx} + \underline{B}\frac{du}{dy} + \underline{C}u\right)dy + \left(\underline{D}\frac{du}{dx} + \underline{E}\frac{du}{dy} + \underline{F}u\right)dx\right]$$

$$+ \iint_R \underline{G}u\,dxdy = \iint_R \underline{H}\,dxdy \qquad \text{(A-3)}$$

where the boundary Σ of subregion R is traced in the clockwise direction.

For the elastostatic equations, the formulation reduces to a set of difference equations for a uniform orthogonal lattice with grid lines parallel to the $\underline{x}$,$\underline{y}$ axes and separated by a distance $\underline{h}$. The interior node, N_o, is surrounded by 8 adjacent nodes, each numbered consecutively starting at the $\underline{x}$ axis and working clockwise. In this case the set of interior difference equations at an interior node N_o becomes:

$$\sum_{k=1}^{8}\{ -[\underline{A}\delta(\frac{du}{dx}) + \underline{B}\delta(\frac{du}{dy})]_{S_k}\Delta y_k$$

$$+ [\underline{D}\delta(\frac{du}{dx}) + \underline{E}\delta(\frac{du}{dy})]_{S_k}\Delta x_k\} \qquad (A\text{-}4)$$

$$= \sum_{k=1}^{8} \underline{H}_{T_k}\Delta a_k$$

where $\delta(z)$ is a difference approximation to $\underline{z}$. Thus, $\delta(\frac{du}{dx})$ is a vector approximation to $\frac{du}{dx}$ in terms of the approximations to the dependent variables $\underline{u} = (u_1, u_2)$ at node N_o and its neighbors $N_1, N_2 \ldots, N_8$. The summation is along the boundary Σ of the subregion. This subregion is a square centered upon the interior node N_o and with side $\underline{h}$. The subregion may be further subdivided into 8 equal right triangles, t_k, all having a vertex in common at the interior node N_o. $s_1, \ldots s_8$ denotes the boundary of subregion starting at the $\underline{x}$ axis and continuing clockwise, and Δy_k, Δx_k is the length of the segment s_k in the $\underline{x}$ and $\underline{y}$ directions. S_k indicates that the matrix or difference approximation is evaluated at the midpoint of segment s_k, and $\underline{T}_k$ requires evaluation at the centroid of the triangular subregion t_k. The evaluation of the governing system of matrices $\underline{A}$, $\underline{B}, \ldots, \underline{H}$ and the approximation $\delta(\frac{du}{dx})$, etc., are accomplished by a bilinear interpolation from the values at the surrounding nodes. Thus,

evaluation for the midpoint of segment s_1 requires a linear interpolation using nodes N_o, N_1, N_2, and N_3. The formulation results then in a nine-point difference approximation to equation (10) for the displacement field. The matrices for equation (A-4) become

$$\underline{A} = \begin{bmatrix} \frac{(1-\nu)E(x,y)}{(1+\nu)(1-2\nu)} & 0 \\ 0 & \frac{E(x,y)}{2(1+\nu)} \end{bmatrix}$$

$$\underline{B} = \begin{bmatrix} 0 & \frac{\nu E(x,y)}{(1+\nu)(1-2\nu)} \\ \frac{E(x,y)}{2(1+\nu)} & 0 \end{bmatrix}$$

$$\underline{D} = \begin{bmatrix} 0 & \frac{E(x,y)}{2(1+\nu)} \\ \frac{E(x,y)}{(1+\nu)(1-2\nu)} & 0 \end{bmatrix} \qquad \text{(A-5)}$$

$$\underline{E} = \begin{bmatrix} \frac{E(x,y)}{2(1+\nu)} & 0 \\ 0 & \frac{(1-\nu)E(x,y)}{(1+\nu)(1-2\nu)} \end{bmatrix}$$

$$\underline{H} = \begin{pmatrix} 0 \\ \\ -F_y(x,y) \end{pmatrix} \tag{A-5}$$

E(x,y) represents the spatially varying Young's modulus, and $F_y(x,y)$ is the gravitational body force. Using the finite-difference approximation to the coupled equations, a solution may be obtained using successive over-or-under-relaxation.

The finite-difference equations must be represented in matrix form

$$\underline{AU} = \underline{B} \tag{A-6}$$

where A and B are a coefficient matrix and inhomogeneity vector, respectively, produced by means of the integration technique. The vector of approximations to the nodal values of the dependent variables $\underline{u}$, is determined by successive over-relaxation. For a problem with N dependent variables, each node has a set of N equations which are ordered successively in (A-6) according to the grid numbering. Correspondingly, the unknown vector $\underline{U}$ of the system is formed by stacking sets of nodal approximations $\underline{u}_p = (u_1, u_2)_p$ end-on-end in the order of the numbering. Thus for a lattice with M nodes, the vector $\underline{U}$ of (A-6) would have MN

components while A would be a square, MN by MN, coefficient matrix, and $\underline{B}$ an inhomogeneity vector with MN components. The solution is then obtained using the method of successive point over- or under-relaxation (Varga 1962).

The solution of the general plane elastostatic problem given by equation (A-4) and (A-5) requires theorems for stability and convergence of coupled elliptic equations with variable coefficients. Since these are not available, we must depend upon empirical tests of convergence (Mitchell 1969).

Mild restrictions are, however, imposed by the integration technique (Varga 1962; Tillman 1971):

(1) dependent variables $\underline{u} = (\underline{u}_1, \ldots, \underline{u}_n)$ must be continuous functions of x and y;

(2) all coefficients of the equations must be piecewise continuous;

(3) there must be flux continuity in any direction and at any point of the region.

Flux continuity is actually a property imposed upon the solution u by the integration technique and guarantees that proper interface conditions are formulated along lines of material discontinuities without special attention (Varga 1962).

Convergence towards a true, discrete solution using successive over-relaxation depends upon the properties of the

coefficient matrix, which in turn depends on the particular differential system and finite-difference lattice under consideration. Successive relaxation will converge for any relaxation factor ω in the range $0<\omega<2$. If matrix $\underline{A}$ is symmetric, nonsingular, and positive definite, and further, convergence will occur for $\omega = 1$ (Gauss-Seidel method) if $\underline{A}$ is strictly or irreducibly diagonally dominant (Varga 1962). The last condition is satisfied; however, showing that matrix A possesses the other properties is a difficult task, particularly for variable coefficients. One must then rely upon empirical tests to evaluate the convergence.

Tillman (1971) describes several sample problems successfully solved by the program. These include conduction problems, simple plane stress, potential flow, and linear and nonlinear plate bending, including irregular lattice structures. Comparison to exact solutions available for some problems indicates insignificant errors; the final answers are within a few percent of the theoretical.

Fig. 14 depicts the numerical solution for a plane strain problem with variable elastic moduli. A square with 11 grid points to the side is taken for the region, and Young's moduli is made to vary along the y-axis. A rigid boundary is placed along the left-hand face; free sides are

specified; and 25 dynes/cm^2 outward traction is imposed by means of body forces upon the right-hand face. Thus the square is under tension. The exact solution along the axis of the square corresponds within 6% to the numerical results for $\omega = 1.5$ and after 150 iterations. The problem indicates that on-line monitoring can provide an accurate evaluation of the convergence.

For general solutions, empirical evaluation must be relied upon to determine convergence, for it does not necessarily occur for all values of the relaxation parameter. Yet on-line tests for different parameters furnish a reliable appraisal of the convergence; both convergence to a discrete solution and the optimum rate may be evaluated. This technique has proven the surest means of guaranteeing stability and convergence for the problems.

Anderson, D.L., 1967. Latest information from seismic observations, in The Earth's Mantle, ed. by T.F. Gaskell, Academic Press, London.

Anderson, D.L. & Sammis, C., 1970. Partial melting in the upper mantle, Phys. Earth Planet. Int., 3, 41-50.

Carr, M.J., Stoiber, R.E. & Drake, C.L., 1971. A model of upper mantle structure below Japan, Trans. Am. Geophys. Un., 52, 279 (abstract).

Carslaw, H.S. & Jaeger, J.C., 1959. Conduction of heat in solids, Oxford, London.

Carter, N.L. & Ave'Lallemant, H.G., 1970. High temperature flow of dunite and peridotite, Bull. geol. Soc. Am., 81, 2181-2202.

Cathles, L.M., 1971. Lower mantle viscosity inferred from post glacial adjustment of the ocean basins and Canada, Trans. Am. Geophys. Un., 52, 353 (abstract).

Christensen, R.M., 1971. Theory of viscoelasticity, an introduction, Academic Press, New York.

Chung, D.H., 1971. Elasticity and equations of state of olivines in the Mg_2SiO_4-Fe_2SiO_4 system, Geophys. J. R. astr. Soc., in press.

Clark, S.P. & Ringwood, A.E., 1964. Density distribution and constitution of the mantle, Rev. Geophys., 2 35-88.

Crittenden, M.D., Jr., 1967. Viscosity and finite strength of the mantle as determined from water and ice loads, Geophys. J. R. astr. Soc., 14, 261-279.

Davies, D. & McKenzie, D.P., 1969. Seismic travel-time residuals and plates, Geophys. J. R. astr. Soc., 18, 51-63.

Everett, J.E. & Hyndman, R.D., 1968. Geomagnetic variations and electrical conductivity structure in south-western Australia, Phys. Earth Planet Int., 1, 24-34.

Fukao, Y., 1971. Focal process of a large deep-focus earthquake as inferred from long-period P waves, the Western Brazil Earthquake of 1963, Sc.D. Thesis, Earthquake Research Institute, University of Tokyo.

Goetze, C., 1971. High temperature rheology of Westerly Granite, J. geophys. Res., 76, 1223-1230.

Griggs, D.T., 1972. The sinking lithosphere and the focal mechanism of deep earthquakes, Proc. of the meeting in honor of Francis Birch, in press.

Hanks, T.C., 1970. The Kurile trench-Hokkaida rise system: large shallow earthquakes and simple models of deformation, Trans. Am. Geophys. Un., 51, 823 (Abstract).

Isacks, B. & Molnar, P., 1969. Mantle earthquake mechanisms and the sinking of the lithosphere, Nature, 223, 1121-1124.

Isacks, B. & Molnar, P., 1971. Distribution of stresses in the descending lithosphere from a global survey of focal-mechanism solutions of mantle earthquakes, Rev. Geophys. Space Phys., 9, 103-174.

Jacob, K.H., 1970. Three-dimensional seismic ray tracing in a laterally heterogeneous spherical earth, J. geophys. Res., 75, 6675-6689.

Kanamori, H., 1968. Travel times to Japanese stations from Longshot and their geophysical implications, Bull. Earthq. Res. Inst., 46, 841-859.

Kanamori, H., 1970. Mantle beneath the Japanese arc, Phys. Earth Planet Int., 3, 475.

Kanamori, H., 1971. Seismological evidence for a lithospheric normal faulting--the Sanriku earthquake of 1933, Phys. Earth Planet Int., 4, 289-300.

Le Pichon, X., 1968. Sea-floor spreading and continental drift, J. geophys. Res., 73, 3661-3697.

Le Pichon, X., 1970. Correction to paper by Xavier Le Pichon, Sea-floor spreading and continental drift, J. geophys. Res., 75, 2793.

Luyendyk, B.P., 1970. Dips of downgoing lithospheric plates beneath island arcs, Bull. geol. Soc. Am., 81, 3411-3416.

MacDonald, G.J.F., 1959. Calculations on the thermal history of the earth, J. geophys. Res., 64, 1967-2000.

McConnell, R.K., Jr., 1968. Viscosity of the Earth's mantle, in Proc. Conf. History Earth's Crust, 1966, ed. by R.A. Phinney, Princeton University Press.

McKenzie, D.P., 1969. Speculation on the consequences and causes of plate motion, Geophys. J. R. astr. Soc., 18, 1-32.

Minear, J.W. & Toksöz, M.N., 1970. Thermal regime of a downgoing slab and new global tectonics, J. geophys. Res., 75, 1397-1419.

Mitchell, A.R., 1969. Computation methods in partial differential equations, Wiley, London.

Mitronovas, W. & Isacks, B., 1971. Seismic velocity anomalies in the upper mantle beneath the Tonga-Kermadec Island Arc, J. geophys. Res., 76, 7154-7180.

Molnar, P. & Sykes, L.R., 1969. Tectonics of the Caribbean and Middle American regions for focal mechanisms and seismicity, Bull. geol. Soc. Am., 80, 1639-1684.

Nowinski, J. & Turski, S., 1953. On the theory of elasticity of nonhomogeneous isotropic bodies (in Polish with Russian and English summaries), Arch. Mech. Stos. 1, 5, 67-88.

Ringwood, A.E. & Major, A., 1970. The system Mg_2SiO_4-Fe_2SiO_4 at high pressures and temperatures, Phys. Earth Planet Int., 3, 89-108.

Schatz, F.J., 1971. Thermal conductivity of earth materials at high temperatures, Ph.D. Thesis, MIT, Cambridge, Mass.

Schubert, G. & Turcotte, D.L., 1971. Phase changes and mantle convection, J. geophys. Res., 76, 1424-1432.

Stauder, W., 1968a. Mechanisms of the Rat-Island earthquake sequence of February 4, 1965, with relation to island arcs and sea-floor spreading, J. geophys. Res., 73, 3847-3858.

Stauder, W., 1968b. Tensional character of earthquake foci beneath the Aleutian trench with relation to sea-floor spreading, J. geophys. Res., 73, 7693-7701.

Sykes, L.R., 1966. The seismicity and deep structure of island arcs, J. geophys. Res., 71, 2981-3006.

Tillman, C.C., 1971. On-line solution of elliptic boundary-value problems, Ph.D. Thesis, MIT, Cambridge, Mass.

Toksöz, M.N., Minear, J.W. & Julian, B.R., 1971. Temperature field and geophysical effects of a down-going slab, J. geophys. Res., 76, 1113-1138.

Utsu, T., 1967. Anomalies in seismic wave velocities and attenuation associated with a deep earthquake zone (I), J. of Fac. of Sci., Hok. Univ., Japan, Ser. VII, 3, 1-25.

Varga, R.S., 1962. Matrix iterative analysis, Prentice-Hall, N.J.

Walcott, R.I., 1970. Flexural rigidity, thickness and viscosity of the lithosphere, J. geophys. Res., 75, 3941-3954.

Weertman, J., 1970. The creep strength of the earth's mantle, Rev. Geophys. Space Phys., 8, 145-168.

Wyss, M., 1970. Stress estimates for South American shallow and deep earthquakes, J. geophys. Res., 75, 1529-1544.

Table I-A. Models of Descending Lithosphere using Elastostatic Simulation

Model	Figure Number	Thermal Regime (Figure)	Depth of Slab (km)	Plate* Boundary	Poisson Ratio	Log Ratio of Young's Modulus		
						Slab(center) / Slab(edge)	Mantle(440 km) / Mantle(140 km)	Slab† / Mantle
1	3	1	560	free	0.25	0.0	0.0	0.0
2	4a	1	560	rigid	0.25	0.0	0.4	0.5
3	4b	1	560	free	0.25	0.0	3.0	0.3
4	5a	2	420	rigid	0.30	0.8	2.5	0.8
5	5b	2	420	rigid	0.30	0.5	0.0	3.0
6	6a	2	420	rigid	0.30	0.4	2.3	0.6
7	6b	1	380	free	0.25	0.0	0.7	1.0
8	7	1	560	rigid	0.25	1.7	3.0	0.5
9	9	1	560	rigid	0.25	0.0	0.4	0.5
10	10	-	560	rigid	0.25	0.0	-	-
11	10	-	560	rigid	0.25	0.0	0.4	0.5

* Boundary condition on edge of lithosphere

† Measured 100 km from end of slab

Table I-B. Stress Distribution in Descending Lithosphere Models

Model	Down-dip Principle Stress in Slab*			
	Intermediate (160 km depth)			Deep (>250 km)
	Top Face	Center	Bottom face	
1	P low	I low	I med	P low
2	P high	I low	T high	P,I med
3	T high	I med	P high	P high
4	P med	P high	I med	P high
5	I low	T high	T med	T med
6	P high	I med	T high	P med
7	P,I med	I low	T high	P high
8	I low	T,I high	I low	P high
9	T low	T low	T low	T,P med
10	P low	I low	T low	P,I low
11	I low	I low	I low	I low

* Down-dip stress: P, compression; T, tension; I, intermediate.

Maximum shear stress: low, <150 bar; med, 150-300 bar; high, >300 bar.

Table II. Numerical Integration of Equilibrium Equation for Descending Slab: 45° dip; 8 cm/yr; 80 km thick

Depth (km)	Body** Force (dyne/cm^3)	Mantle Resistance (bar)	slab depth:	Down-dip Stress* 700	560	280
35.	-100.	30.		896	2209	672
71.	-100.	30.		434	1747	210
106.	-100.	30.		-29	1285	-252
141.	-100.	30.		-491	823	-714
177.	-100.	144.		-953	361	-1176
212.	-100	296.		-1273	41	-1496
247	-100.	606.		-1405	-91	-1628
283.	-180.	606.		-1148	166	-1371
318.	-260.	606.		-1291	23	
353.	-260.	606.		-1833	-520	
389.	-260.	606.		-2376	-1063	
424.	-100.	606.		-2919	-1606	
459.	-100.	606.		-2662	-1349	
495.	-100.	606.		-2405	-1092	
530.	-180.	606.		-2148	-834	
565.	-260.	606.		-2291	-977	
601.	-260.	608.		-2834		
636.	-260.	715.		-3374		
671.	-100.	822.		-3780		
707.	-100.	929.		-3252		
End-resistance (bar):				-2591	-1520	-1514

* Positive denotes tension (bar)

** Component along the slab

Figures

Fig. 1.

Temperature field at time t = 12.96 by using MacDonald's (1959) value of the radiative conductivity. Adiabatic compression, phase changes, shear-heating, and radioactive-heating are included as energy sources in the model. The spreading rate is 8 cm/yr. Shading indicates zones of phase changes. For the elastostatic problem, the slab is truncated when its temperature reaches equilibrium with the surrounding mantle at 560 km. (reproduced from Toksöz et al. 1971).

Fig. 2.

Temperature field at time t = 9.45 my for a 30 degree dipping slab with Schatz's (1971) radiative conductivity. All other parameters are the same. The MacDonald geotherm has been used for the mantle. Notice the larger thermal gradients and temperature contrasts within the slab (provided by N. Sleep 1971).

Fig. 3.

Maximum shear stress for model 1: contours of maximum shear stress in bars are shown in the slab for stresses less than 500 bars. The arrows indicate the direction of deviatoric compression or tension (principle stresses minus hydrostatic pressure) for select nodes of the finite-difference

solution. In this case, Young's modulus, E, is constant throughout the region for both the mantle and slab, and it equals 1.5 10^{12} dynes/cm^2. The gravitational body forces result from thermal contraction using the temperature regime in Fig. 1.

Figs. 4a and b.

Solutions for the maximum shear stress for two different mantle conditions using the temperature regime of Fig. 1. The contours on the right are again those of maximum shear stress in bars within the slab. Shear stresses greater than 500 bars are not contoured in these illustrations. The stresses within the mantle are not contoured. On the left, E represents Young's modulus (dynes/cm^2) used for the mantle surrounding the slab. Unless otherwise specified, the elastic moduli of the slab are constant within it and equal to the lithosphere's value.

Fig. 4a

Model 2 depicts sagging of the slab at 160 km in the asthenosphere: compression near the top face, tension at the lower surface. Only a slight decrease in the asthenosphere's strength is used for the model.

Fig. 4b

In contrast, model 3 with low strength asthenosphere and increasing strength with depth.

Figs. 5a and b.

Solution of maximum shear stress for two different mantle supports using a 30 degree dipping slab in Fig. 2. Section A-A' depicts the temperature dependence of Young's modulus within the slab for both models.

Fig. 5a.

Model 4 with a soft asthenosphere and increasing mantle support. Compression results along the full length of the slab.

Fig. 5b.

Model 5 with little mantle support. The slab hangs under tension.

Fig. 6a.

Maximum shear stress for model 6 using the thermal regime in Fig. 2 and a slowly varying thermal dependence in the slab given by section A-A'. Sagging effects and stress concentrations again result along the edge of the slab.

Fig. 6b.

Maximum shear stress for model 7 when the thermal regime of Fig. 1 is truncated at 380 km. An extended asthenosphere is used for a slab with constant elastic moduli. Both sagging and intermediate tensional stresses occur within the slab.

Fig. 7.

Maximum shear stress for model 8 illustrating a slab with strongly varying elastic moduli given by section A-A'. The thermal regime in Fig. 1 is used for the computations. Large down-dip tensional stresses predominate at intermediate depths and gradually rotate to compression for greater depths.

Fig. 8.

Three-dimensional diagram summarizing the dependence of the models upon the elastic moduli. The three coordinates represent increasing mantle strength with depth relative to the asthenosphere (mantle/mantle), increasing temperature dependence of the slab's elastic moduli (slab/slab), and increasing contrast between the slab and mantle's elastic moduli (slab/mantle). The points refer to models 1 through 8 in Table 1. The regions blocked off are meant only as a rough guide to the characteristic stress patterns observed for the previous models.

Fig. 9.

The maximum shear stress for model 9 with olivine-spinel phase change introduced at 400 km depth according to Ringwood & Major's (1970) data and using the thermal regime in Fig. 1. A density anomaly of approximately

0.3 gm/cm^3 results at 350 km. The elastic moduli in the mantle and slab are the same as model 2.

Fig. 10.

Maximum shear stress for two models simulating convection. Model 10 on the right is for a free plate with 50 bars traction along its upper face simulating mantle resistance. The arrows again indicate direction of principle stress at various nodes. The maximum shear stress is less than 100 bars throughout the slab. Model 11 on the left uses a shear-couple at the mantle-slab interface to simulate resistance by the mantle. The arrows indicate the component of the shear couple acting on the slab, while a similar component but in the opposite direction acts upon the mantle. The mantle's elastic modulus for this model is given on the left and is the same as model 2. The maximum shear stress is approximately 70 bars throughout the slab.

Fig. 11.

Global summary of the distribution of down-dip stresses in inclined seismic zones. The stress axis that is approximately parallel to the dip of the zone is represented by an unfilled (open) circle for compression or P axis, and a filled (solid) circle for the tensional or T axis;

an "X" indicates that neither the P nor the T axis is approximately parallel to the dip. For each region the line represents the seismic zone in a vertical section aligned perpendicular to the strike of the zone. The lines show approximately the dips and lengths of the zone and gaps in the seismic activity as a function of depth (reproduced from Isacks & Molnar 1971).

Figs. 12a and b.

Down-dip stresses in the inclined seismic zones as a function of convergence rate and depth. The filled circles indicate the maximum depth of down-dip tension; the open circles show the shallowest down-dip compressional solution (Isacks & Molnar 1971). If two of the same circles occur for a region, they represent the lower and upper bound for the deepest tensional solution or the shallowest compressional event inferred from the boundaries of the aseismic gap in Fig. 11. The Kurile island arc apparently has tensional and compressional solutions scattered throughout the region. The convergence rates are taken from Le Pichon (1968, 1970). The lines across the diagram depict theoretical limits when the down-dip stress is greater than 1 kilobar. The solid line defines the lower bound for tension; the dashed line is the upper bound for compression; and stresses generally less than 500 bars occur

between the limits. The maximum depth of the slab is given on the right for each theoretical model.

Fig. 12a.

Limits of tension and compression for inclined seismic zones dipping less than 45 degrees. Theoretical models for a 45 degree dipping slab are included for slabs penetrating 560 and 700 km in depth.

Fig. 12b.

Inclined seismic zones and theoretical models for steeply dipping slabs (60 degrees or more). New Zealand has been included in the previous diagram since the curves merge for slowly converging slabs.

Fig. 13a.

Annual number of earthquakes per 25 km depth intervals as a function of depth for three select regions: Tonga, Kurile-Kamchatka, and Alaska (data from Sykes 1966).

Fig. 13b.

Magnitude of down-dip principle stress as a function of depth for slab models using numerical integration of the equilibrium equation. The gravitational body forces and mantle resistance are a function of convergence rate. The models correspond to the previous three regions: a 700 km depth slab at 9 cm/yr convergence rate for Tonga;

560 km depth at 8 cm/yr for the Kurile island arc; and 300 km depth at 6 cm/yr for Alaska-Aleutian slab. The dips are shown along side the depth. Effects of lithospheric bending and overthrusting are not included for shallow depths. The relative shapes of the curves show a distinct correlation.

Fig. 14.

Finite-difference solution for a plane-strain elastostatic problem with variable elastic moduli in the y-direction. The boundary conditions for the square region are illustrated at the bottom. The arrows indicate the 25 dyne/cm^3 body force imposed at the boundary nodes on the far right. The 20 cm sides consist of 11 grid points. The solution along the y-axis is shown at the top together with the value of Young's modulus. The theoretical solution is 25 dynes/cm^2 except near the rigid boundary.

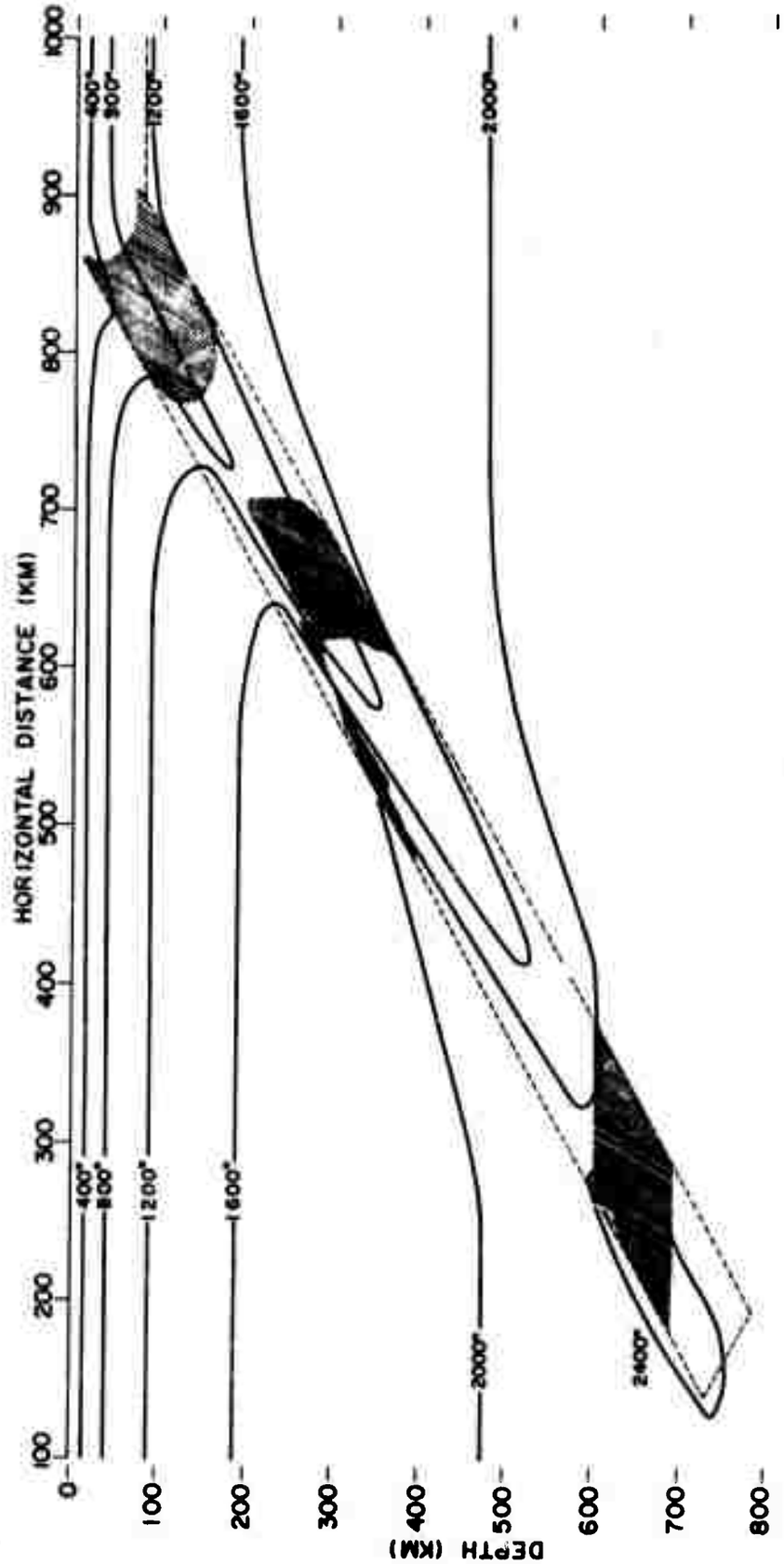
HORIZONTAL DISTANCE (KM)
0
100
200
300
400
500
600
700
800
900
1000
400'
800'
1200'
1600'
2000'
2400'
DEPTH (KM)
0
100
200
300
400
500
600
700
800

Fig. 1

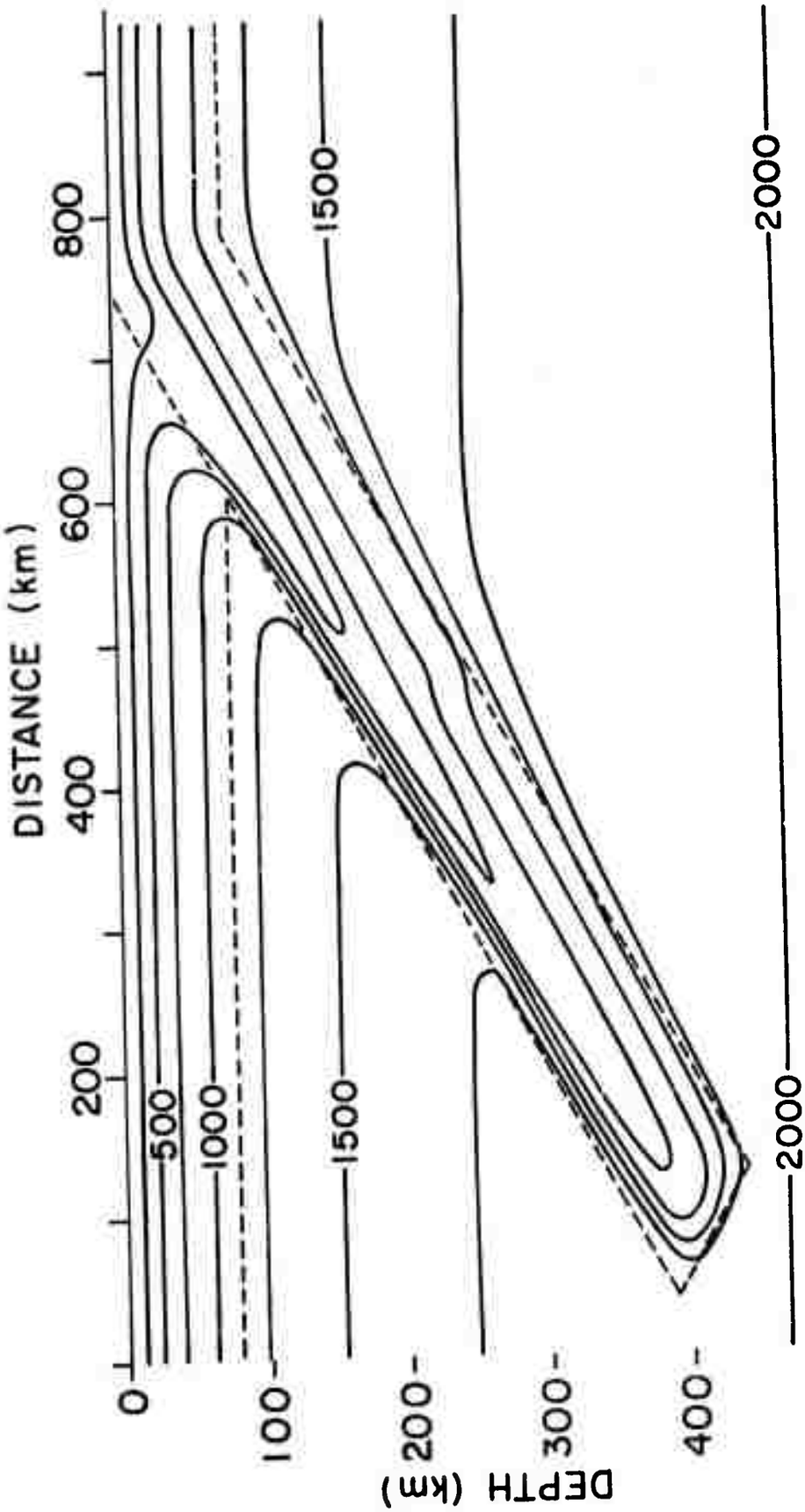
DISTANCE (km)
0
200
400
600
800
500
1000
1500
2000
1500
2000
0
100
200
300
400
500
DEPTH (km)

Fig. 2

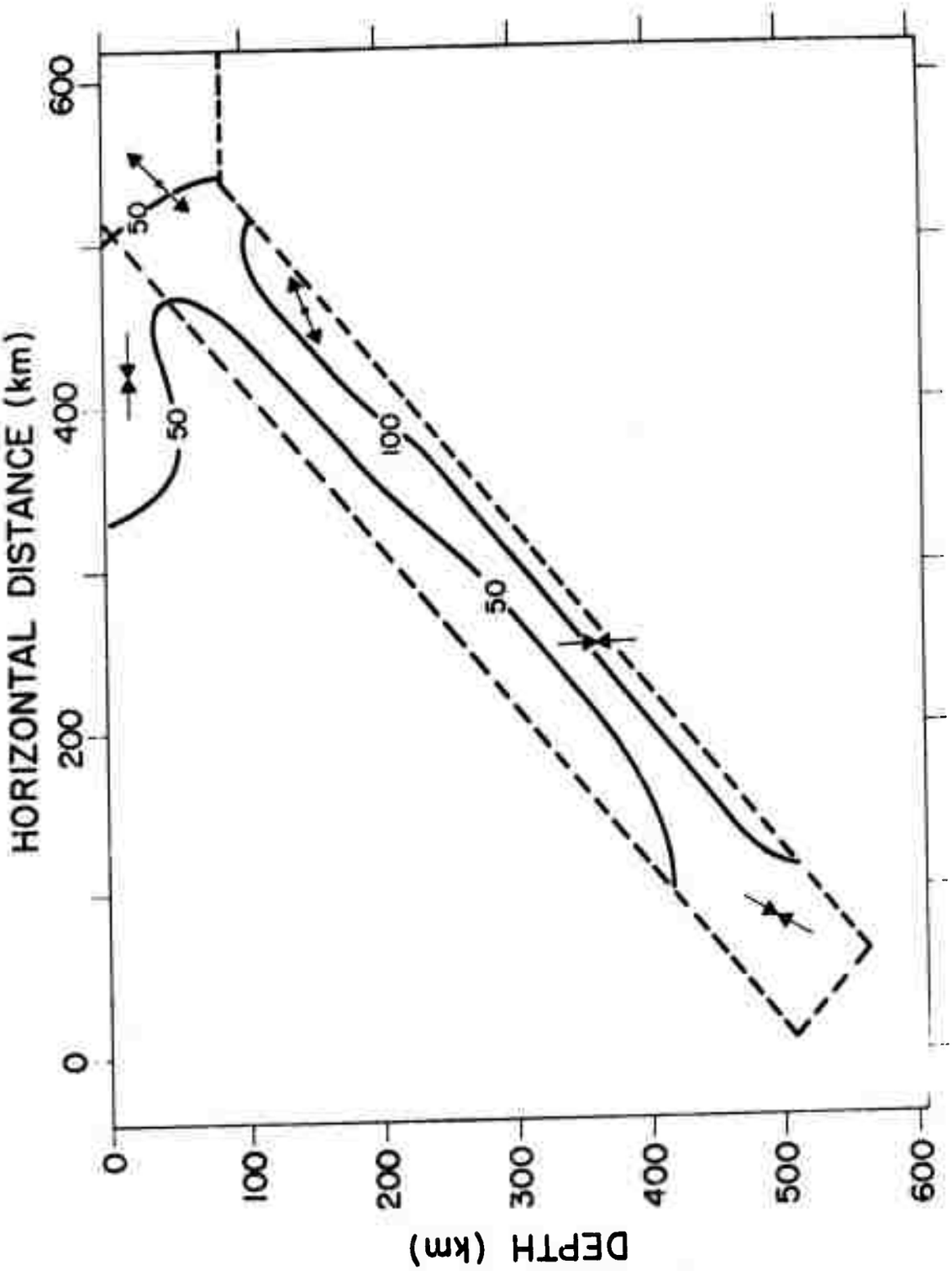
HORIZONTAL DISTANCE (km)
0
200
400
600
50
50
100
50
DEPTH (km)
0
100
200
300
400
500
600

Fig. 3

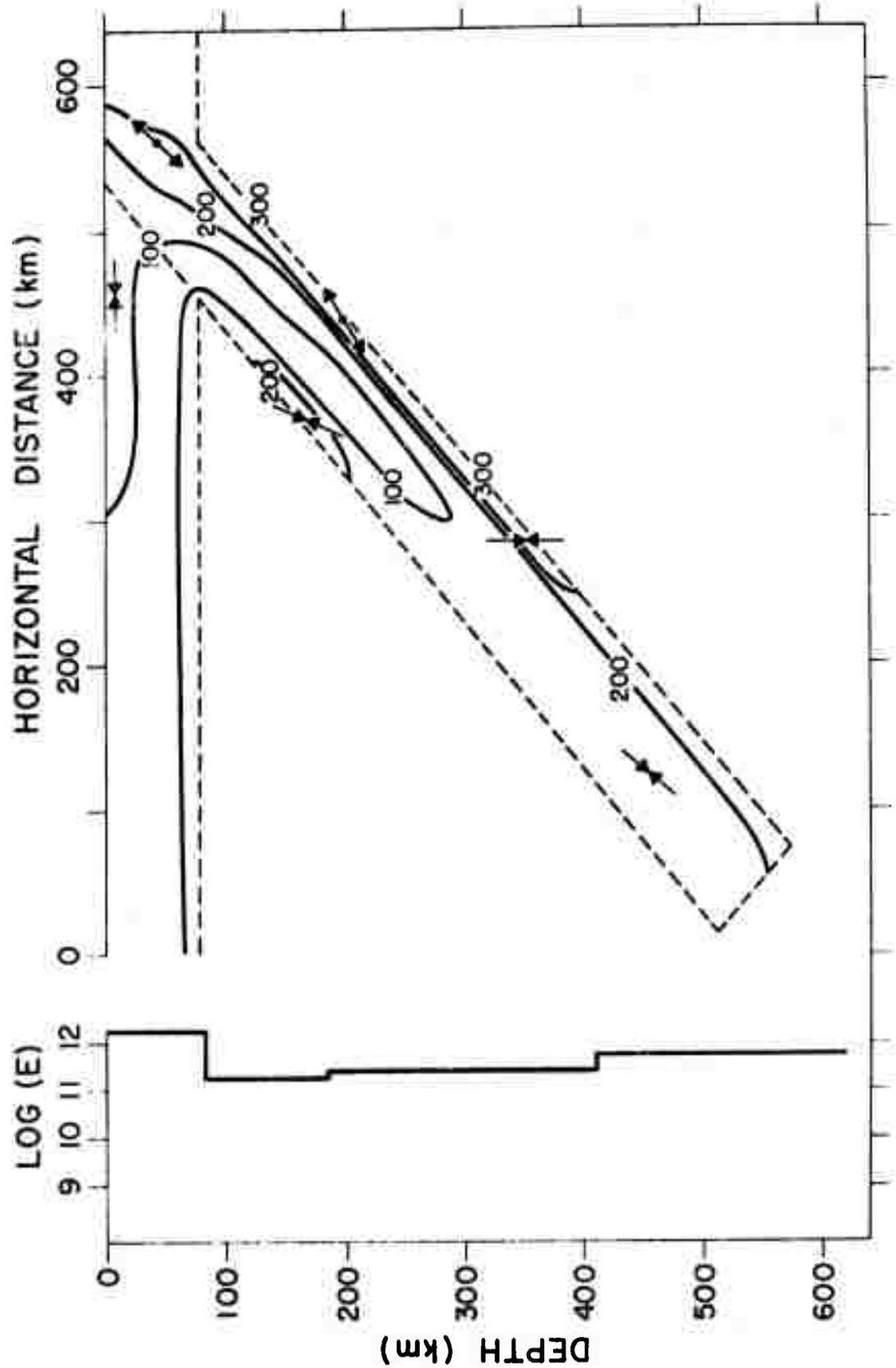
HORIZONTAL DISTANCE (km)
0
200
400
600
100
200
300
100
200
300
200
LOG (E)
9
10
11
12
DEPTH (km)
0
100
200
300
400
500
600

Fig. 4a

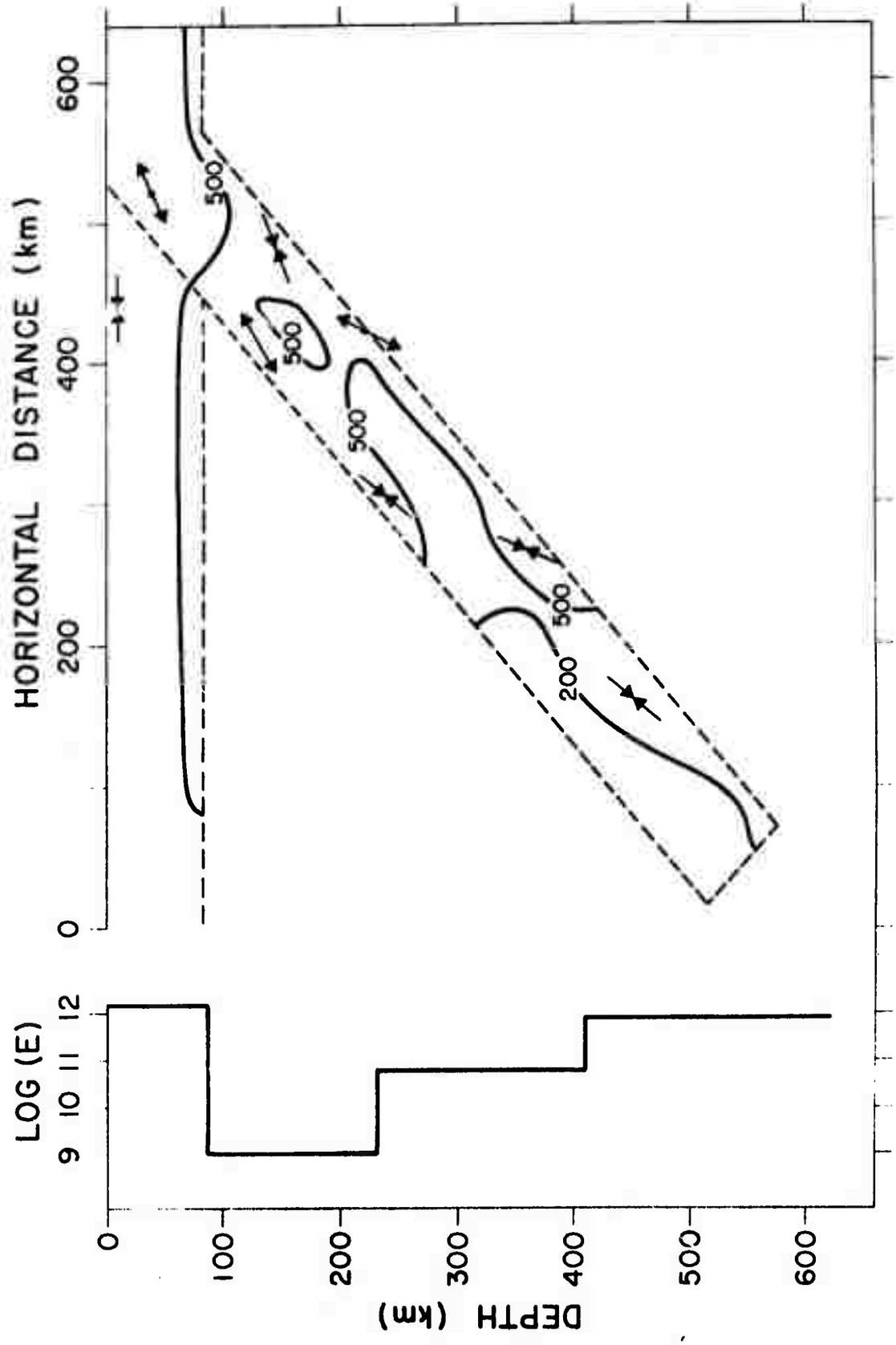
HORIZONTAL DISTANCE (km)
0
200
400
600
500
500
500
500
200
LOG (E)
9 10 11 12
0
100
200
300
400
500
600
DEPTH (km)

Fig. 4b

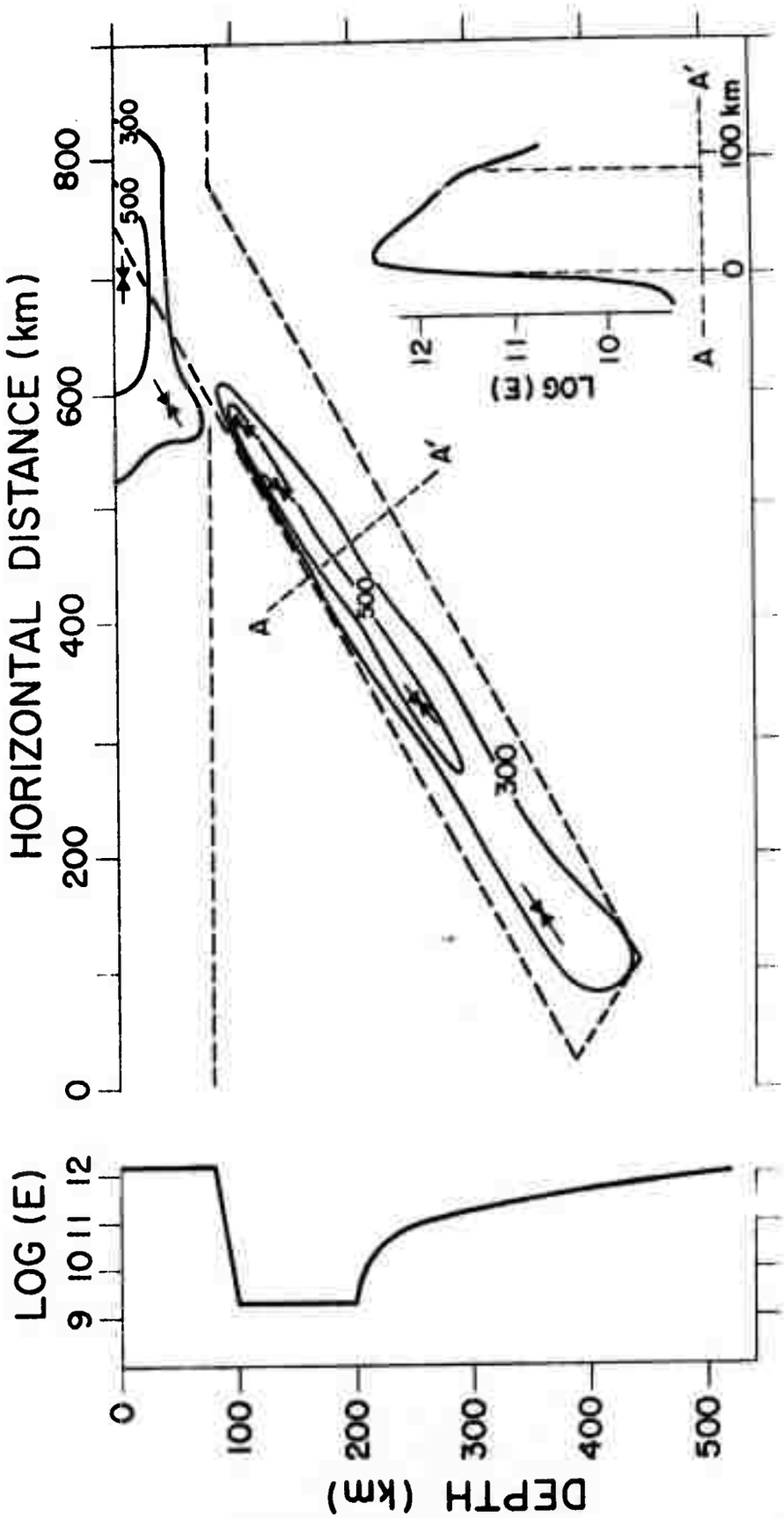
HORIZONTAL DISTANCE (km)
0
200
400
600
800
300
500
A
A'
LOG (E)
9 10 11 12
DEPTH (km)
0
100
200
300
400
500
LOG (E)
12
11
10
A
A'
100 km
0

Fig. 5a

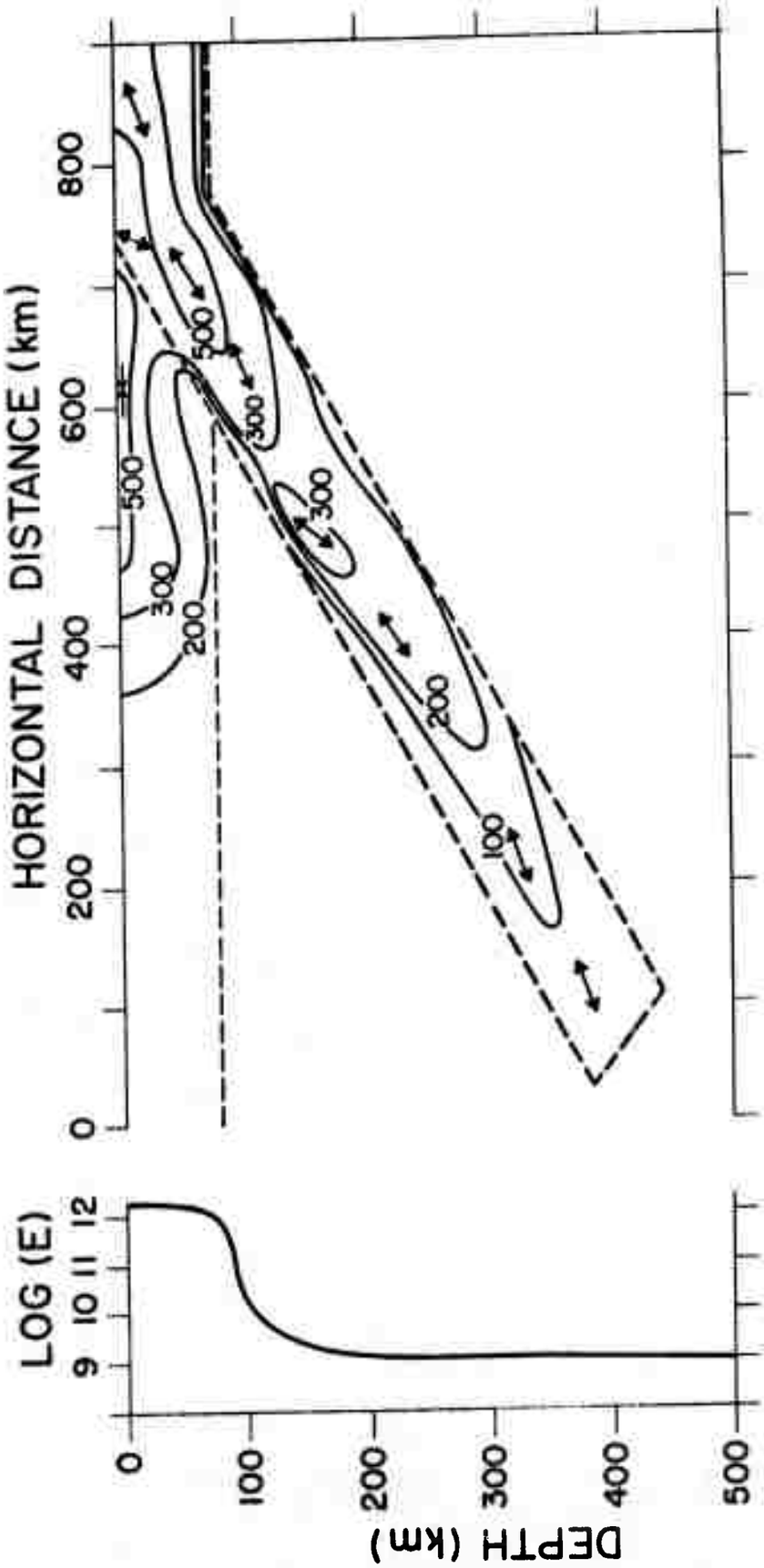
HORIZONTAL DISTANCE (km)
0
200
400
600
800
500
300
200
100
LOG (E)
9
10
11
12
0
100
200
300
400
500
DEPTH (km)

Fig. 5b

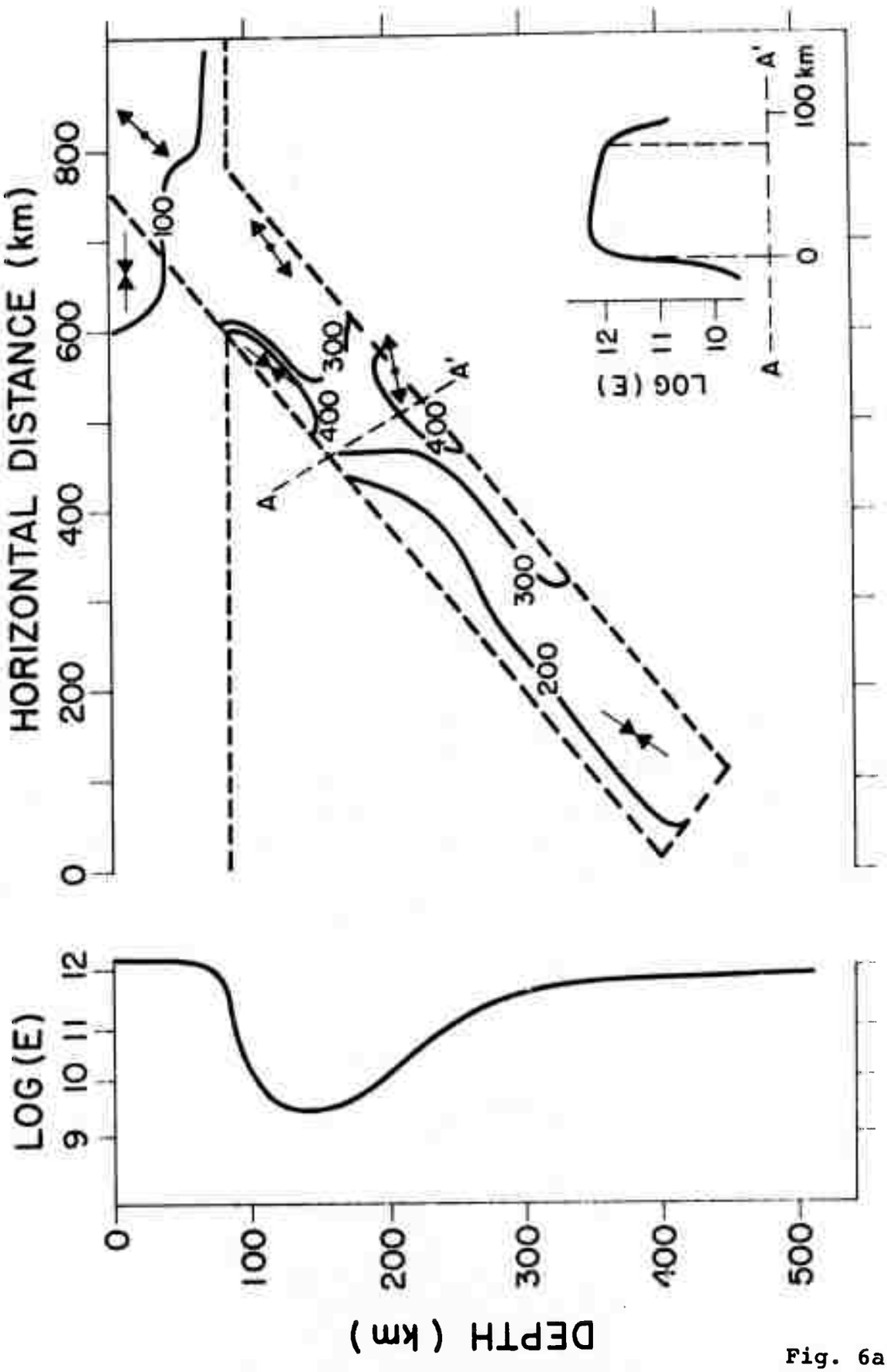
HORIZONTAL DISTANCE (km)
0
200
400
600
800
100
300
400
400
300
200
A
A'
LOG (E)
12
11
10
A
A'
0
100 km
LOG(E)
9
10
11
12
0
100
200
300
400
500
DEPTH (km)

Fig. 6a

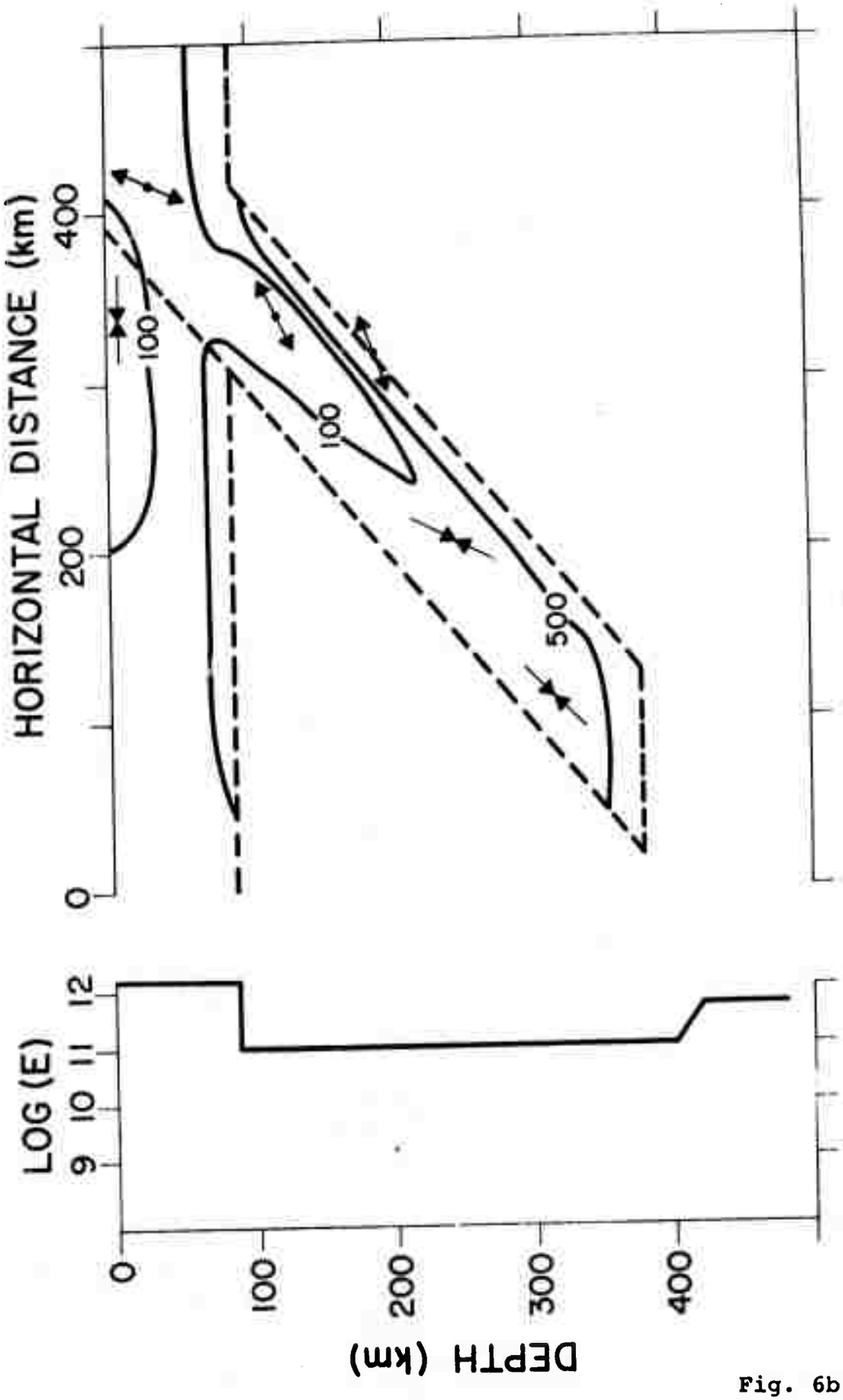
HORIZONTAL DISTANCE (km)
0
200
400
100
100
500
LOG (E)
9
10
11
12
0
100
200
300
400
DEPTH (km)

Fig. 6b

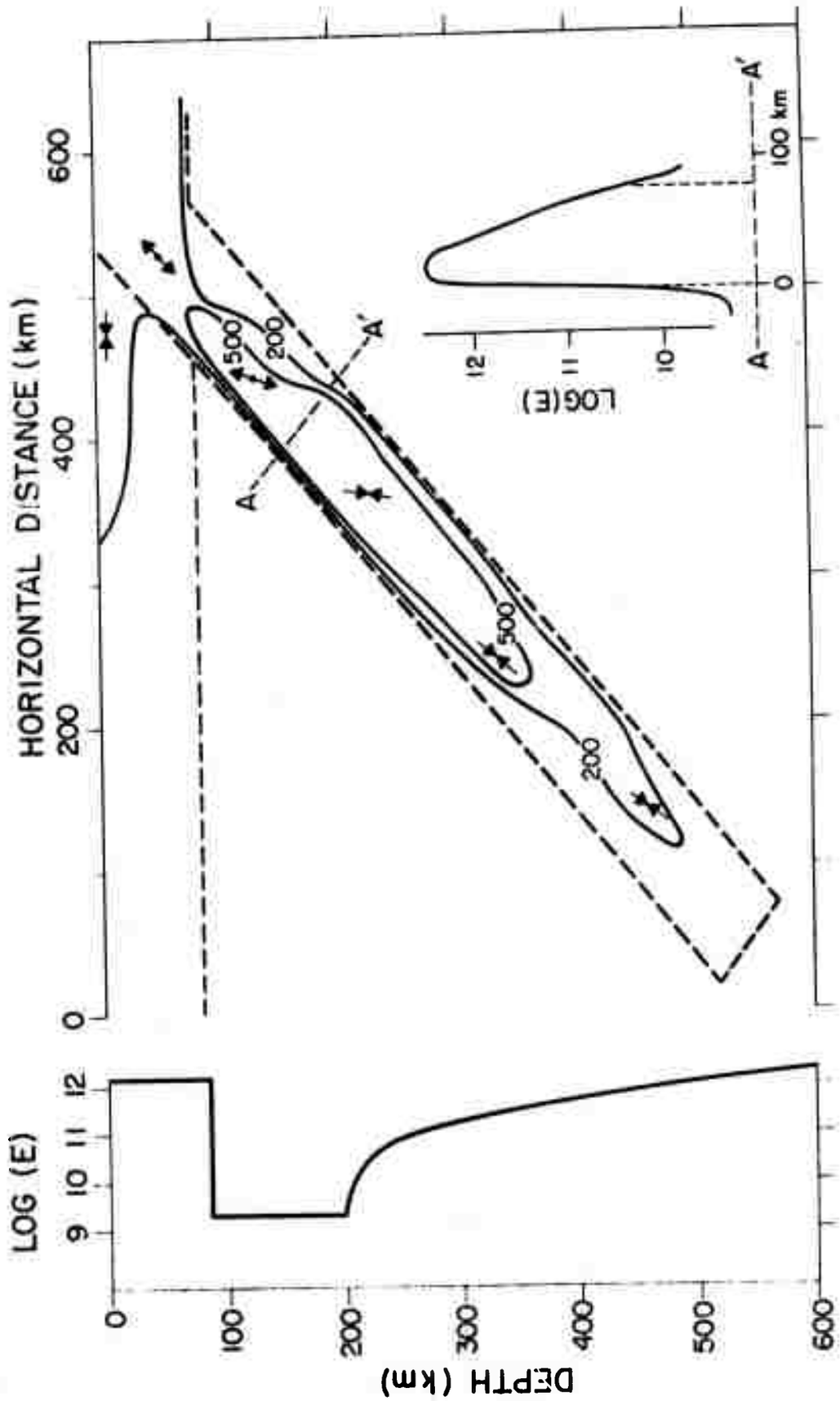
HORIZONTAL DISTANCE (km)
0
200
400
600
500
200
A
A'
LOG(E)
12
11
10
A
A'
100 km
0
500
200
LOG (E)
9
10
11
12
0
100
200
300
400
500
600
DEPTH (km)

Fig. 7

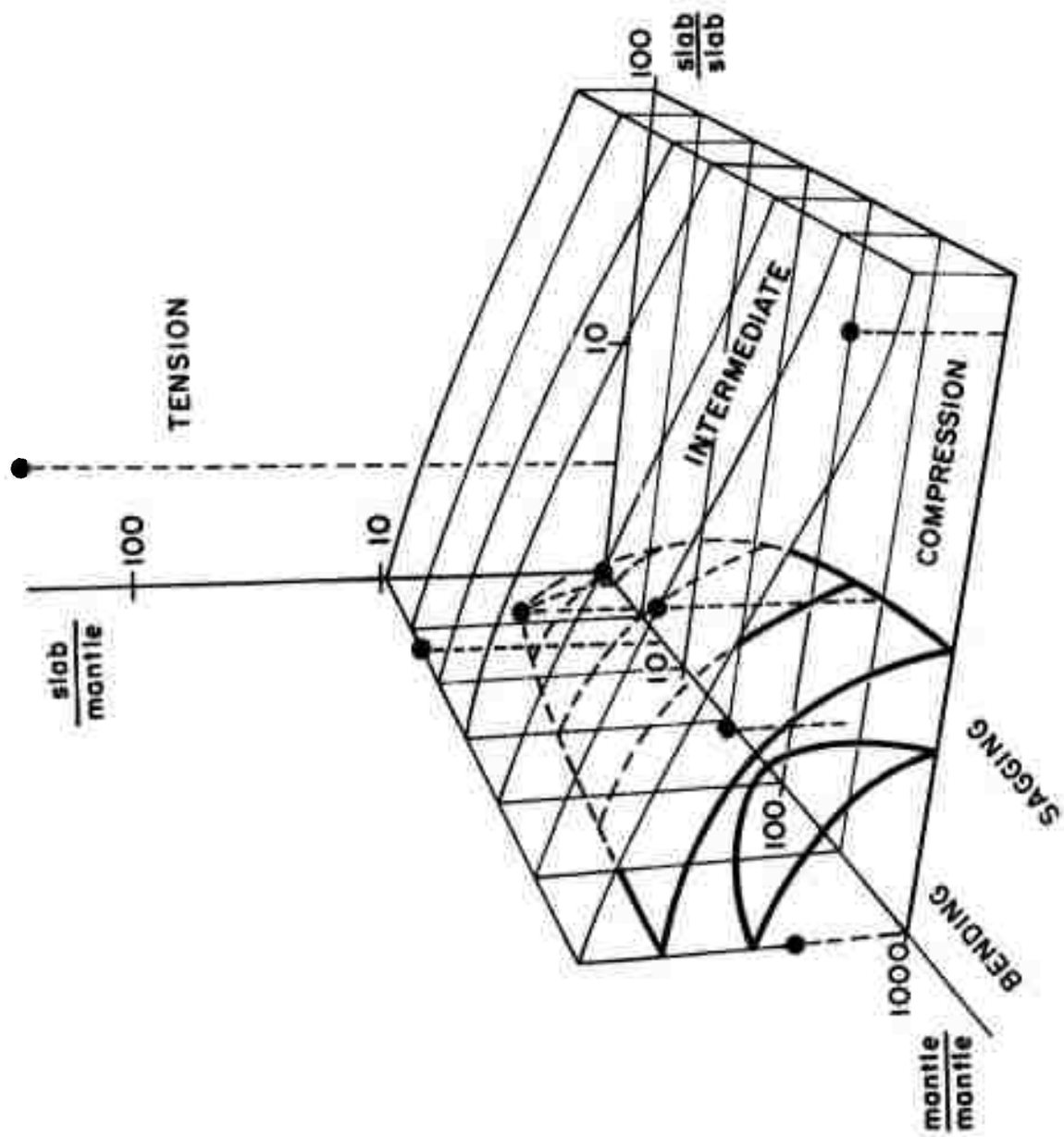
TENSION
100
slab/mantle
10
100
slab/slab
10
INTERMEDIATE
COMPRESSION
10
100
SAGGING
BENDING
1000
mantle/mantle

Fig. 8

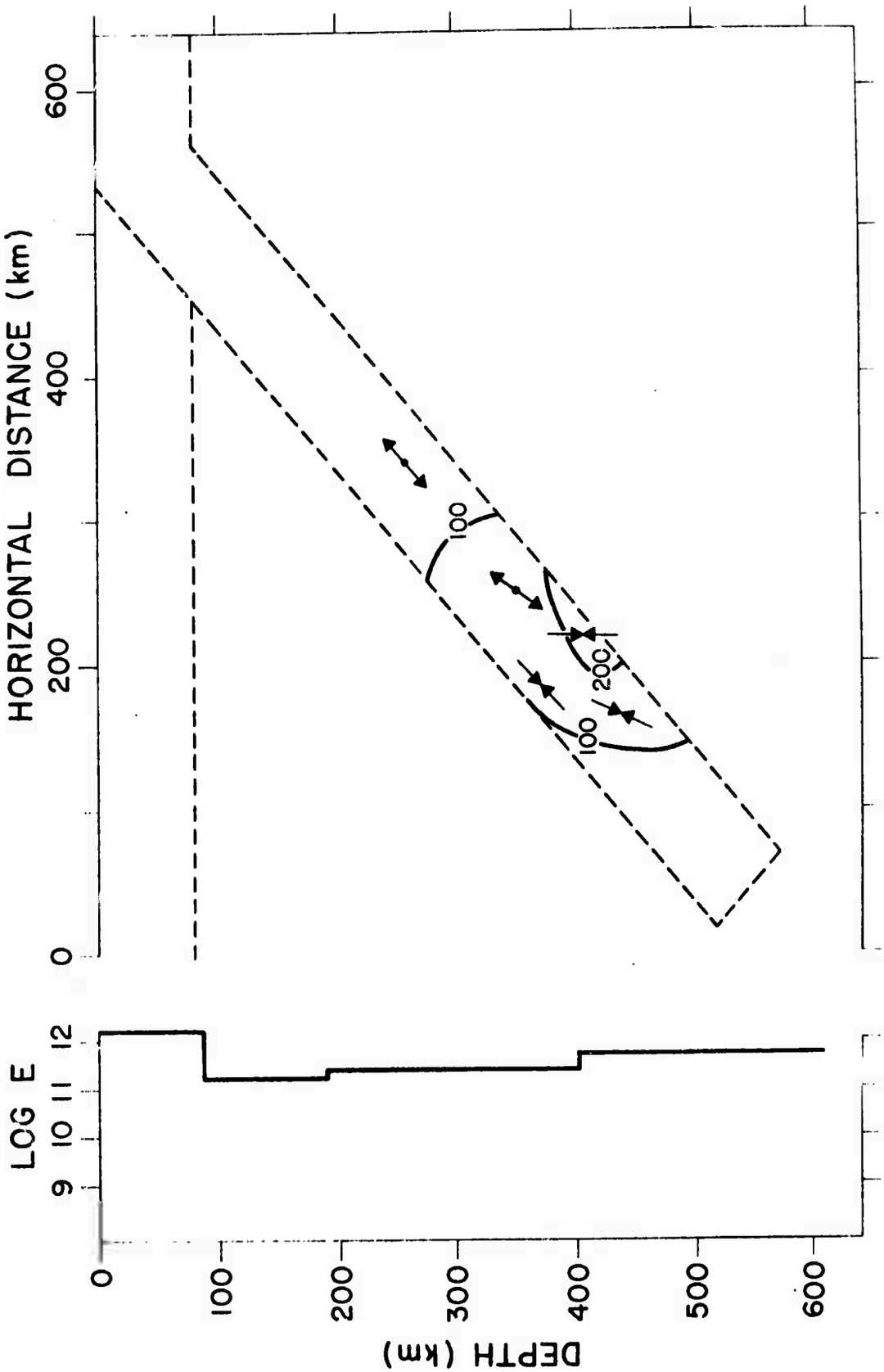
HORIZONTAL DISTANCE (km)
0
200
400
600
100
200
100
LOG E
9
10
11
12
0
100
200
300
400
500
600
DEPTH (km)

Fig. 9

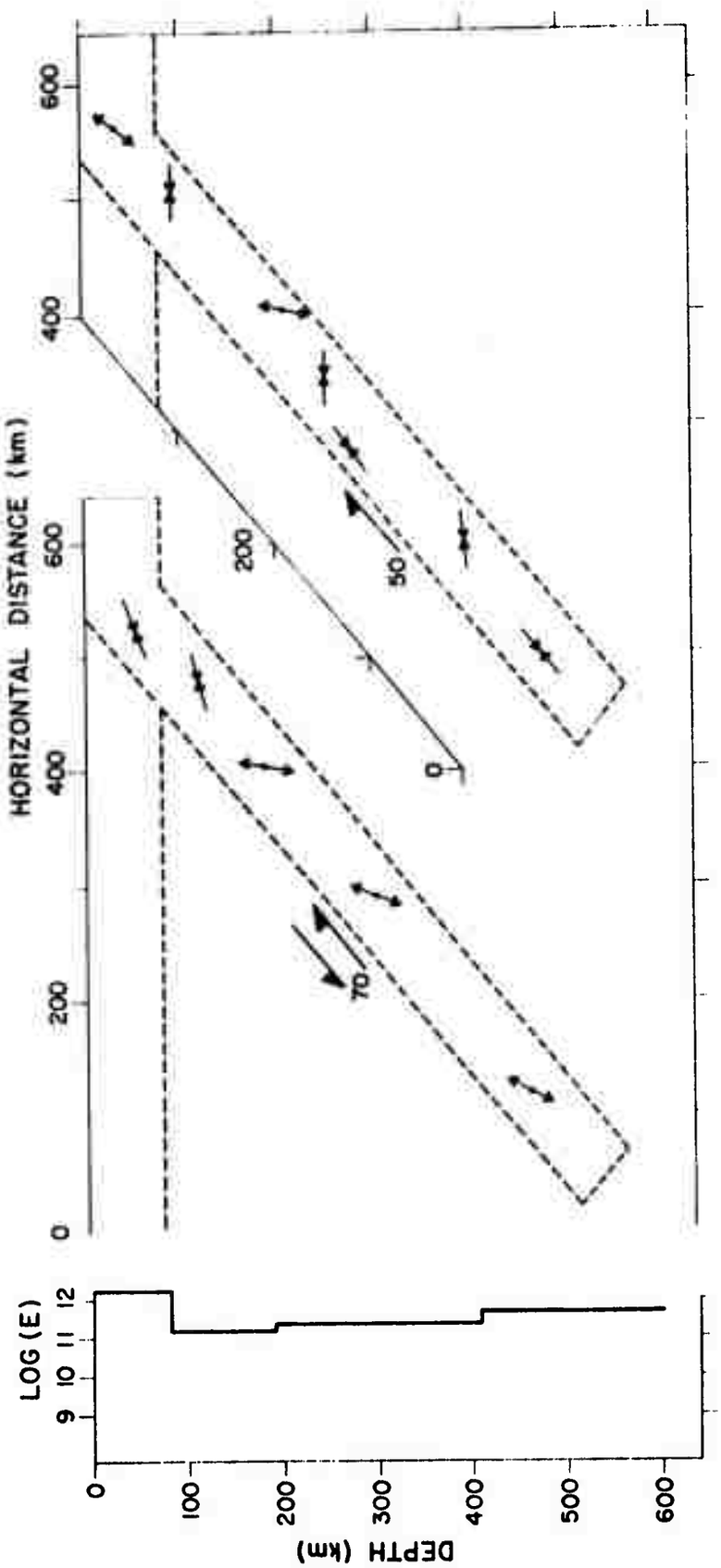
HORIZONTAL DISTANCE (km)
0
200
400
600
0
50
200
70
LOG (E)
9
10
11
12
0
100
200
300
400
500
600
DEPTH (km)

Fig. 10

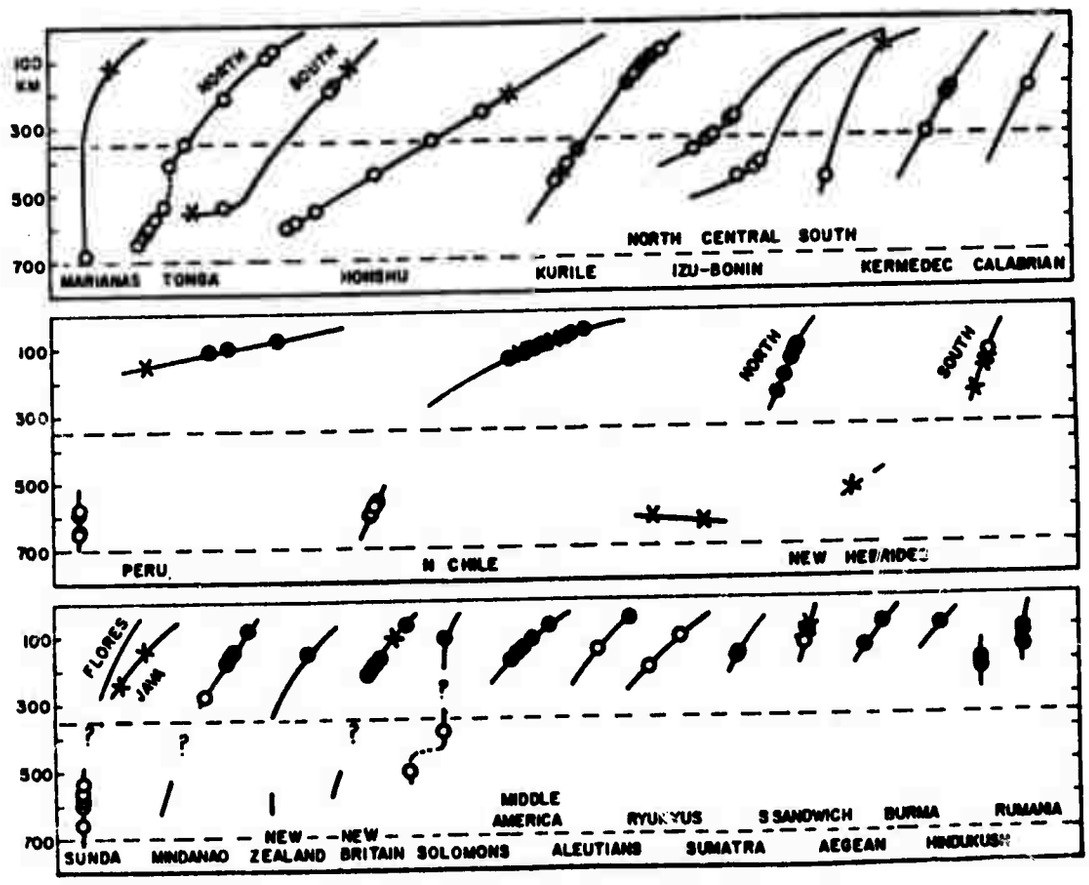
100 KM
300
500
700
NORTH
SOUTH
NORTH CENTRAL SOUTH
MARIANAS TONGA
HONSHU
KURILE
IZU-BONIN
KERMEDEC CALABRIAN
100
300
500
700
NORTH
SOUTH
PERU
N CHILE
NEW HEBRIDES
100
300
500
700
FLORES
JAVA
?
?
?
?
MIDDLE AMERICA
RYUKYUS
S SANDWICH
BURMA
RUMANIA
SUNDA
MINDANAO
NEW ZEALAND
NEW BRITAIN
SOLOMONS
ALEUTIANS
SUMATRA
AEGEAN
HINDUKUSH

Fig. 11

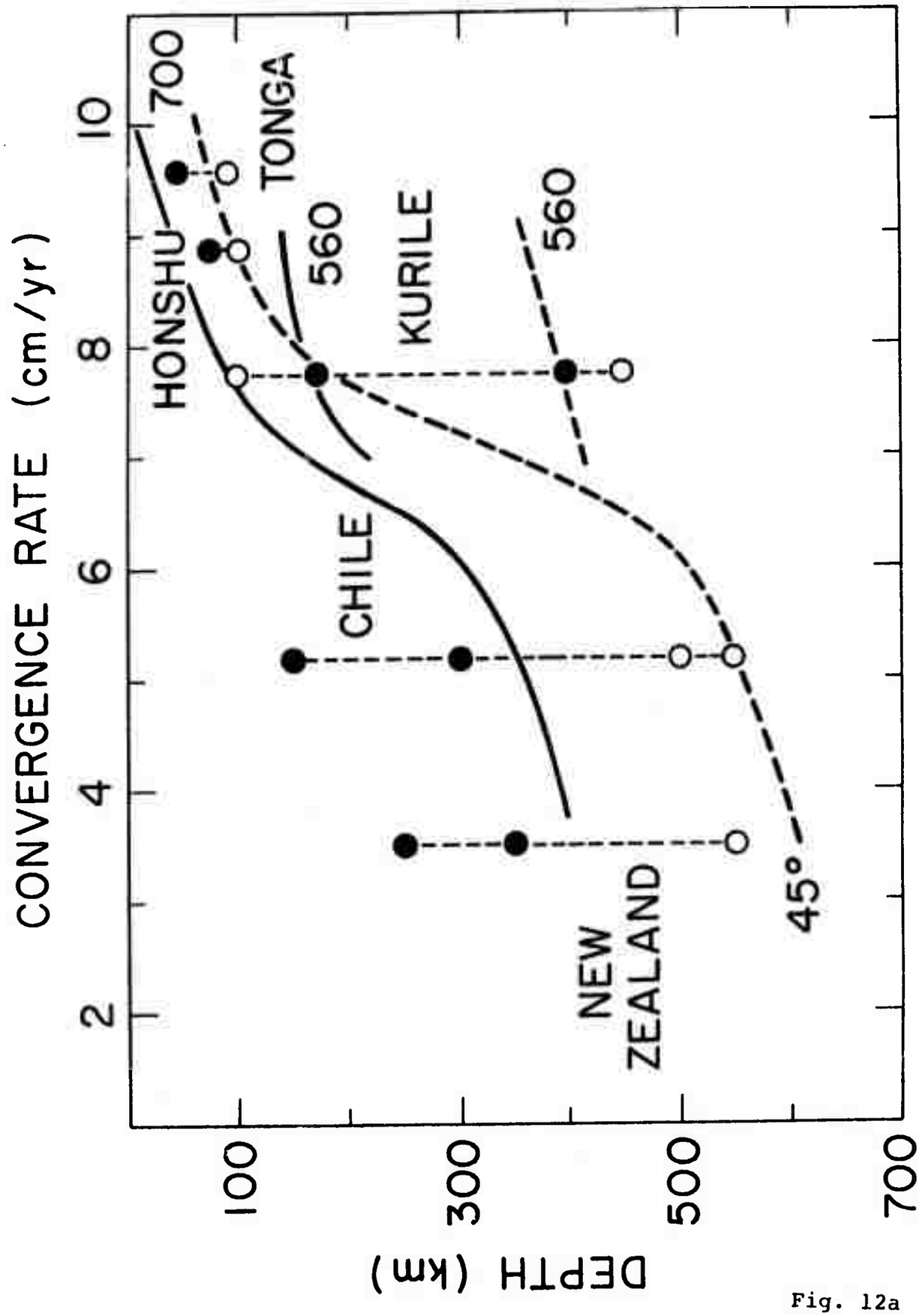
CONVERGENCE RATE (cm/yr)
2
4
6
8
10
DEPTH (km)
100
300
500
700
HONSHU
700
TONGA
560
KURILE
560
CHILE
NEW ZEALAND
45°

Fig. 12a

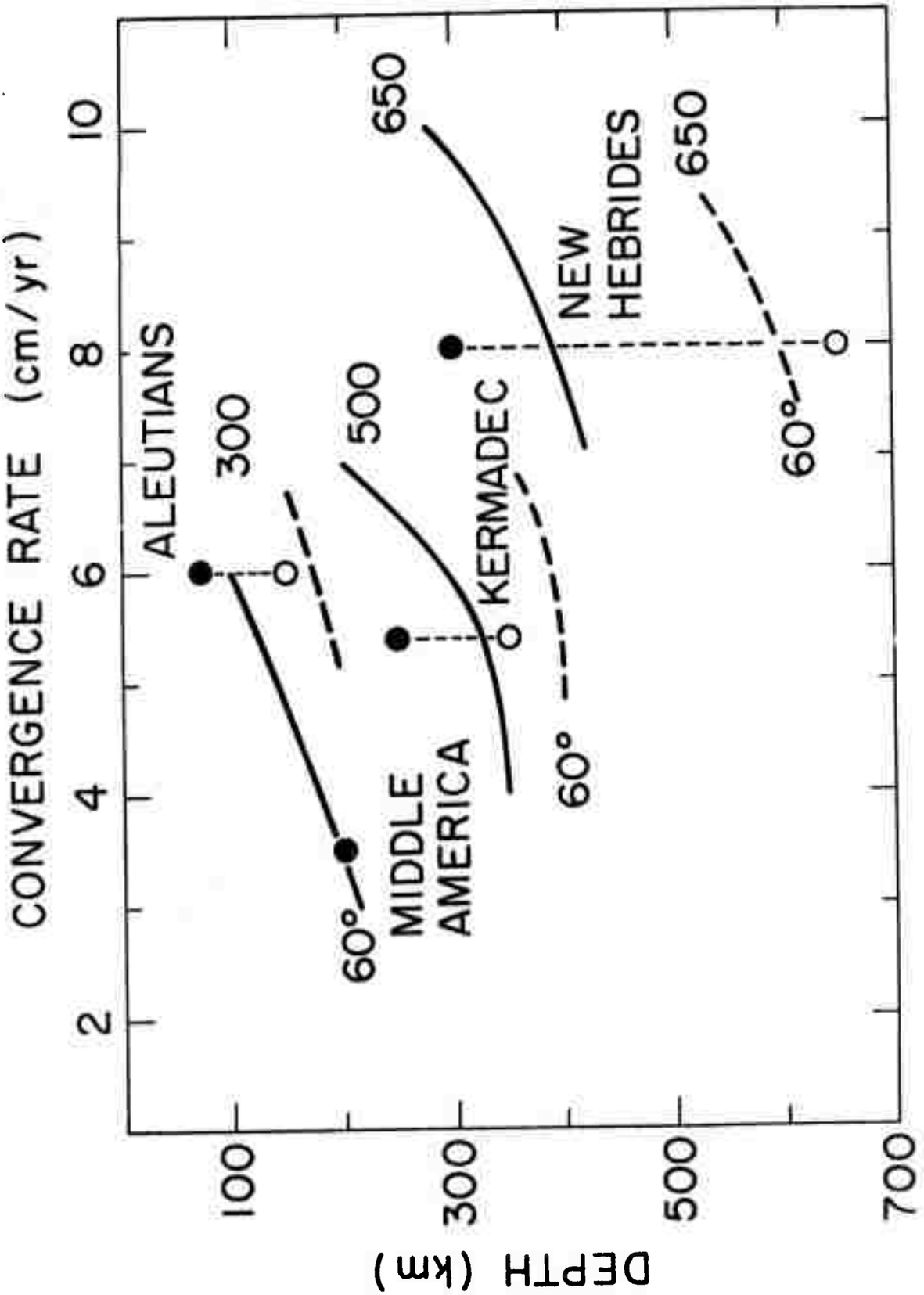
CONVERGENCE RATE (cm/yr)
2
4
6
8
10
DEPTH (km)
100
300
500
700
ALEUTIANS
MIDDLE AMERICA
KERMADEC
NEW HEBRIDES
300
500
650
650
60°
60°
60°

Fig. 12b

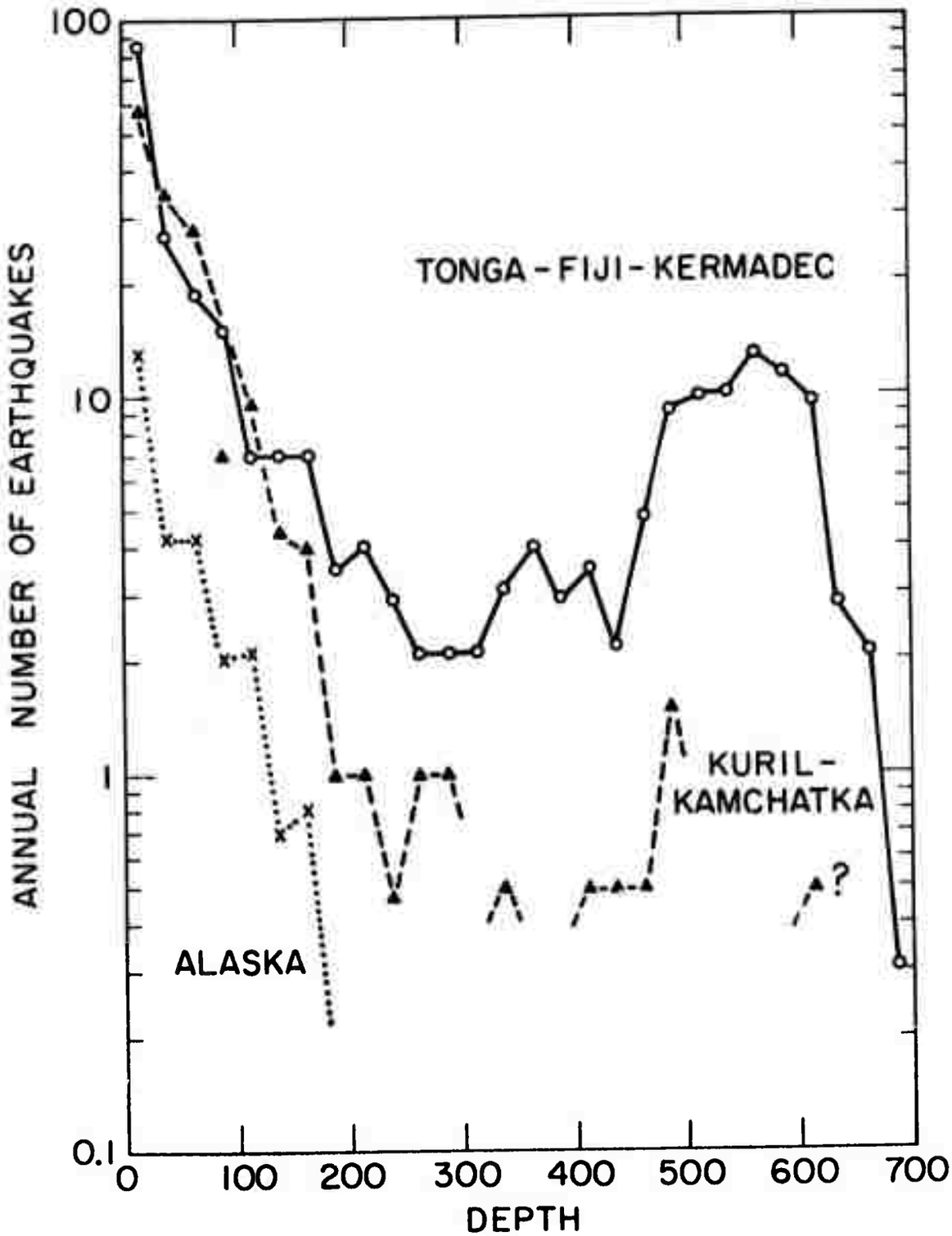
100
10
1
0.1
ANNUAL NUMBER OF EARTHQUAKES
TONGA - FIJI - KERMADEC
KURIL - KAMCHATKA
?
ALASKA
0
100
200
300
400
500
600
700
DEPTH

Fig. 13a

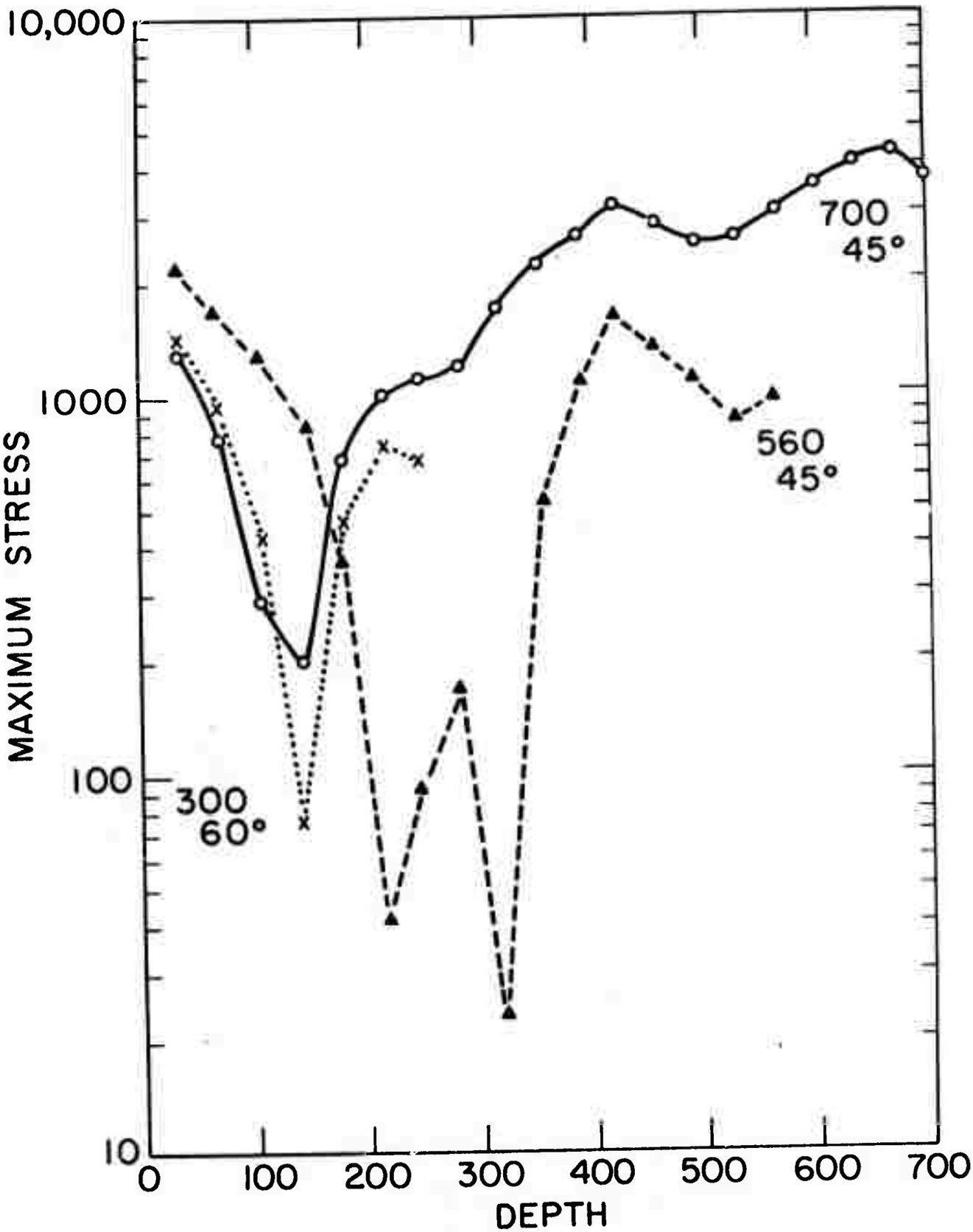
10,000
1000
100
10
MAXIMUM STRESS
0
100
200
300
400
500
600
700
DEPTH
700
45°
560
45°
300
60°

Fig. 13b

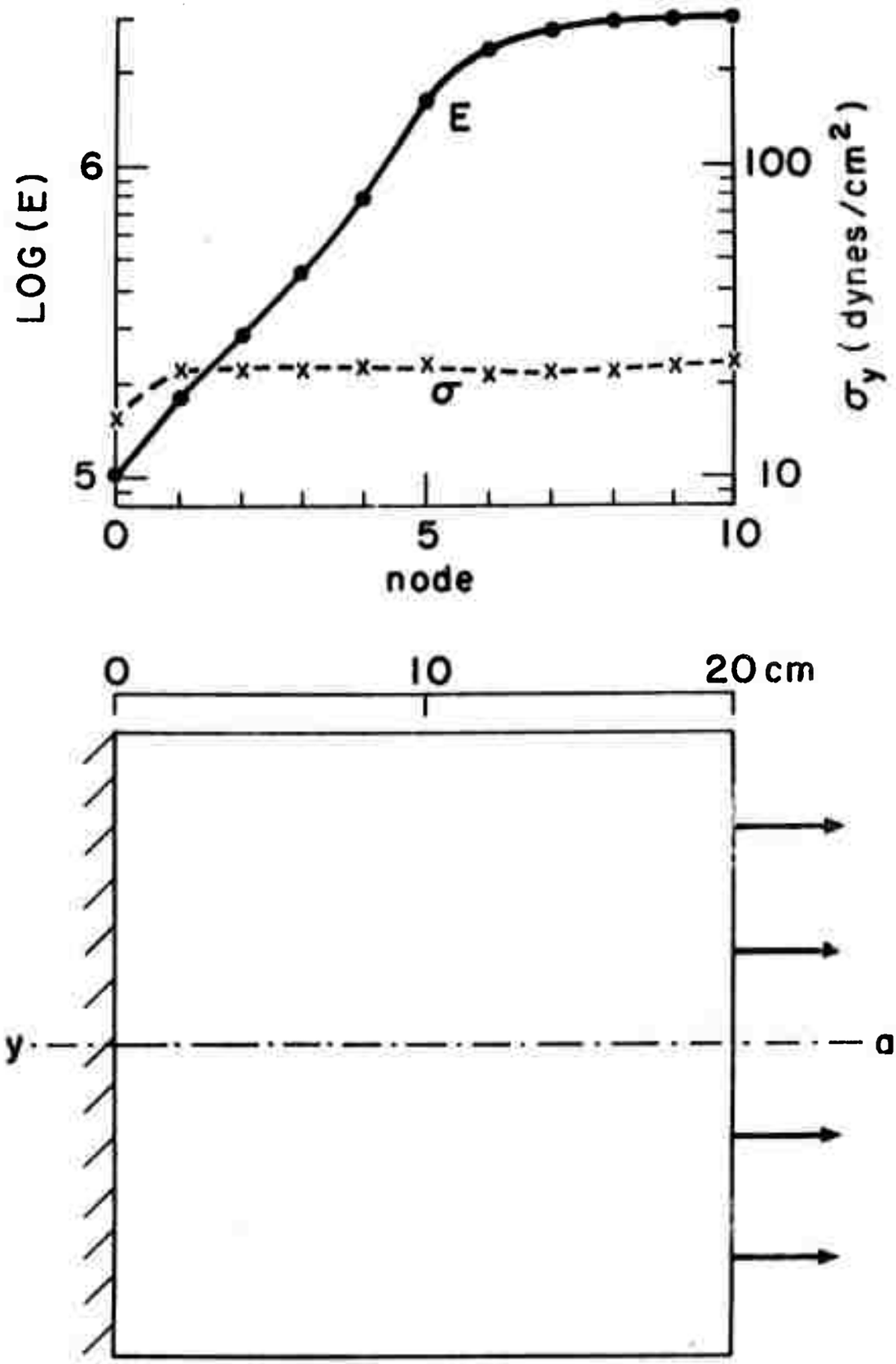
LOG (E)
6
5
E
100
10
σ_y (dynes/cm^2)
σ
0
5
10
node
0
10
20 cm
y
axis

Fig. 14

5. LIST OF PUBLICATIONS DURING CONTRACT YEAR

Aki, K., Earthquake mechanism, Tectonophysics, 13, 423-446, 1972a.

Aki, K., Recent results on the mechanism of earthquakes with implications on the prediction and control program, Tectonophysics, in press, 1972b.

Aki, K., Scaling law of earthquake source-time function, Geophys. J. Roy. Astron. Soc., in press, 1972c.

Ida, Y., Cohesive force across the tip of a longitudinal-shear crack and Griffith's specific surface energy, J. Geophys. Res., 77, 3796-3805, 1972.

Madariaga, R.I., Toroidal free oscillations of the laterally heterogeneous earth, Geophys. J. Roy. Astron. Soc., 27, 81-100, 1972.

Madariaga, R.I. and K. Aki, Spectral splitting of toroidal-free oscillations due to lateral heterogeneity of the earth's structure, J. Geophys. Res., 77, 4421-4431, 1972.

Shlien, S., Earthquake-tide correlation, Geophys. J. Roy. Astron. Soc., 28, 27-34, 1972.

Smith, A.T., Jr., and M.N. Toksöz, Stress distribution beneath island arcs, Geophys. J. Roy. Astron. Soc., in press, 1972.

Solomon, S.C., Seismic-wave attenuation and partial melting in the upper mantle of North America, J. Geophys. Res., 77, 1483-1502, 1972a.

Solomon, S.C., On Q and seismic discrimination, Geophys. J. Roy. Astron. Soc., in press, 1972b.

Toksöz, M.N. and H.H. Kehrer, Tectonic strain release by underground nuclear explosions and its effect on seismic discrimination, Geophys. J. Roy. Astron. Soc., in press, 1972.

6. LIST OF THESES COMPLETED DURING CONTRACT YEAR

Madariaga, Raul I., Free Oscillations of the Laterally Heterogeneous Earth, Ph.D. Thesis, Massachusetts Institute of Technology, Cambridge, 105 pp., 1971.

Smith, Albert T., Jr., The Stress Distribution Beneath Island Arcs, M.S. Thesis, Massachusetts Institute of Technology, Cambridge, 104 pp., 1971.

Ward, Ronald W., Synthesis of Teleseismic P-Waves from Sources Near Transition Zones, Ph.D. Thesis, Massachusetts Institute of Technology, Cambridge, 206 pp., 1971.